공학박사 학위논문

Bounded Relative Motion and Station-Keeping in the Vicinity of Libration Point Orbits Leveraging Hamiltonian Structure and Disturbance Observer Technique

해밀턴 구조와 외란 관측기 기법을 이용한 라그랑주 점 궤도 주변에서의
경계 상대 운동 및 궤도유지

2020 년 8 월

서울대학교 대학원

기계항공공학부

정 승 윤

Bounded Relative Motion and Station-Keeping in the Vicinity of Libration Point Orbits Leveraging Hamiltonian Structure and Disturbance Observer Technique

해밀턴 구조와 외란 관측기 기법을 이용한 라그랑주 점 궤도 주변에서의 경계 상대 운동 및 궤도유지

지도교수 김 유 단

이 논문을 공학박사 학위논문으로 제출함

2020 년 6 월

서울대학교 대학원

기계항공공학부

정 승 윤

정승윤의 공학박사 학위논문을 인준함

2020 년 6 월

위 원 장 기 창 돈 (인)

부위원장 김 유 단 (인)

위 원 김 현 진 (인)

위 원 박 찬 국 (인)

위 원 박 찬 덕 (인)

Bounded Relative Motion and Station-Keeping in the Vicinity of Libration Point Orbits Leveraging Hamiltonian Structure and Disturbance Observer Technique

by

Seungyun Jung

Submitted to the Graduate School of
Seoul National University
in partial fulfillment of the requirements for the degree of

Doctor of Philosophy

Department of Mechanical and Aerospace Engineering
Seoul National University

Advisor: Prof. Youdan Kim

August 2020

Bounded Relative Motion and Station-Keeping in the Vicinity of Libration Point Orbits Leveraging Hamiltonian Structure and Disturbance Observer Technique

by

Seungyun Jung

Approved as to style and content by:

Changdon Kee, Chair, Ph.D.

Youdan Kim, Vice-Chair, Ph.D.

H. Jin Kim, Member, Ph.D.

Chan Gook Park, Member, Ph.D.

Chandeok Park, Member, Ph.D.

Abstract

Bounded Relative Motion and Station-Keeping in the Vicinity of Libration Point Orbits

Leveraging Hamiltonian Structure and Disturbance Observer Technique

Seungyun Jung
Department of Mechanical and Aerospace Engineering
The Graduate School
Seoul National University

In this dissertation, a novel strategy for station-keeping and formation flight of spacecraft in the vicinity of unstable libration point orbits is presented, and its performance and stability are analyzed. The presented control strategy leverages the Hamiltonian nature of the equations of motion, rather than simply applying the control theory from the perspective of "signal processing". A filtered extended high-gain observer, a kind of disturbance observer, is designed to mitigate the performance degradation of the control strategy due to model uncertainties and external disturbances.

Canonical coordinates are adopted to design a controller that exploits the mathematical structure of Hamiltonian system inherent in orbital mechanics, and then the equations of motion of spacecraft are represented in the form of Hamilton's equation with generalized coordinates and momenta. The base-

line controller, utilizing the canonical form of the Hamiltonian system, is divided into two parts: i) a Hamiltonian structure-preserving control, and ii) an energy dissipation control. Hamiltonian structure-preserving control can be designed in accordance with the Lagrange-Dirichlet criterion, i.e., a sufficient condition for the nonlinear stability of Hamiltonian system. Because the Hamiltonian structure-preserving control makes the system marginally stable instead of asymptotically stable, the resultant motion of the Hamiltonian structure-preserving control yields a bounded trajectory. Through the frequency analysis of bounded relative motion, a circular motion can be achieved for particular initial conditions. By appropriately switching the gain of the Hamiltonian structure-preserving control, the radius of bounded motion can be adjusted systematically, which is envisioned that this approach can be applied to spacecraft formation flight. Furthermore, the energy dissipation control can be activated to make the spacecraft's bounded relative motion converge to the nominal orbit.

On the other hand, a filtered extended high-gain observer is designed for the robust station-keeping and formation flight even under highly uncertain deep-space environment. The filtered extended high-gain observer estimates the velocity state of the spacecraft and disturbance acting on the spacecraft by measuring only the position of the spacecraft. The filtered extended high-gain observer includes an integral state feedback to attenuate navigation error amplification due to the high gain of the observer. The global convergence of the observer is shown, and it is also shown that the tracking error is ultimately bounded to the nominal libration point orbit by applying the Hamiltonian structure-based controller.

Numerical simulations demonstrate the performance of the designed control

strategy. Halo orbit around the L_2 point of the Earth-Moon system is considered as an illustrative example, and various perturbations are taken into account.

Keywords: Libration Point Orbit, Unstable Orbit, Non-Keplerian Orbit, Station-Keeping, Spacecraft Formation Flight, Hamiltonian System, Extended High-Gain Observer

Student Number: 2015-20790

Contents

Abstract **i**

Contents **v**

List of Tables **ix**

List of Figures **xi**

1 Introduction **1**

1.1 Background and Motivation 1

1.2 Literature Review 3

1.2.1 Spacecraft Station-Keeping in the Vicinity of the Libration Point Orbits 3

1.2.2 Spacecraft Formation Flight in the Vicinity of the Libration Point Orbits 5

1.3 Contributions 7

1.4 Dissertation Outline 10

2 Background **13**

2.1 Circular Restricted Three-Body Problem 14

2.1.1 Equilibrium Solutions and Periodic Orbits 16

2.1.2 Stability of Periodic Orbits 20

2.2 Hamiltonian Mechanics 21
2.2.1 Hamiltonian Approach to CR3BP 21
2.2.2 Hamiltonian Approach to LPO Tracking Problem 22

3 Hamiltonian Structure-Based Control **25**
3.1 Classical Linear Hamiltonian Structure-Preserving Control 27
3.2 Switching Hamiltonian Structure-Preserving Control 29
3.2.1 Orbital Properties of Spacecraft 33
3.2.2 Switching Point 1: From a Circular Orbit to an Elliptical Orbit 34
3.2.3 Switching Point 2: From an Elliptical Orbit to a Circular Orbit 37
3.3 Hamiltonian Structure-Based Control 39
3.3.1 Potential Shaping Control 39
3.3.2 Energy Dissipation Control 45

4 Filtered Extended High-Gain Observer and Closed-Loop Stability **49**
4.1 Filtered Extended High-Gain Observer and Its Convergence . . . 51
4.2 Closed-Loop Stability Analysis 56

5 Numerical Simulations **67**
5.1 Disturbance Model 67
5.2 Navigation Error Model 68
5.3 Simulation Results 69
5.3.1 Simulation 1 71
5.3.2 Simulation 2 77

5.3.3 Simulation 3 81
5.3.4 Simulation 4 93
5.3.5 Simulation 5 98

6 Conclusion **101**

6.1 Concluding Remarks 101
6.2 Further Work 103

Bibliography **105**

국문초록 **127**

List of Tables

Table 5.1 Nominal halo orbit parameter values 70

Table 5.2 System parameter values 71

Table 5.3 Radius of transfer orbit 72

Table 5.4 Initial values of spacecrafts 72

Table 5.5 Average estimation error 90

Table 5.6 Mean and standard deviation of tracking error 90

Table 5.7 Mean and standard deviation of tracking error depending on potential shaping control gain 96

List of Figures

Figure 2.1 Geometry of the CR3BP. 15

Figure 2.2 Sample member from the $L_1 and L_2$ families of planar lyapunov orbits in the Earth-Moon system 17

Figure 2.3 Sample member from the L_1 families of halo orbits in the Earth-Moon system 18

Figure 2.4 Sample member from the L_2 families of halo orbits in the Earth-Moon system 19

Figure 3.1 Switching point No.1 38

Figure 3.2 Switching point No.2 38

Figure 4.1 Set of maximum eigenvalue of $\Lambda_{\dot{\mathbf{W}}}$ during one-period of LPO (black dot line is a reference orbit) 62

Figure 5.1 Nominal halo orbit 70

Figure 5.2 Orbit transfer using switching HSP control (relative motion) 73

Figure 5.3 Relative position of spacecraft No.1 (from $R_1 = 50m$ to $R_2 = 100m$) 74

Figure 5.4 Relative position of spacecraft No.2 (from $R_1 = 50m$ to $R_2 = 25m$) 74

Figure 5.5 Relative position of spacecraft No.3 ($R = 50m$) 75
Figure 5.6 Control input of spacecraft No.1 (from $R_1 = 50m$ to $R_2 = 100m$) 75
Figure 5.7 Control input of spacecraft No.2 (from $R_1 = 50m$ to $R_2 = 25m$) 76
Figure 5.8 Control input of spacecraft No.3 ($R = 50m$) 76
Figure 5.9 Exaggerated orbit size formation flying scenario along halo orbit (from $R_1 = 2,000km$ to $R_2 = 3,000km$) 77
Figure 5.10 Relative trajectory of spacecraft with respect to the reference LPO under Xu's HSP controller (with and without disturbance, $G_1 = G_2 = 300$, $G_3 = 200$, $\Delta = 0$) . . . 79
Figure 5.11 Relative distance and velocity with respect to the reference LPO under Xu's HSP controller (with and without disturbance, $G_1 = G_2 = 300$, $G_3 = 200$, $\Delta = 0$) 80
Figure 5.12 Position and velocity estimation error without navigation error 83
Figure 5.13 Disturbance estimation error without navigation error . 84
Figure 5.14 Position and velocity estimation error with navigation error ($1\sigma_{x,y,z} = 1$ km) 85
Figure 5.15 Disturbance estimation error with navigation error ($1\sigma_{x,y,z} = 1$ km) 86
Figure 5.16 Control input history with navigation error ($1\sigma_{x,y,z} = 1$ km) 87
Figure 5.17 Position and velocity estimation error with different observer pole 88

Figure 5.18 Disturbance estimation error with different observer pole 89
Figure 5.19 LPO position and velocity tracking error (during 10 periods) 91
Figure 5.20 Control input history (during 10 periods) 92
Figure 5.21 LPO position and velocity tracking error depending on potential shaping control change 95
Figure 5.22 Relative trajectory of spacecraft with respect to the reference LPO without navigation error and energy dissipation control 96
Figure 5.23 Distance of spacecraft with respect to the reference LPO without navigation error and energy dissipation control . 97
Figure 5.24 Monodromy matrix eigenvalues of controlled orbit 97
Figure 5.25 Relative trajectory of spacecraft with respect to the reference LPO 99
Figure 5.26 Control input 100
Figure 5.27 Relative trajectory of spacecraft with respect to the reference LPO under potential shaping gain $k_p = 200^2$ . . . 100

Chapter 1

Introduction

1.1 Background and Motivation

As a new era of space exploration begins, various challenging space missions are being planned in several space agencies, e.g., Europa Clipper [1], Martian Moons Exploration (MMX) [2], and Comet Interceptor [3]. To successfully accomplish those challenging deep-space exploration missions, creative and advanced technologies should be developed. Mission design, guidance, navigation, and control are the areas where further technological development is required [4–6].

One of the great obstacles to deep-space exploration is the large amount of propellant consumption required to escape the Earth's gravity. There is significant limitation to the distance that can be reached using remaining fuel after escaping the Earth's gravity. To overcome this difficulty (of course this is not the only reason), the National Aeronautics and Space Administration (NASA) is working on a Lunar Gateway mission, a part of the Artemis program [7]. The Artemis employs a Gateway station in cis-lunar space, specifically in a Near Rectilinear Halo Orbit (NRHO) of the Earth-Moon system's L_2 point, which serves as a pressurized environment for astronaut crews as well as a staging

location for missions to other destinations, e.g., Mars, Asteroids, Distant Retrograde Orbits, and others. The NRHOs are subclass of halo orbit family, whose stability indices are stable or close-to-stable. Due to their stability characteristics, these orbits are potentially useful for the placement of Lunar Gateway for deep-space exploration. Although the stability indices of nominal NRHOs are stable or close-to-stable, NRHOs are not stable in reality due to the effects of forces of other celestial bodies and solar radiation. For this reason, active control techniques should be developed to keep the spacecraft on the desired orbit [8].

Libration point orbits (LPOs) have been studied for a long time because they exist in various binary systems in space, e.g., Sun-Earth system, Sun-Jupiter system, and binary asteroid system [9]. The interest on the LPOs has soared after Farquhar shed light on the availability of these orbits [10]. Trajectories leveraging the LPOs and the associated invariant manifolds allow the spacecraft transfers within the cis-lunar region for lower costs, and therefore many different space missions have been planned using these orbits [3, 11–14]. Among these missions, not only single spacecraft missions but also missions involving multiple spacecraft are planned [15, 16]. More recently, advanced missions utilizing LPO have been studied, including the construction of a lunar far side surface navigation system [17, 18] and an advanced satellite constellation [19]. Therefore, research on the formation flight of multiple spacecraft as well as the station-keeping strategy in the vicinity of unstable LPO is needed. In this dissertation, a novel way of station-keeping and formation flight is presented to prepare upcoming deep-space missions.

1.2 Literature Review

1.2.1 Spacecraft Station-Keeping in the Vicinity of the Libration Point Orbits

Station-keeping strategies can be divided into two categories [20]: One is to leverage the geometrical structure of the phase space around an orbit, and the other is to use the advanced control theory.

In the first approach, the station-keeping technique leveraging the geometrical structure of the phase space makes use of the dynamic characteristics of the circular restricted 3-body problem (CR3BP). Because the dynamic instability of LPO originates from the unstable manifold in the phase space, a controller is designed to cancel out the unstable mode. Accordingly, the control strategy is straightforward and can be considered to be fuel efficient because it compensates only the components causing the motion unstable. Furthermore, this approach offers a new perspective to exploit the inherent dynamic characteristics of the target system in designing the controller. For example, Simo et al. [21] proposed a station-keeping strategy that cancels out the unstable Floquet mode around the halo orbit of the Sun-Earth system. Farres and Jorba [22, 23] analysed the dynamic modes considering the solar radiation pressure, and a station-keeping strategy was proposed to utilize these dynamic modes. Similarly, paying attention to the intrinsic Hamiltonian nature of the CR3BP, Scheeres et al. [24] proposed a Hamiltonian structure-preserving control scheme by utilizing the center manifold of the Hamiltonian system. In spite of these advantages and the possibility of new inspiration for the control methodology, Shirobokov et al. [20] pointed out that it is necessary to improve robustness because the performance of the station-keeping strategy included in this category is somewhat

sensitive to the model uncertainty.

There also have been much research on the second approach of the station-keeping strategy, i.e., the station-keeping technique based on the advanced control theory. It is beneficial because each control theory guarantees the performance as well as the stability of the system. In particular, among various control theories, a robust control theory guaranteeing the control performance under uncertainties is appropriate for deep-space missions. This is because it is difficult to fully identify the deep-space environment in advance [25]. For example, a discrete-time sliding mode controller was designed for station-keeping on the LPO of the Earth-Moon system considering the solar system model [26], and a H_∞ control theory was applied to design a controller [27]. More recently, an active disturbance rejection control scheme was applied for station-keeping to estimate and compensate for the effects of disturbances [28–30], and nonlinear output regulation theory was applied to this problem [31, 32]. Notwithstanding these satisfactory results, there exist several issues to be solved in the station-keeping strategies based on the robust control theory. For instance, the previously mentioned sliding mode control technique or H_∞ control technique must know the adequate upper bound of the model uncertainty to achieve satisfactory control performance, which is difficult to achieve in advance, especially in the deep-space. Conservative specification of the upper bound of uncertainty would sacrifice orbit tracking performance, and the opposite may threaten the stability. On top of that, control theory-based techniques have not been able to exploit the inherent dynamics of LPOs because they approached the station-keeping problem with the framework of "signal processing", and such limitation needs to be addressed.

In summary, the two types of LPO station-keeping strategies have both advantages and disadvantages. If two different strategies are complementarily and efficiently applied together, it would be possible to maintain a more effective station-keeping. However, no studies have applied the two different categories of station-keeping strategies together. In this dissertation, the two different approaches to the LPO station-keeping strategies are combined to exploit the advantages of each method. More specifically, a station-keeping strategy is proposed that overcomes the vulnerability to the uncertainty with the help of robust control techniques while fully exploiting the geometric structure of the phase space around the LPO. For more comprehensive survey on the station-keeping technique for LPO, refer to Ref. [20].

1.2.2 Spacecraft Formation Flight in the Vicinity of the Libration Point Orbits

The concept of spacecraft formation flight in the vicinity of LPO has been discussed for a long time to accomplish high-resolution deep-space observation missions, but unfortunately most of the missions have been cancelled, which include Micro-Arcsecond X-ray Imaging Mission (MAXIM) [33], Terrestrial Planet Finder (TPF) [34], and Darwin [35]. Several missions are still being planned, and the number of missions in these orbital regions are expected to proceed because of their unique dynamic environment [36, 37].

Several studies were conducted to determine the viable region for the loose formation flight around the LPO [38–40]. Locating a formation of spacecraft in these natural low-drift regions leads to a smaller variation in the mutual distance between the spacecraft and the pointing direction of the formation. Triangular

configurations providing good performance in terms of formation keeping without control were also investigated [41]. Tight formation control, however, is required during certain mission phases. For the tight formation control, various controllers have been designed, such as time-varying linear-quadratic controller [42], feedback-linearization-based controller [43], nonlinear adaptive neural network controller [44], optimal periodic controller [45], suboptimal $\theta - D$ controller [46,47], output-regulation theory-based controller [31,32,48], and Kalman filter-based linear-quadratic regulator [49]. In addition to the continuous-time controllers designed for the spacecraft formation flight, discrete-time impulsive controllers were also designed [50–52]. More recently, distributed adaptive synchronization schemes were applied to the formation flight problem [53]. Among previous studies, Scheeres et al. presented a non-traditional, unusual continuous-time controller that achieved relative bounded motion, like a motion of planetary satellites, which could be applicable to the spacecraft formation flight near an unstable LPO [24]. Because the control law proposed by Scheeres preserves the mathematical structure of the system i.e., symplectic Hamiltonian structure, it is called a Hamiltonian structure-preserving controller. After the very first work of Scheeres et al., some researchers extended this control methodology and successfully applied to various LPO missions [54–56]. However, the radius of the bounded motion could not be adjusted using the previous studies on Hamiltonian structure-preserving control, which is a limitation and needs to be addressed. In this study, a switching Hamiltonian structure-preserving strategy is established to adjust the elliptic/circular orbit pattern of spacecraft.

1.3 Contributions

The main contributions of this study are summarized as follows.

Switching strategy for desired relative elliptic/circular trajectory pattern via Hamiltonian structure-preserving control

A switching Hamiltonian structure-preserving controller is proposed to stabilize the spacecraft and make a relative circular trajectory, where its radius can be systematically designed. The original concept of the Hamiltonian structure-preserving control is extended to adjust the elliptic/circular orbit pattern of the spacecraft by means of switching strategy. To achieve the desired relative distances, relative orbital motion is analyzed and a strategy akin to Hohmann transfer is presented.

Hamiltonian structure-based station-keeping controller for unstable libration point orbits mission

A Hamiltonian structure-based controller, which can be used as a baseline controller for LPO station-keeping, is presented. Canonical coordinates are adopted to design a controller that leverages the Hamiltonian nature of the CR3BP. The LPO tracking problem in the CR3BP is redefined as a regulation problem in the non-autonomous Hamiltonian system in terms of tracking error state. The Hamiltonian structure-based controller consists of two parts: i) a potential shaping control which makes the equilibrium point as an isolated minimum point of the tracking error Hamiltonian function without destroying the inherent Hamiltonian structure of the system, and ii) energy dissipation control that makes the trajectory converge to the equilibrium point, that is, the isolated

minimum of the reshaped tracking error Hamiltonian. The overall framework of the Hamiltonian structure-based control is the same as a control method proposed by van der Schaft for an autonomous Hamiltonian system [57]. In this study, the original framework is modified and applied to a nonautonomous Hamiltonian system. Furthermore, the relation between the existing Hamiltonian structure-preserving controller and the proposed controller is discussed.

Filtered extended high-gain observer and stability analysis

A filtered extended high-gain observer with improved noise filtering for deep-space environments, which yields a relatively large navigation error, is presented. The deep-space environment is highly uncertain, and therefore dynamic system cannot be represented as an exact Hamiltonian system. The real system is a "perturbed" Hamiltonian system subject to unmodeled dynamics, external disturbances, and parameter uncertainties. Therefore, performance of the nominal controller may be degraded. To address this problem, the extended high-gain observer technique is adopted to estimate disturbances [58,59]. However, a drawback of the high-gain observer is the severe noise amplification due to high observer gain in the presence of measurement noise [60–63]. Notably, navigation errors become very large in deep-space such as LPOs environment, and therefore the problem of navigation error amplification becomes worse when the extended high-gain observer is used. In this study, to attenuate the measurement noise amplification of the standard extended high-gain observer, an enhanced version of the extended high-gain observer, that is, filtered extended high-gain observer using an integral state feedback [64], is proposed, and its convergence is proven. Furthermore, the stability of the integrated closed-loop

system is analyzed.

1.4 Dissertation Outline

The organization of this study is as follows.

- Chapter 2: Background

  The equations of motion are described for the CR3BP. The equilibrium solutions, periodic solutions, and stability are discussed. The Hamiltonian formalism is adopted to analyze the system.

- Chapter 3: Hamiltonian Structure-Based Control

  Two novel control strategies leveraging the Hamiltonian nature of the system are presented. The switching Hamiltonian structure-preserving control is derived, and its application to spacecraft formation flight around the LPO is discussed. More general control law is derived for Hamiltonian canonical coordinates space, and its application to LPO station-keeping is presented.

- Chapter 4: Filtered Extended High-Gain Observer and Closed-Loop Stability

  Filtered extended high-gain observer is designed for state and disturbance estimation. An integral state feedback is used to filter out the effects of measurement noise. Estimation error convergence analysis is conducted, and the estimation error bounds between typical extended high-gain observer and filtered extended high-gain observer are compared. Furthermore, the stability of entire closed-loop system is analyzed and the LPO tracking error bound is given.

- Chapter 5: Numerical Simulations

  Numerical simulations are performed to demonstrate the performance of the proposed controller and observer. To support the effectiveness of the proposed control scheme, various simulation scenarios are taken into account.

- Chapter 6: Conclusion

  This chapter summarizes the main results of this study and provides suggestions for future work.

Chapter 2

Background

This chapter describes a Circular Restricted Three-Body Problem (CR3BP), equilibrium solution, periodic orbit, and stability. To understand the stability of motion, the equations of motion are analyzed using Hamiltonian formulations.

In this study, the three-dimensional CR3BP is adopted to investigate the motion of a spacecraft. This problem represents a system where two astronomical bodies significantly influence the motion of the third body with negligible mass compared with them. Examples include spacecraft motion in the Earth-Moon and Sun-Earth systems, as well as binary asteroid systems. Though the CR3BP is a simplified model, this model offers valuable insight into the fundamental motions within multi-body systems. Therefore, the CR3BP will serve as a stepping stone to a full n-body problem.

2.1 Circular Restricted Three-Body Problem

In the CR3BP, the motion of a spacecraft is influenced by the gravitational attraction of two massive bodies. The primary body, for example, is the Earth and the secondary body is the Moon, which is defined as the Earth-Moon system. A third body, that is, the spacecraft, is assumed to be massless, and therefore the orbital motions of the two primaries are not affected by the third body. It is further assumed that the two primaries move in circular orbits with respect to the barycenter, and their angular velocity $\boldsymbol{\Omega}_f = [0, 0, \Omega_f]^T \in \mathbb{R}^{3\times 1}$ is constant. In the standard formulation of the CR3BP, the motion of the spacecraft is described relative to a coordinate frame that rotates with the two primaries. The rotating x-axis is directed from the Earth to the Moon, the z-axis is normal to the plane of motion of the primaries, and the y-axis completes the right-handed triad. In general, the quantities in the CR3BP are normalized such that the distance between two primaries as well as the angular velocity of the two primaries are both equal to unity. Also, a normalized mass unit is $M = m_1 + m_2$, where m_i are the masses of the two primaries. By defining a mass ratio $\mu = m_2/M$, the location of each primary can be expressed as $[\mu, 0, 0]^T$ and $[1-\mu, 0, 0]^T$. The rotating frame is illustrated in Fig. 2.1, and the nondimensional equations of motion are expressed in terms of rotating frame coordinates as [65–67]

$$\ddot{x} - 2\Omega_f \dot{y} - \Omega_f^2 x = -\frac{(1-\mu)(x+\mu)}{r_1^3} - \frac{\mu(x-1+\mu)}{r_2^3} \tag{2.1a}$$

$$\ddot{y} + 2\Omega_f \dot{x} - \Omega_f^2 y = -\frac{(1-\mu)y}{r_1^3} - \frac{\mu y}{r_2^3} \tag{2.1b}$$

$$\ddot{z} = -\frac{(1-\mu)z}{r_1^3} - \frac{\mu z}{r_2^3} \tag{2.1c}$$

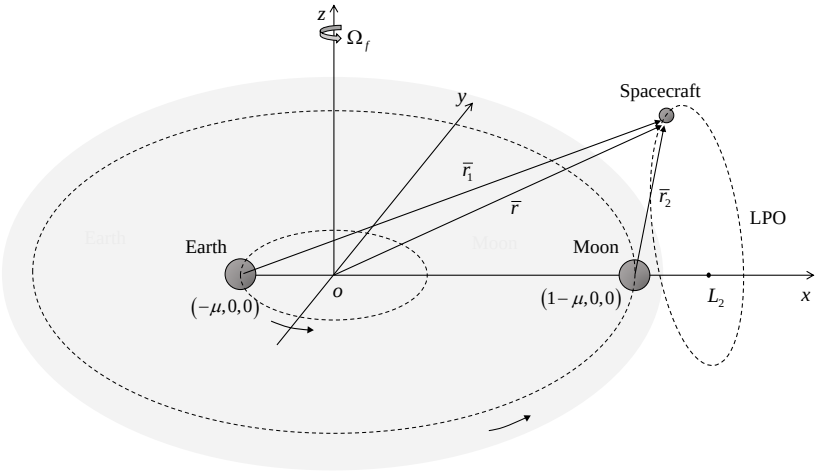

Figure 2.1 Geometry of the CR3BP.

where (x, y, z) are the components of spacecraft position, and $r_1 = \sqrt{(x+\mu)^2 + y^2 + z^2}$ and $r_2 = \sqrt{(x-1+\mu)^2 + y^2 + z^2}$ are nondimensional distances between the spacecraft and two primaries, respectively. Note that all derivatives are evaluated with respect to a rotating observer.

Now, let us consider the following pseudo-potential function $U(\mathbf{r})$,

$$U(\mathbf{r}) = -V(\mathbf{r}) - \Phi(\mathbf{r}) \tag{2.2}$$

where $\mathbf{r} = [x, y, z]^T \in \mathbb{R}^{3\times 1}$ denotes a position vector of spacecraft, $V(\mathbf{r})$ is the non-dimensional gravitational potential function of the two primaries, and $\Phi(\mathbf{r})$ is the non-dimensional potential due to the rotation of the reference frame, which are defined as follows,

$$V(\mathbf{r}) = -\frac{1-\mu}{r_1} - \frac{\mu}{r_2} \tag{2.3}$$

$$\Phi(\mathbf{r}) = -\frac{1}{2}(\boldsymbol{\Omega}_f \times \mathbf{r}) \cdot (\boldsymbol{\Omega}_f \times \mathbf{r}) \tag{2.4}$$

Then, Eq. (2.1) can be written more compactly as

$$\ddot{x} - 2\Omega_f \dot{y} = \nabla_x U(\mathbf{r}) \tag{2.5a}$$

$$\ddot{y} + 2\Omega_f \dot{x} = \nabla_y U(\mathbf{r}) \tag{2.5b}$$

$$\ddot{z} = \nabla_z U(\mathbf{r}) \tag{2.5c}$$

More details about the derivation of CR3BP can be found in [65–67].

2.1.1 Equilibrium Solutions and Periodic Orbits

If the CR3BP is formulated in terms of the rotating frame, it is possible to identify five equilibrium solutions, i.e., libration points, which include three collinear points (L_1,L_2,L_3) and two equilateral points (L_4,L_5). For the Earth-Moon system, the eigenvalues corresponding to the collinear libration points indicate that these points possess a topological structure of the type saddle×center×center. Two pairs of imaginary roots indicate that the center subspace is four-dimensional and oscillatory behavior exists in the vicinity of the libration point for the linear system. Furthermore, the existence of periodic and quasi-periodic orbits still persists in nonlinear models [68–70]. These periodic and quasi-periodic orbits are called libration point orbits (LPOs), which will be the gateway to the various future deep-space missions [7,10,13,15,71,72]. Sample solutions of periodic orbit in the vicinity of the L_1 and L_2 are shown in Figs. 2.2 $\sim$ 2.4. To design nominal orbits, single or multiple differential correction algorithms were employed [73, 74].

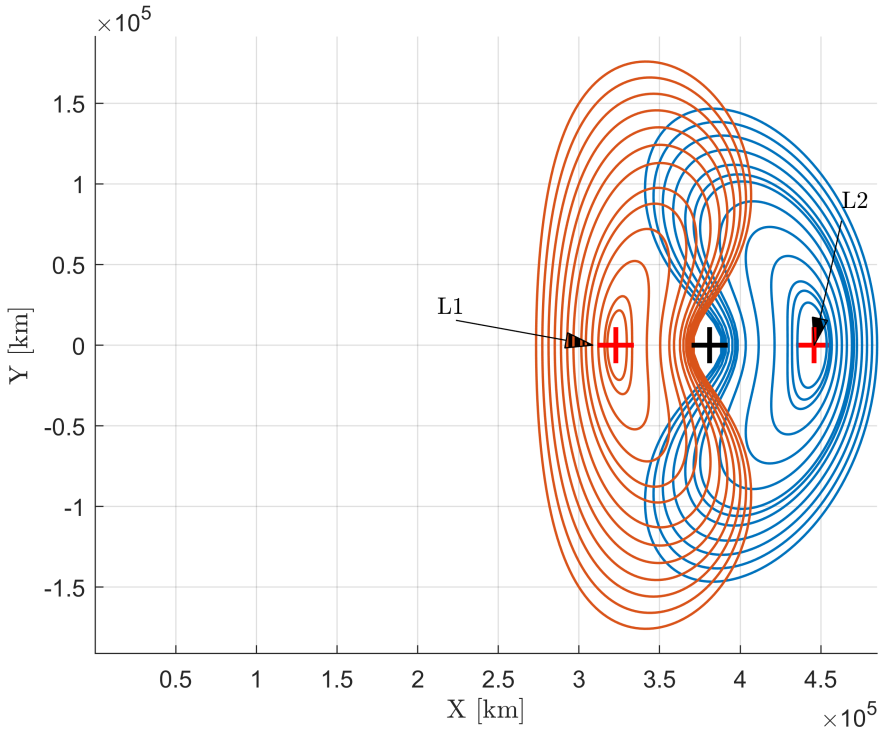

Figure 2.2 Sample member from the $L_1 and L_2$ families of planar lyapunov orbits in the Earth-Moon system

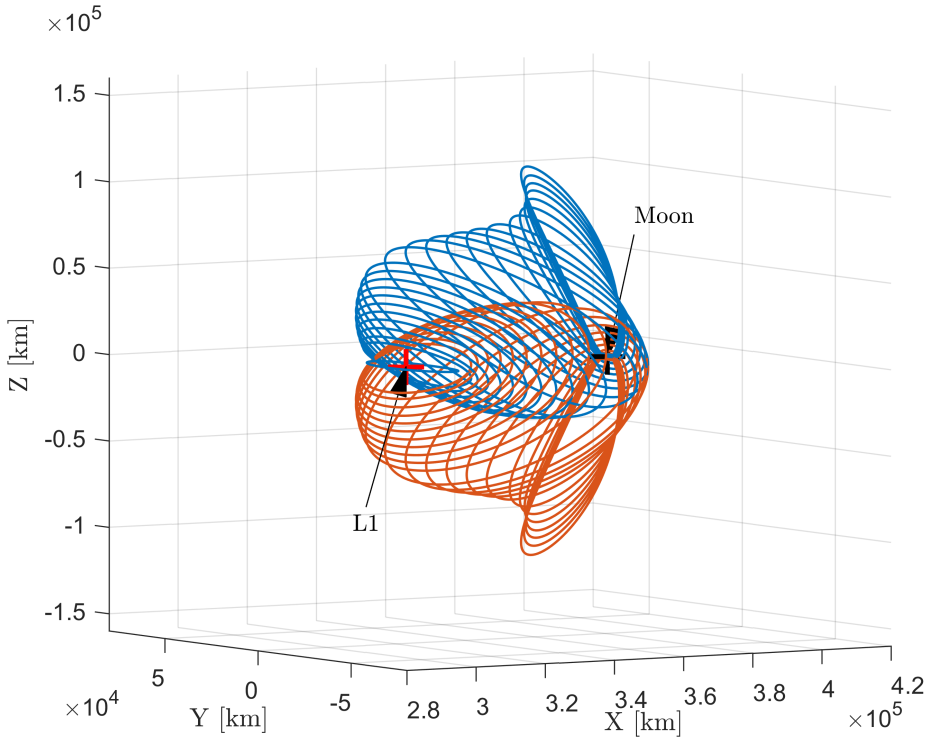

Figure 2.3 Sample member from the L_1 families of halo orbits in the Earth-Moon system

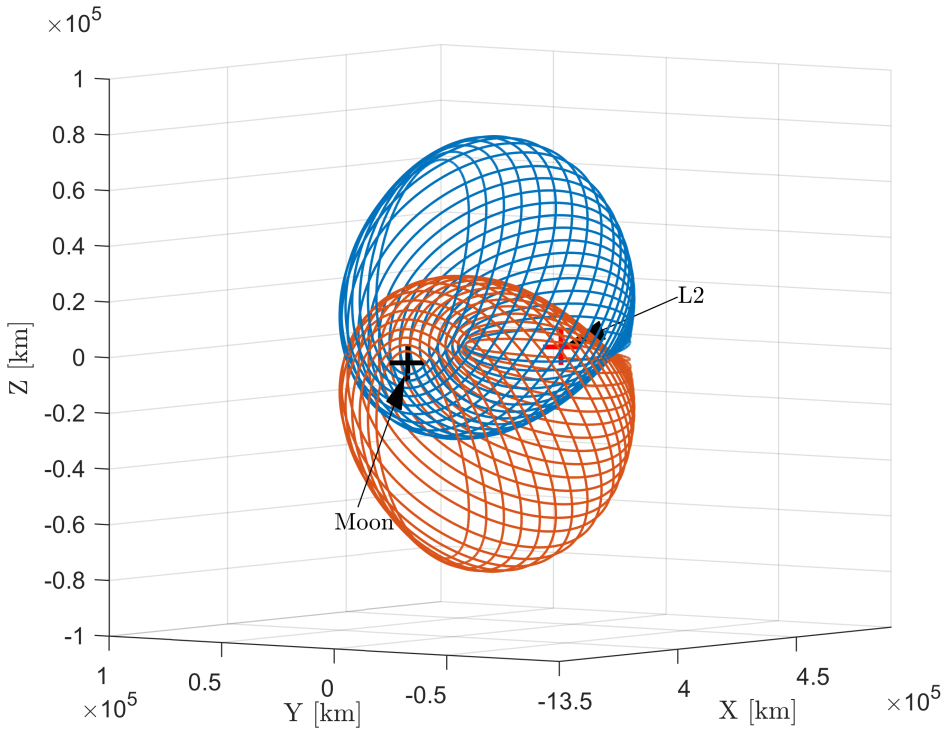

Figure 2.4 Sample member from the L_2 families of halo orbits in the Earth-Moon system

2.1.2 Stability of Periodic Orbits

To determine the stability of a periodic orbit, linearly approximated equation of motion can be used. Consider the position vector $\mathbf{r} = [x, y, z]^T \in \mathbb{R}^{3\times1}$ and velocity vector $\dot{\mathbf{r}} = [\dot{x}, \dot{y}, \dot{z}]^T \in \mathbb{R}^{3\times1}$ of the spacecraft. Likewise, a reference LPO can be defined as $\mathbf{r}_r = [x_r, y_r, z_r]^T \in \mathbb{R}^{3\times1}$ with velocity $\dot{\mathbf{r}}_r = [\dot{x}_r, \dot{y}_r, \dot{z}_r]^T \in \mathbb{R}^{3\times1}$. Then, linear variational equation along the reference LPO can be defined as

$$\frac{d}{dt}\begin{bmatrix}\mathbf{r}-\mathbf{r}_r\\ \dot{\mathbf{r}}-\dot{\mathbf{r}}_r\end{bmatrix} = \begin{bmatrix}\mathbf{0}_3 & \mathbf{I}_3\\ \nabla^2_{\mathrm{rr}}U(\mathbf{r}_r) & 2\Omega_f\mathbf{J}\end{bmatrix}\begin{bmatrix}\mathbf{r}-\mathbf{r}_r\\ \dot{\mathbf{r}}-\dot{\mathbf{r}}_r\end{bmatrix} \tag{2.6}$$

where

$$\mathbf{J} = \begin{bmatrix}0 & 1 & 0\\ -1 & 0 & 0\\ 0 & 0 & 0\end{bmatrix} \tag{2.7}$$

Note that the term $\nabla^2_{\mathrm{rr}}U(\mathbf{r}_r)$ depends on the reference orbit $\mathbf{r}_r$. That is, it has a periodic value, and therefore Eq. (2.6) is a linear time-periodic equation.

Poincare map or stroboscopic map is a useful tool for analysis of the swirling flows, such as the flow near a periodic orbit [75]. And the linearized Poincare map can be defined by the monodromy matrix $\Phi(T, 0)$, i.e., the state transition matrix with the fixed point for one period (T) of the orbit. Accordingly, the monodromy matrix of Eq. (2.6) can be used to evaluate the stability of the reference orbit. The monodromy matrix of the periodic orbit has eigenvalues that occur in reciprocal pairs. More specifically, periodic orbit possesses at least one pair of unit eigenvalues. If there exists one more pair of unit eigenvalues, a nontrivial center manifold is predicted. In the case of L_2 halo orbit families of the Earth-Moon system, most monodromy matrix has at least one reciprocal pair

of real eigenvalues $\lambda_s = 1/\lambda_u$. Accordingly, most halo orbit is unstable, and the uncontrolled motion will diverge from the orbit because of the presence of the unstable manifold. A more detailed description of the eigenvalue distribution of the monodromy matrix depending on the type of periodic orbit can be found in [76].

2.2 Hamiltonian Mechanics

2.2.1 Hamiltonian Approach to CR3BP

A Hamiltonian system is defined as a set of $2n$ differential equations written as [77]

$$\begin{bmatrix} \dot{\mathbf{q}} \\ \dot{\mathbf{p}} \end{bmatrix} = \begin{bmatrix} \mathbf{0}_n & \mathbf{I}_n \\ -\mathbf{I}_n & \mathbf{0}_n \end{bmatrix} \begin{bmatrix} \frac{\partial \mathcal{H}(\mathbf{q},\mathbf{p},t)}{\partial \mathbf{q}}^T \\ \frac{\partial \mathcal{H}(\mathbf{q},\mathbf{p},t)}{\partial \mathbf{p}}^T \end{bmatrix} \tag{2.8}$$

Equation (2.8) is known as the Hamilton's equation with generalized coordinates $\mathbf{q}$, generalized momenta $\mathbf{p}$, and a Hamiltonian function $\mathcal{H}(\mathbf{q}, \mathbf{p}, t)$. If the Hamiltonian function is not explicitly time dependent, i.e., $\mathcal{H}(\mathbf{q}, \mathbf{p}, t) = \mathcal{H}(\mathbf{q}, \mathbf{p})$, then the value of the Hamiltonian is constant, where the constant equals the total energy of the system.

According to Hamiltonian formalism, the CR3BP can be classified as an autonomous Hamiltonian system. Thus, the equations of motion in the CR3BP, Eq. (2.5), can be derived using Lagrangian and Legendre transformation. The Lagrangian of the CR3BP is defined as follows,

$$\begin{aligned} \mathcal{L}(\mathbf{r}, \dot{\mathbf{r}}) &= \mathcal{K}(\mathbf{r}, \dot{\mathbf{r}}) - V(\mathbf{r}) \\ &= \frac{1}{2}\{(\dot{x} - \Omega_f y)^2 + (\dot{y} + \Omega_f x)^2 + z^2\} + \frac{1-\mu}{r_1} + \frac{\mu}{r_2} \end{aligned} \tag{2.9}$$

where $\mathcal{K}(\mathbf{r}, \dot{\mathbf{r}})$ is the kinetic energy of the spacecraft in the CR3BP.

Let us consider the following Legendre transformation with generalized coordinates $\mathbf{q} = [q_1, q_2, q_3]^T \in \mathbb{R}^{3\times 1}$ and generalized momenta $\mathbf{p} = [p_1, p_2, p_3]^T \in \mathbb{R}^{3\times 1}$.

$$\begin{bmatrix} \mathbf{q} \\ \mathbf{p} \end{bmatrix} = \begin{bmatrix} \mathbf{I}_3 & \mathbf{0}_3 \\ -\Omega_f \mathbf{J} & \mathbf{I}_3 \end{bmatrix} \begin{bmatrix} \mathbf{r} \\ \dot{\mathbf{r}} \end{bmatrix} \tag{2.10}$$

Then, Eq. (2.5) can be transformed into the following form of Hamilton's canonical equations.

$$\dot{q}_1 = \frac{\partial \mathcal{H}}{\partial p_1} = p_1 + \Omega_f q_2 \tag{2.11a}$$

$$\dot{q}_2 = \frac{\partial \mathcal{H}}{\partial p_2} = p_2 - \Omega_f q_1 \tag{2.11b}$$

$$\dot{q}_3 = \frac{\partial \mathcal{H}}{\partial p_3} = p_3 \tag{2.11c}$$

$$\dot{p}_1 = -\frac{\partial \mathcal{H}}{\partial q_1} = \Omega_f p_2 - \frac{(1-\mu)(q_1+\mu)}{r_1^3} - \frac{\mu(q_1-1+\mu)}{r_2^3} \tag{2.11d}$$

$$\dot{p}_2 = -\frac{\partial \mathcal{H}}{\partial q_2} = -\Omega_f p_1 - \frac{(1-\mu)q_2}{r_1^3} - \frac{\mu q_2}{r_2^3} \tag{2.11e}$$

$$\dot{p}_3 = -\frac{\partial \mathcal{H}}{\partial q_3} = -\frac{(1-\mu)q_3}{r_1^3} - \frac{\mu q_3}{r_2^3} \tag{2.11f}$$

with the following Hamiltonian function.

$$\begin{aligned} \mathcal{H}(\mathbf{q}, \mathbf{p}) &= \mathbf{p}^T \dot{\mathbf{q}} - \mathcal{L}(\mathbf{q}, \dot{\mathbf{q}}) \\ &= \frac{1}{2}\mathbf{p}^T\mathbf{p} + \Omega_f \mathbf{p}^T \mathbf{J}\mathbf{q} + V(\mathbf{q}) \\ &= \frac{1}{2}(p_1^2 + p_2^2 + p_3^2) + \Omega_f(p_1 q_2 - p_2 q_1) - \frac{1-\mu}{r_1} - \frac{\mu}{r_2} \end{aligned} \tag{2.12}$$

where $r_1 = \sqrt{(q_1+\mu)^2 + q_2^2 + q_3^2}$, and $r_2 = \sqrt{(q_1-1+\mu)^2 + q_2^2 + q_3^2}$.

2.2.2 Hamiltonian Approach to LPO Tracking Problem

Let us consider a reference LPO that can be defined as $\mathbf{r}_r$ with velocity $\dot{\mathbf{r}}_r$. The corresponding generalized coordinates/momenta can be defined as $\mathbf{q}_r =$

$[q_{r_1}, q_{r_2}, q_{r_3}]^T \in \mathbb{R}^{3\times 1}$, and $\mathbf{p}_r = [p_{r_1}, p_{r_2}, p_{r_3}]^T \in \mathbb{R}^{3\times 1}$, respectively. Since LPOs are one of the solutions to the CR3BP, they are also governed by the Hamilton's equations with the following Hamiltonian function.

$$\begin{aligned}\mathcal{H}(\mathbf{q}_r, \mathbf{p}_r) &= \mathbf{p}_r^T \dot{\mathbf{q}}_r - \mathcal{L}(\mathbf{q}_r, \dot{\mathbf{q}}_r) \\ &= \frac{1}{2}\mathbf{p}_r^T \mathbf{p}_r + \Omega_f \mathbf{p}_r^T \mathbf{J}\mathbf{q}_r + V(\mathbf{q}_r) \\ &= \frac{1}{2}(p_{r_1}^2 + p_{r_2}^2 + p_{r_3}^2) + \Omega_f(p_{r_1}q_{r_2} - p_{r_2}q_{r_1}) - \frac{1-\mu}{r_{r_1}} - \frac{\mu}{r_{r_2}}\end{aligned} \tag{2.13}$$

where $r_{r_1} = \sqrt{(q_{r_1} + \mu)^2 + q_{r_2}^2 + q_{r_3}^2}$, and $r_{r_2} = \sqrt{(q_{r_1} - 1 + \mu)^2 + q_{r_2}^2 + q_{r_3}^2}$.

Now, let us define the generalized tracking error coordinates/momenta between the trajectory of the spacecraft and reference LPO as $\mathbf{e}_q \triangleq \mathbf{q} - \mathbf{q}_r \in \mathbb{R}^{3\times 1}$ and $\mathbf{e}_p \triangleq \mathbf{p} - \mathbf{p}_r \in \mathbb{R}^{3\times 1}$, respectively. Then, the generalized tracking error coordinates/momenta dynamics can be written as follows,

$$\dot{\mathbf{e}}_q^T = \frac{\partial \mathcal{H}(\mathbf{q}, \mathbf{p})}{\partial \mathbf{p}} - \frac{\partial \mathcal{H}(\mathbf{q}_r, \mathbf{p}_r)}{\partial \mathbf{p}_r} \tag{2.14a}$$

$$\dot{\mathbf{e}}_p^T = -\frac{\partial \mathcal{H}(\mathbf{q}, \mathbf{p})}{\partial \mathbf{q}} + \frac{\partial \mathcal{H}(\mathbf{q}_r, \mathbf{p}_r)}{\partial \mathbf{q}_r} \tag{2.14b}$$

A tracking error Hamiltonian function can be defined as

$$\begin{aligned}\mathcal{H}_e(\mathbf{e}_q, \mathbf{e}_p, \mathbf{q}_r, \mathbf{p}_r) &\triangleq \mathcal{H}(\mathbf{q}, \mathbf{p}) + \mathcal{H}(\mathbf{q}_r, \mathbf{p}_r) \\ &= \mathcal{H}(\mathbf{e}_q + \mathbf{q}_r, \mathbf{e}_p + \mathbf{p}_r) + \mathcal{H}(\mathbf{q}_r, \mathbf{p}_r)\end{aligned} \tag{2.15}$$

Then, we have

$$\begin{aligned}\frac{\partial \mathcal{H}_e}{\partial \mathbf{e}_q} &= \frac{\partial \mathcal{H}(\mathbf{q}, \mathbf{p})}{\partial \mathbf{e}_q} + \frac{\partial \mathcal{H}(\mathbf{q}_r, \mathbf{p}_r)}{\partial \mathbf{e}_q} \\ &= \frac{\partial \mathcal{H}(\mathbf{q}, \mathbf{p})}{\partial \mathbf{q}} \frac{\partial \mathbf{q}}{\partial \mathbf{e}_q} + \frac{\partial \mathcal{H}(\mathbf{q}_r, \mathbf{p}_r)}{\partial \mathbf{q}_r} \frac{\partial \mathbf{q}_r}{\partial \mathbf{e}_q} \\ &= \frac{\partial \mathcal{H}(\mathbf{q}, \mathbf{p})}{\partial \mathbf{q}} - \frac{\partial \mathcal{H}(\mathbf{q}_r, \mathbf{p}_r)}{\partial \mathbf{q}_r}\end{aligned} \tag{2.16a}$$

$$\begin{aligned}\frac{\partial \mathcal{H}_e}{\partial \mathbf{e}_p} &= \frac{\partial \mathcal{H}(\mathbf{q},\mathbf{p})}{\partial \mathbf{e}_p} + \frac{\partial \mathcal{H}(\mathbf{q}_r,\mathbf{p}_r)}{\partial \mathbf{e}_p} \\ &= \frac{\partial \mathcal{H}(\mathbf{q},\mathbf{p})}{\partial \mathbf{p}}\frac{\partial \mathbf{p}}{\partial \mathbf{e}_p} + \frac{\partial \mathcal{H}(\mathbf{q}_r,\mathbf{p}_r)}{\partial \mathbf{p}_r}\frac{\partial \mathbf{p}_r}{\partial \mathbf{e}_p} \\ &= \frac{\partial \mathcal{H}(\mathbf{q},\mathbf{p})}{\partial \mathbf{p}} - \frac{\partial \mathcal{H}(\mathbf{q}_r,\mathbf{p}_r)}{\partial \mathbf{p}_r}\end{aligned} \tag{2.16b}$$

Using Eqs. (2.14) and (2.16), the generalized tracking error coordinates/momenta dynamic equations with control input can be rewritten as

$$\dot{\mathbf{e}}_q^T = \frac{\partial \mathcal{H}_e(\mathbf{e}_q,\mathbf{e}_p,\mathbf{q}_r,\mathbf{p}_r)}{\partial \mathbf{e}_p} \tag{2.17a}$$

$$\dot{\mathbf{e}}_p^T = -\frac{\partial \mathcal{H}_e(\mathbf{e}_q,\mathbf{e}_p,\mathbf{q}_r,\mathbf{p}_r)}{\partial \mathbf{e}_q} + \mathbf{u}^T \tag{2.17b}$$

Note that $\mathbf{u} \in \mathbb{R}^{3\times 1}$ represents the control input which is required to be designed for station-keeping or formation flight. If $\mathbf{u} = \mathbf{0}$, the tracking error dynamics between the trajectory of the spacecraft and the reference LPO can be considered to be a non-autonomous Hamiltonian system.

In this chapter, the LPO tracking problem was redefined as a regulation problem in the non-autonomous Hamiltonian system in terms of the tracking error. In the following chapters, control input $\mathbf{u}$ will be designed to make the errors $(\mathbf{e}_q, \mathbf{e}_p)$ converge to zero leveraging the Hamiltonian nature of the system.

Chapter 3

Hamiltonian Structure-Based Control

In celestial mechanics and astrodynamics, most of the dynamic problems can be fall into a Hamiltonian system. For this reason, understanding and exploiting the physical and mathematical properties of the Hamiltonian system have a wide range of applications in related problems [78]. In this regard, several studies have investigated to leverage the natural center manifold of the Hamiltonian system in spacecraft formation flight missions [79, 80]. However, the use of the natural center manifold around LPO is restrictive because the existence of the unstable manifold makes the center manifold practically unstable, and also the rotation frequency of the center manifold is slow compared to the period of the LPO. To address these issues, Scheeres et al. [24] conducted fundamental research on the spacecraft formation flight using an artificial center manifold instead of the natural center manifold around the LPO. Since the earliest work of Scheeres et al., the control scheme using the bounded motion of the Hamiltonian system has been studied under the name of Hamiltonian structure-preserving control [54–56, 81–86]. Because the Hamiltonian structure-preserving control makes the system marginally stable instead of asymptotically stable, the resulting motion of the Hamiltonian structure-preserving control provides a bounded trajectory like a motion of planetary satellites instead of a

converging trajectory.

This chapter proposes two novel control strategies by extending existing Hamiltonian structure-preserving control: i) One is a switching Hamiltonian structure-preserving control, and ii) the other is an energy dissipation control. Switching Hamiltonian structure-preserving control extends the original concept of Hamiltonian structure-preserving control using the switching control strategy. The proposed switching Hamiltonian structure-preserving controller can systematically adjust the radius of orbit to the desired one, which was not possible by the existing Hamiltonian structure-preserving controllers. Energy dissipation control is designed to break the Hamiltonian structure by adding dissipative forces. Consequently, spacecraft motion can converge to desired points or trajectories.

3.1 Classical Linear Hamiltonian Structure-Preserving Control

Note that the nonlinear CR3BP as well as the linear variational equation is a Hamiltonian system, and therefore Eq. (2.6) can be transformed into the linear form of Hamilton's equations using Legendre transformation, Eq. (2.10), as

$$\frac{d}{dt}\begin{bmatrix}\mathbf{e}_q\\ \mathbf{e}_p\end{bmatrix} = \begin{bmatrix}\mathbf{I}_3 & \mathbf{0}_3\\ -\Omega_f\mathbf{J} & \mathbf{I}_3\end{bmatrix}\begin{bmatrix}\mathbf{0}_3 & \mathbf{I}_3\\ \nabla^2_{\mathrm{qq}}U(\mathbf{q}_r) & 2\Omega_f\mathbf{J}\end{bmatrix}\begin{bmatrix}\mathbf{I}_3 & \mathbf{0}_3\\ -\Omega_f\mathbf{J} & \mathbf{I}_3\end{bmatrix}^{-1}\begin{bmatrix}\mathbf{e}_q\\ \mathbf{e}_p\end{bmatrix} \tag{3.1}$$

with the following Hamiltonian function.

$$\begin{aligned}\mathcal{H}_{e,2}(\mathbf{e}_q,\mathbf{e}_p) &= \frac{1}{2}\begin{bmatrix}\mathbf{e}_q^T & \mathbf{e}_p^T\end{bmatrix}\begin{bmatrix}\mathbf{0}_3 & -\mathbf{I}_3\\ \mathbf{I}_3 & \mathbf{0}_3\end{bmatrix}\begin{bmatrix}\mathbf{I}_3 & \mathbf{0}_3\\ -\Omega_f\mathbf{J} & \mathbf{I}_3\end{bmatrix}\begin{bmatrix}\mathbf{0}_3 & \mathbf{I}_3\\ \nabla^2_{\mathrm{qq}}U(\mathbf{q}_r) & 2\Omega_f\mathbf{J}\end{bmatrix}\begin{bmatrix}\mathbf{I}_3 & \mathbf{0}_3\\ -\Omega_f\mathbf{J} & \mathbf{I}_3\end{bmatrix}^{-1}\begin{bmatrix}\mathbf{e}_q\\ \mathbf{e}_p\end{bmatrix}\\ &= \frac{1}{2}\begin{bmatrix}\mathbf{e}_q^T & \mathbf{e}_p^T\end{bmatrix}\begin{bmatrix}-\nabla^2_{\mathrm{qq}}U(\mathbf{q}_r)-\Omega_f^2\mathbf{J}\mathbf{J} & -\Omega_f\mathbf{J}\\ \Omega_f\mathbf{J} & \mathbf{I}_3\end{bmatrix}\begin{bmatrix}\mathbf{e}_q\\ \mathbf{e}_p\end{bmatrix}\end{aligned} \tag{3.2}$$

Then, the linear Hamilton's canonical equations are expressed as

$$\dot{e}_{q_1} = \frac{\partial\mathcal{H}_{e,2}}{\partial e_{p_1}} = e_{p_1} + \Omega_f e_{q_2} \tag{3.3a}$$

$$\dot{e}_{q_2} = \frac{\partial\mathcal{H}_{e,2}}{\partial e_{p_2}} = e_{p_2} - \Omega_f e_{q_1} \tag{3.3b}$$

$$\dot{e}_{q_3} = \frac{\partial\mathcal{H}_{e,2}}{\partial e_{p_3}} = e_{p_3} \tag{3.3c}$$

$$\begin{aligned}\dot{e}_{p_1} &= -\frac{\partial\mathcal{H}_{e,2}}{\partial e_{q_1}}\\ &= \Omega_f e_{p_2} + (\nabla^2_{q_1q_1}U(\mathbf{q}_r) - \Omega_f^2)e_{q_1} + \nabla^2_{q_1q_2}U(\mathbf{q}_r)e_{q_2} + \nabla^2_{q_1q_3}U(\mathbf{q}_r)e_{q_3}\end{aligned} \tag{3.3d}$$

$$\begin{aligned}\dot{e}_{p_2} &= -\frac{\partial \mathcal{H}_{e,2}}{\partial e_{q_2}} \\ &= -\Omega_f e_{p_1} + \nabla^2_{q_1 q_2} U(\mathbf{q}_r) e_{q_1} + (\nabla^2_{q_2 q_2} U(\mathbf{q}_r) - \Omega_f^2) e_{q_2} + \nabla^2_{q_2 q_3} U(\mathbf{q}_r) e_{q_3}\end{aligned} \tag{3.3e}$$

$$\begin{aligned}\dot{e}_{p_3} &= -\frac{\partial \mathcal{H}_{e,2}}{\partial e_{q_3}} \\ &= \nabla^2_{q_1 q_3} U(\mathbf{q}_r) e_{q_1} + \nabla^2_{q_2 q_3} U(\mathbf{q}_r) e_{q_2} + \nabla^2_{q_3 q_3} U(\mathbf{q}_r) e_{q_3}\end{aligned} \tag{3.3f}$$

where

$$e_{p_1} = -\Omega_f e_{q_2} + \dot{e}_{q_1} \tag{3.4a}$$

$$e_{p_2} = \Omega_f e_{q_1} + \dot{e}_{q_2} \tag{3.4b}$$

$$e_{p_3} = \dot{e}_{q_3} \tag{3.4c}$$

Note from Eq. (2.6) that the tracking error dynamics of spacecraft in the vicinity of reference LPO can be written as

$$\ddot{\mathbf{e}}_r - 2\Omega_f \mathbf{J}\dot{\mathbf{e}}_r - \nabla^2_{\mathrm{rr}} U(\mathbf{r}_r)\mathbf{e}_r = \mathbf{0} \tag{3.5}$$

where $\mathbf{e}_r \triangleq \mathbf{r} - \mathbf{r}_r \in \mathbb{R}^{3\times 1}$. Substituting Eq.(3.4) into Eq. (3.3) shows that Eq. (3.3) and Eq. (3.5) are equivalent.

To stabilize the motion of spacecraft, let us consider the following control input $\mathbf{T_c}$.

$$\mathbf{T_c} = \mathbf{T}\mathbf{e}_r + \mathbf{K}\dot{\mathbf{e}}_r \tag{3.6}$$

Then, the equation of motion in the closed-loop system can be written as

$$\ddot{\mathbf{e}}_r - (2\Omega_f \mathbf{J} + \mathbf{K})\dot{\mathbf{e}}_r - (\nabla^2_{\mathrm{rr}} U(\mathbf{r}_r) + \mathbf{T})\mathbf{e}_r = \mathbf{0} \tag{3.7}$$

From Eqs. (3.3) and (3.7), in order for the Hamiltonian structure of the system to be maintained even after the control input is applied to the system, $\mathbf{T}$ must

have the same structure as $\nabla^2_{\mathrm{rr}} U(\mathbf{r}_r)$, and $\mathbf{K}$ must have the same structure as $\mathbf{J}$. In other words, the control input conditions to preserve the symplectic Hamiltonian structure are as follows: i) $\mathbf{T}$ is a symmetric matrix, and ii) $\mathbf{K}$ is a skew symmetric matrix [24, 87].

The controllers in the previous works [24, 54, 56] are examples of feedback control law that satisfy the above conditions, and the specific form of control input can be found in each article. The common form of the Hamiltonian structure-preserving control proposed in the previous studies is to compensate for the position errors in the stable, unstable, and center eigenspace directions. The principle of the Hamiltonian structure-preserving controller is to stabilize the motion of spacecraft over a long time by stabilizing the relative motion over a short time. Note that the stabilization of the relative motion over a short term is necessary but not sufficient to ensure that the motion of the spacecraft is stable over a long term. For this reason, long term stabilization with respect to LPO, that is the ultimate goal of the mission, is evaluated by computing the eigenvalues of the monodromy matrix. More details about the classical linear Hamiltonian structure-preserving control can be found in [24, 56, 88].

3.2 Switching Hamiltonian Structure-Preserving Control

Because the Hamiltonian structure-preserving control makes the system marginally stable instead of asymptotically stable, the resultant motion yields a bounded trajectory. Due to this feature of the Hamiltonian structure-preserving control, it is difficult to design a relative trajectory of the spacecraft. In other words, using the Hamiltonian structure-preserving control, it is difficult to make

the spacecraft exactly track the reference orbit. As a result, all the previous studies have only focused on the stabilization, not the configuration of the relative motion of spacecraft. In this section, a novel switching Hamiltonian structure-preserving controller is proposed to overcome this limitation. More specifically, a switching Hamiltonian structure-preserving controller is proposed to stabilize the spacecraft and make a circular relative trajectory, where the radius of the circular relative trajectory can be systematically adjusted.

First, let us rewrite Eq. (3.7) as

$$\ddot{\mathbf{e}}_r - \mathbf{S}\dot{\mathbf{e}}_r - \tilde{\mathbf{U}}\mathbf{e}_r = \mathbf{0} \tag{3.8}$$

where $\mathbf{S} \triangleq (2\Omega_f \mathbf{J} + \mathbf{K})$ and $\tilde{\mathbf{U}} \triangleq (\nabla^2_{\mathrm{rr}} U(\mathbf{r}_r) + \mathbf{T})$. Note that the negative definiteness of $\tilde{\mathbf{U}}$ is a sufficient condition for the stability of the equilibrium points in the linear sense. Because $\tilde{\mathbf{U}}$ is only affected by the position error feedback, the velocity error feedback is not essential to ensure stability. To make the design of the relative trajectory of the spacecraft easy, the velocity error feedback controller is designed to null out the Coriolis force, that is, $\mathbf{S} = \mathbf{0}$. In other words, the position error feedback control matrix $\mathbf{T}$ and velocity error feedback control matrix $\mathbf{K}$ are designed as follows,

$$\mathbf{T} = \tilde{\mathbf{U}} - \nabla^2_{\mathrm{rr}} U(\mathbf{r}_r) \tag{3.9a}$$

$$\mathbf{K} = -2\Omega_f \mathbf{J} \tag{3.9b}$$

Then, the closed-loop system becomes

$$\ddot{\mathbf{e}}_r - \tilde{\mathbf{U}}\mathbf{e}_r = \mathbf{0} \tag{3.10}$$

with a negative definite matrix $\tilde{\mathbf{U}}$. Because $\tilde{\mathbf{U}}$ is symmetric, it is always orthogonally diagonalizable as

$$\tilde{\mathbf{U}} = \mathbf{M}\mathbf{\Lambda}\mathbf{M}^{-1} \tag{3.11}$$

where $\mathbf{M}$ denotes an orthogonal eigenvector matrix of $\tilde{\mathbf{U}}$, and $\mathbf{\Lambda}$ denotes a diagonalized matrix of $\tilde{\mathbf{U}}$. Let us define a new variable $\mathbf{e}_g \triangleq \mathbf{M}^{-1}\mathbf{e}_r$. Then, Eq. (3.10) can be rewritten as

$$\ddot{\mathbf{e}}_g - \mathbf{\Lambda}\mathbf{e}_g = \mathbf{0} \tag{3.12}$$

where $\mathbf{e}_g$ is a new representation of $\mathbf{e}_r$ with respect to the eigenvector matrix $\mathbf{M}$. Note from Eq. (3.12) that the relative motion of spacecraft can be understood as a combination of three simple harmonic oscillations. Therefore, designing the relative motion of the spacecraft implies constructing a linear combination of three simple harmonic oscillations. Eventually, constructing a linear combination of three simple harmonic oscillations is to design matrix $\mathbf{\Lambda}$.

For the design of matrix $\mathbf{\Lambda}$, the relative motion of the spacecraft should be analyzed. The relative motion of the spacecraft can be written as follows,

$$\begin{aligned}
\mathbf{e}_r(t) &= \mathbf{M}\begin{bmatrix} e_{g_1}(t) \\ e_{g_2}(t) \\ e_{g_3}(t) \end{bmatrix} \\
&= \begin{bmatrix} \bar{\mathbf{h}}_1 & \bar{\mathbf{h}}_2 & \bar{\mathbf{h}}_3 \end{bmatrix}\begin{bmatrix} e_{g_1}(t) \\ e_{g_2}(t) \\ e_{g_3}(t) \end{bmatrix} \\
&= \sum_{i=1}^{3}[e_{g_i}(t)\bar{\mathbf{h}}_i] \\
&= \sum_{i=1}^{3}\left[\Big\{A_i cos(\omega_i t) + B_i sin(\omega_i t)\Big\}\bar{\mathbf{h}}_i\right]
\end{aligned} \tag{3.13}$$

where A_i and B_i are constant coefficients, ω_i^2 is the magnitude of the eigenvalues of $\tilde{\mathbf{U}}$, and $\bar{\mathbf{h}}_i$ is the orthonormal eigenvectors of the $\tilde{\mathbf{U}}$.

Hsiao et al. [89] showed that the trajectory described by each oscillation

mode forms an elliptical orbit with the origin of frame at the center. Therefore, the relative trajectory is a linear combination of three elliptical orbits. Unfortunately, it is difficult to imagine the actual relative trajectories, which are combinations of three elliptical orbits. Nevertheless, if appropriate initial conditions and mode frequencies, i.e., the eigenvalues, are given, the resulting relative trajectory (that is, combined result of each mode) can be an elliptical/circular orbit. If the conditions of elliptical/circular orbit are known, it is possible to design a switching Hamiltonian-structure preserving controller using the information. With the designed switching controller, the radius of the elliptic/circular orbit can be changed systematically. In addition, if a switching control is applied repeatedly, the position convergence to the reference orbit can be achieved.

Note that Liberzon et al. [90, 91] studied a basic idea of asymptotic stabilization using a state-dependent switching control, and in particular, they discussed a stabilizing switching strategy for the harmonic oscillator which is applicable to the Hamiltonian structure-preserving controller.

In this study, the following cases are discussed: i) transfer from a circular orbit with radius R_1 to an elliptical orbit whose apsis distances are R_1 and R_2, and ii) transfer from an elliptical orbit whose apsis distances are R_1 and R_2 to circular orbit with radius R_2. The basic concept of the switching Hamiltonian structure-preserving control is similar to Hohmann transfer.

First, let us assume that the spacecraft rotates a circular orbit with radius R_1. At any point on the circular orbit, the spacecraft switches the Hamiltonian structure-preserving controller to transfer to the elliptical orbit, whose apsis distances are R_1 and R_2. After transferring to the elliptic orbit, the spacecraft

switches the controller again at the other apsis to transfer to the circular orbit, whose radius is R_2. By following these two switching steps, it is possible to systematically resize the circular orbit of the spacecraft. For the switching strategy, one must know the orbital properties of the spacecraft.

3.2.1 Orbital Properties of Spacecraft

Differentiating Eq. (3.13) with respect to time gives the relative velocity vector as

$$\dot{\mathbf{e}}_r(t) = \sum_{i=1}^{3}\left[\left\{-A_i\omega_i sin(\omega_i t) + B_i\omega_i cos(\omega_i t)\right\}\bar{\mathbf{h}}_i\right] \tag{3.14}$$

To make a relative trajectory elliptical/circular orbit, each mode's frequency should be identical, i.e., $\omega_i = \omega$. If the relative trajectory is an elliptical orbit, the position and velocity vector will be perpendicular to each other at the periapsis and apoapsis. By defining the apsis angle variable $\theta_\perp$, the following equation holds.

$$\begin{aligned}\mathbf{e}_r(t_{aps})\cdot\dot{\mathbf{e}}_r(t_{aps}) &= \left(\sum_{i=1}^{3}\left[\left\{A_i cos(\theta_\perp) + B_i sin(\theta_\perp)\right\}\bar{h}_i\right]\right)\\ &\quad\cdot\left(\sum_{i=1}^{3}\left[\omega\left\{-A_i sin(\theta_\perp) + B_i cos(\theta_\perp)\right\}\bar{h}_i\right]\right)\\ &= \frac{\omega}{2}\left\{\sum_{i=1}^{3}\left(-A_i^2 + B_i^2\right)\right\}sin(2\theta_\perp) + \omega\left\{\sum_{i=1}^{3}\left(A_i B_i\right)\right\}cos(2\theta_\perp) \equiv 0\end{aligned} \tag{3.15}$$

Thus, we have

$$cos(2\theta_\perp) = \pm\frac{\sum_{i=1}^{3}\left(A_i^2 - B_i^2\right)}{\sqrt{\left\{\sum_{i=1}^{3}\left(A_i^2 - B_i^2\right)\right\}^2 + 4\left\{\sum_{i=1}^{3}\left(A_i B_i\right)\right\}^2}} \tag{3.16a}$$

$$sin(2\theta_{\perp}) = \pm \frac{2\left\{\sum_{i=1}^{3}\left(A_i B_i\right)\right\}}{\sqrt{\left\{\sum_{i=1}^{3}\left(A_i^2 - B_i^2\right)\right\}^2 + 4\left\{\sum_{i=1}^{3}\left(A_i B_i\right)\right\}^2}} \tag{3.16b}$$

Using Eqs. (3.13) and (3.16), the square of the periapsis and apoapsis distances can be written as follows,

$$\begin{aligned} |\mathbf{e}_r(t_{aps})|^2 &= \left(\sum_{i=1}^{3}\left[\left\{A_i cos(\theta_{\perp}) + B_i sin(\theta_{\perp})\right\}\bar{\mathbf{h}}_i\right]\right) \cdot \left(\sum_{i=1}^{3}\left[\left\{A_i cos(\theta_{\perp}) + B_i sin(\theta_{\perp})\right\}\bar{\mathbf{h}}_i\right]\right) \\ &= \frac{1}{2}\left\{\sum_{i=1}^{3}\left(A_i^2 + B_i^2\right)\right\} \pm \frac{\frac{1}{2}\left\{\sum_{i=1}^{3}\left(A_i^2 - B_i^2\right)\right\}^2 + 2\left\{\sum_{i=1}^{3}\left(A_i B_i\right)\right\}^2}{\sqrt{\left\{\sum_{i=1}^{3}\left(A_i^2 - B_i^2\right)\right\}^2 + 4\left\{\sum_{i=1}^{3}\left(A_i B_i\right)\right\}^2}} \end{aligned} \tag{3.17}$$

Because the coefficients A_i and B_i of each mode are determined based on the initial conditions, the distance of apsis is also determined by given initial conditions.

3.2.2 Switching Point 1: From a Circular Orbit to an Elliptical Orbit

The position and velocity of spacecraft on the circular orbit of radius R_1 satisfying Eq. (3.10) with a mode frequency ω can be expressed as Eqs. (3.13) and (3.14). Let us take the time at the switching point as $t = 0$. Then, the position and velocity vector can be expressed as

$$\mathbf{e}_r(0) = \sum_{i=1}^{3}(A_i \bar{\mathbf{h}}_i) \tag{3.18a}$$

$$\dot{\mathbf{e}}_r(0) = \omega \sum_{i=1}^{3}(B_i \bar{\mathbf{h}}_i) \tag{3.18b}$$

The objective is to transfer the spacecraft from a circular orbit to an elliptical orbit, whose target apsis distance is R_2. Figure 3.1 shows the concept of the first switching. After switching, the equation of motion becomes Eq. (3.10) with the new mode frequency ω_α. With this switched equation of motion, the position and velocity of the spacecraft are expressed as

$$\mathbf{e}_r(t) = \sum_{i=1}^{3}\left[\left\{C_i cos(\omega_\alpha t) + D_i sin(\omega_\alpha t)\right\}\bar{\mathbf{h}}_i\right] \tag{3.19a}$$

$$\dot{\mathbf{e}}_r(t) = \sum_{i=1}^{3}\left[\left\{-C_i\omega_\alpha sin(\omega_\alpha t) + D_i\omega_\alpha cos(\omega_\alpha t)\right\}\bar{\mathbf{h}}_i\right] \tag{3.19b}$$

Then, we have

$$\mathbf{e}_r(0) = \sum_{i=1}^{3}(C_i\bar{\mathbf{h}}_i) \tag{3.20a}$$

$$\dot{\mathbf{e}}_r(0) = \omega_\alpha\sum_{i=1}^{3}(D_i\bar{\mathbf{h}}_i) \tag{3.20b}$$

At the switching point, the position and velocity vectors before and after switching should be identical. Therefore, following equations are obtained.

$$A_i = C_i \tag{3.21a}$$

$$\omega B_i = \omega_\alpha D_i \tag{3.21b}$$

In addition, if $\omega_\alpha = k\omega$, where k is a real number, then $D_i = B/k$. Under these relations, the square of the periapsis and apoapsis distances can be expressed

as follows,

$$
\begin{aligned}
|\mathbf{e}_r(t_{aps})|^2 &= \frac{1}{2}\left\{\sum_{i=1}^{3}\left(C_i^2 + D_i^2\right)\right\} \\
&\quad \pm \frac{\left[\frac{1}{2}\left\{\sum_{i=1}^{3}(C_i^2 - D_i^2)\right\}^2 + 2\left\{\sum_{i=1}^{3}(C_i D_i)\right\}^2\right]}{\sqrt{\left\{\sum_{i=1}^{3}\left(C_i^2 - D_i^2\right)\right\}^2 + 4\left\{\sum_{i=1}^{3}\left(C_i D_i\right)\right\}^2}} \\
&= \frac{1}{2}\left\{\sum_{i=1}^{3}\left(A_i^2 + \frac{B_i^2}{k^2}\right)\right\} \\
&\quad \pm \frac{\left[\frac{1}{2}\left\{\sum_{i=1}^{3}\left(A_i^2 - \frac{B_i^2}{k^2}\right)\right\}^2 + 2\left\{\sum_{i=1}^{3}\left(\frac{A_i B_i}{k}\right)\right\}^2\right]}{\sqrt{\left\{\sum_{i=1}^{3}\left(A_i^2 - \frac{B_i^2}{k^2}\right)\right\}^2 + 4\left\{\sum_{i=1}^{3}\left(\frac{A_i B_i}{k}\right)\right\}^2}}
\end{aligned}
\tag{3.22}
$$

After substituting the desired apsis value $|\mathbf{e}_r(t_{aps})| = R_2$ into the left-hand side of Eq. (3.22), Eq. (3.22) is numerically solved to obtain k. Then, the mode frequency of the switched system can be determined by $\omega_\alpha = k\omega$. Finally, the Hamiltonian structure-preserving controller can be designed as follows,

$$
\begin{aligned}
\mathbf{T}_{c1} &= \mathbf{T}\mathbf{e}_r + \mathbf{K}\dot{\mathbf{e}}_r \\
&= (\mathbf{M}\mathbf{\Lambda}_\alpha\mathbf{M}^{-1} - \nabla_{\mathrm{rr}}^2 U(\mathbf{r}_r))\mathbf{e}_r - 2\Omega_f\mathbf{J}\dot{\mathbf{e}}_r \\
&= (-\omega_\alpha^2\mathbf{I}_3 - \nabla_{\mathrm{rr}}^2 U(\mathbf{r}_r))\mathbf{e}_r - 2\Omega_f\mathbf{J}\dot{\mathbf{e}}_r
\end{aligned}
\tag{3.23}
$$

3.2.3 Switching Point 2: From an Elliptical Orbit to a Circular Orbit

The second switching strategy is applied when the spacecraft traveling along the elliptical orbit approaches the other apsis. It is assumed that, after the second switching, the equation of motion is Eq. (3.10) with new mode frequency ω_β. Then, it can be designed such that the motion of the switched system is a circular orbit with radius R_2. At the switching point, the position and velocity vectors are perpendicular to each other. Therefore, the remaining condition for the switched system to achieve the circular motion is the magnitude of acceleration. Figure 3.2 shows the concept of the second switching. The magnitude of acceleration for the circular orbit is $|\ddot{\mathbf{e}}_r| = |\dot{\mathbf{e}}_r|^2/|\mathbf{e}_r|$. Using the equation of motion $\ddot{\mathbf{e}}_r = \mathbf{M}\mathbf{\Lambda}_\beta\mathbf{M}^{-1}\mathbf{e}_r = \mathbf{0}$ of the switched system, the following equation should hold for a circular motion.

$$|\mathbf{M}\mathbf{\Lambda}_\beta\mathbf{M}^{-1}\mathbf{e}_r| = \omega_\beta^2|\mathbf{e}_r| \equiv \frac{|\dot{\mathbf{e}}_r|^2}{|\mathbf{e}_r|} \tag{3.24}$$

Then, a new mode frequency ω_β is obtained as follows,

$$\omega_\beta = \pm\frac{|\dot{\mathbf{e}}_r|}{|\mathbf{e}_r|} \tag{3.25}$$

Finally, the Hamiltonian structure-preserving controller is designed as follows,

$$\begin{aligned}\mathbf{T}_{c2} &= \mathbf{T}\mathbf{e}_r + \mathbf{K}\dot{\mathbf{e}}_r \\ &= (\mathbf{M}\mathbf{\Lambda}_\beta\mathbf{M}^{-1} - \nabla_{\mathrm{rr}}^2 U(\mathbf{r}_r))\mathbf{e}_r - 2\Omega_f\mathbf{J}\dot{\mathbf{e}}_r \\ &= (-\omega_\beta^2\mathbf{I}_3 - \nabla_{\mathrm{rr}}^2 U(\mathbf{r}_r))\mathbf{e}_r - 2\Omega_f\mathbf{J}\dot{\mathbf{e}}_r\end{aligned} \tag{3.26}$$

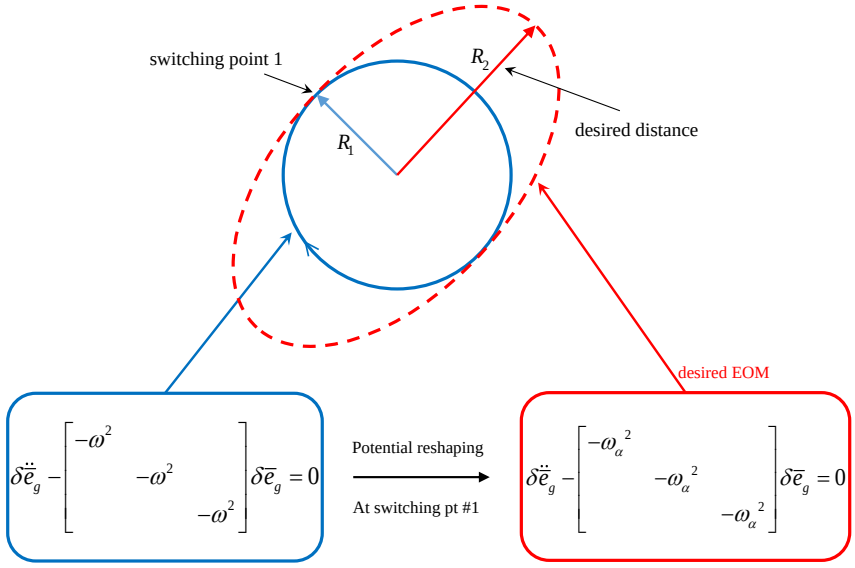

Figure 3.1 Switching point No.1

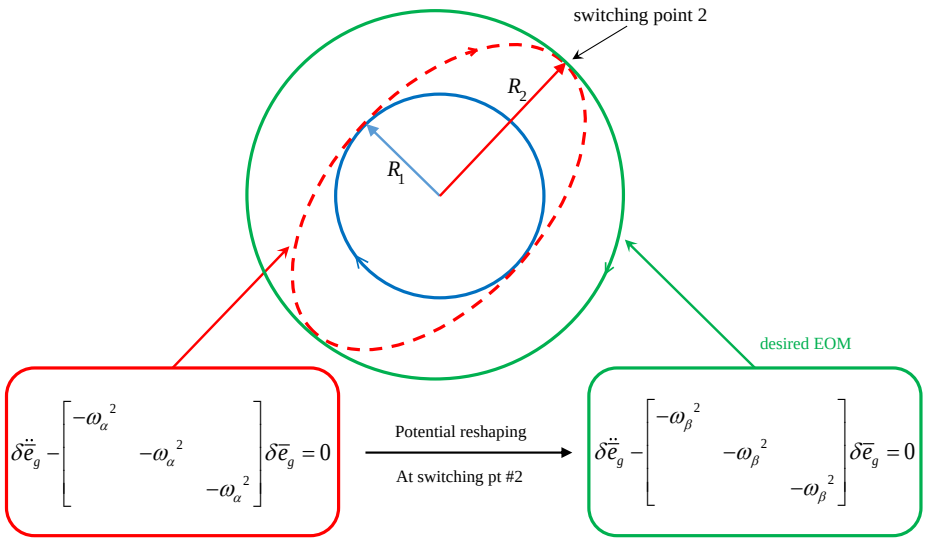

Figure 3.2 Switching point No.2

3.3 Hamiltonian Structure-Based Control

In general, a Hamiltonian function is interpreted as the total energy of autonomous systems. In this respect, the Hamiltonian structure-based control strategy can be thought as one of energy-based controls, and the aforementioned Hamiltonian structure-preserving control can be interpreted as a control scheme that appropriately shapes the potential energy of the system. According to [92], energy-based control has various advantages. The most salient feature is that the physical interpretation of the control input is clear, which makes it possible to handle the performance of the output as well as ensuring the stability.

In this subsection, a Hamiltonian structure-based controller is designed so that it can be applied to the unstable LPO tracking problem by extending previous works [24, 57]. A Hamiltonian structure-based control consists of two parts: i) potential shaping, and ii) energy dissipation. Potential shaping control is applied to reshape the gravitational potential around the equilibrium point to make the point an isolated minimum of the reshaped tracking error Hamiltonian function. Note that the potential shaping control is equivalent to the Hamiltonian structure-preserving control. After potential shaping, a damping term is added to make the motion converge to the minimum of the reshaped tracking error of the Hamiltonian function through energy dissipation.

3.3.1 Potential Shaping Control

As mentioned, the principle of the Hamiltonian structure-preserving control is to reshape the potential energy of the system, and therefore the Hamiltonian structure-preserving control can ultimately be regarded as a potential shaping control. It should be noted, however, that the Hamiltonian structure-preserving

control laws have been designed based only on the linearized equations of motion. It means that nonlinear stability of the closed-loop system is not guaranteed. Because the Hamiltonian structure-preserving controller changes the topology type of the equilibrium from hyperbolic to elliptic, the Hartman-Grobman theorem [93] cannot be applied, and therefore nonlinear stability of the closed-loop system is not guaranteed. In this section, Hamiltonian canonical coordinates are employed to investigate the stability of the Hamiltonian structure-preserving control. The nonlinear stability can be discussed by analyzing the system in the canonical coordinates space.

First, for autonomous Hamiltonian systems, the Lagrange-Dirichlet criterion can be applied to determine the stability of the equilibrium point of system.

Theorem 1 (Lagrange-Dirichlet)**.** If the second variation (Hessian) of the Hamiltonian, i.e., $\nabla^2\mathcal{H}(\mathbf{z})$ with $\mathbf{z} = (\mathbf{q}, \mathbf{p})$, is positive definite at the nondegenerate critical point $\mathbf{z}^*$, then the equilibrium point is stable [94, 95].

For a finite dimension system, the formal stability of the equilibrium point ensures the Lyapunov stability, that is, nonlinear stability [96]. Therefore, as along as the equilibrium of the autonomous Hamiltonian system satisfies the Lagrange-Dirichlet theorem, the stability of the equilibrium point is guaranteed in the sense of Lyapunov. However, in general, the equilibrium point is not an isolated minimum of the Hamiltonian, that is, an indefinite critical point. Accordingly, for the indefinite critical point, a control input should be applied to make the equilibrium be an isolated minimum of the Hamiltonian, which is called potential shaping. In the case of autonomous Hamiltonian system without gyroscopic forces, a potential shaping feedback control can be designed using a fixed gain so that the Hessian of a reshaped Hamiltonian is positive definite at

the equilibrium point [57, 97, 98].

On the other hand, in the case of an LPO tracking problem, that is, a nonautonomous Hamiltonian system with gyroscopic forces, a potential shaping feedback control should be designed using varying-gain so that the Hessian of the reshaped Hamiltonian tracking error, $\nabla^2\tilde{\mathcal{H}}_e$, after the potential shaping has a constant value. Furthermore, the artificial tracking error potential function, $\mathcal{S}_e$, which means a potential function used for potential shaping, should be zero at the equilibrium point to keep the equilibrium unchanged after the potential shaping, i.e., $\mathcal{S}_e(\mathbf{e}_q^*, \mathbf{q}_r) = 0$. Therefore, the potential shaping feedback controller for the LPO tracking can be designed as follows,

$$\mathbf{u}_r(\mathbf{e}_q, \mathbf{q}_r) = -\frac{\partial \mathcal{S}_e(\mathbf{e}_q, \mathbf{q}_r)}{\partial \mathbf{e}_q} \triangleq -\mathbf{W}(\mathbf{q}_r)\mathbf{e}_q \tag{3.27a}$$

$$\begin{aligned}\mathcal{S}_e(\mathbf{e}_q, \mathbf{q}_r) &= \frac{1}{2}\mathbf{e}_q^T\Big[k_p\mathbf{I}_3 - \nabla^2_{\mathrm{e_q e_q}} V_e(\mathbf{e}_q^*, \mathbf{q}_r)\Big]\mathbf{e}_q \\ &= \frac{1}{2}\mathbf{e}_q^T\Big[k_p\mathbf{I}_3 - \nabla^2_{\mathrm{qq}} V(\mathbf{q}_r)\Big]\mathbf{e}_q\end{aligned} \tag{3.27b}$$

$$V_e(\mathbf{e}_q, \mathbf{q}_r) = V(\mathbf{q}_r + \mathbf{e}_q) + V(\mathbf{q}_r) \tag{3.27c}$$

where the equilibrium $(\mathbf{e}_q^*, \mathbf{e}_p^*) = (\mathbf{0}\,, \mathbf{0})$, and design parameter $k_p > 0$.

As shown in Eq. (3.27b), varying artificial tracking error potential function is used for the potential shaping feedback control. Because the stability of the equilibrium point depends on the sign of the second variation (Hessian) of the reshaped tracking error Hamiltonian function, as long as the class of system is preserved in the Hamiltonian system, the artificial tracking error potential function with a higher order than the third-order does not influence the stability of the equilibrium point. Accordingly, the artificial tracking error potential function can be designed as a quadratic form, as shown in Eq. (3.27b). Therefore, the potential shaping feedback control has a simple linear control form

like Eq. (3.27a). As the value of k_p increases, the gravitational potential around the equilibrium point is more deformed. Hence, as the k_p increases, the location of the equilibrium point becomes robust to external disturbances and parameter uncertainties. Therefore, the larger the k_p, the larger the region where the equilibrium point is the isolated minimum value of the modified Hamiltonian tracking error. From the viewpoint of the Hamiltonian structure-preserving control, the value k_p is related to the period of the bounded motion. Indeed, a large value of k_p results in a bounded motion with a high frequency [85,99,100]. These physical interpretations of the potential shaping provide a guideline to adjust the value of k_p, and the switching Hamiltonian structure-preserving control strategy is a example of such guideline.

Lemma 1. : In the case of LPO tracking in CR3BP, if the second variation of the reshaped tracking error potential function with respect to $\mathbf{e}_q$ is positive definite at equilibrium $(\mathbf{e}_q^*, \mathbf{e}_p^*)$, i.e., $\mathbf{\Gamma} > 0$, except when $k_p = 1$, the Hessian of the reshaped tracking error Hamiltonian is positive definite, i.e., $\nabla^2 \tilde{\mathcal{H}}_e(\mathbf{e}_q^*, \mathbf{e}_p^*, \mathbf{q}_r, \mathbf{p}_r) > 0$.

Proof. After applying potential shaping, a reshaped tracking error Hamiltonian function can be written as follows,

$$\begin{aligned}\tilde{\mathcal{H}}_e(\mathbf{e}_q, \mathbf{e}_p, \mathbf{q}_r, \mathbf{p}_r) = &\frac{1}{2}\sum_{i=1}^{3}(p_{r,i} + e_{p,i})^2 + \frac{1}{2}\sum_{i=1}^{3} p_{r,i}^2 \\ &+ \Omega_f\big[(p_{r_1} + e_{p_1})(q_{r_2} + e_{q_2}) - (p_{r_2} + e_{p_2})(q_{r_1} + e_{q_1}) \\ &+ p_{r_1} q_{r_2} - p_{r_2} q_{r_1}\big] + \tilde{V}_e(\mathbf{e}_q, \mathbf{q}_r)\end{aligned} \tag{3.28}$$

where $\tilde{V}_e(\mathbf{e}_q, \mathbf{q}_r) = V_e(\mathbf{e}_q, \mathbf{q}_r) + \mathcal{S}_e(\mathbf{e}_q, \mathbf{q}_r)$, which denotes the reshaped tracking error potential function.

Now, the Hessian of the reshaped Hamiltonian tracking error at equilibrium $(\mathbf{e}_q^*, \mathbf{e}_p^*)$ can be written as follows,

$$\nabla^2 \tilde{\mathcal{H}}_e(\mathbf{e}_q^*, \mathbf{e}_p^*, \mathbf{q}_r, \mathbf{p}_r) = \begin{bmatrix} \mathbf{\Gamma} & -\Omega_f \mathbf{J} \\ \Omega_f \mathbf{J} & \mathbf{I}_3 \end{bmatrix} \tag{3.29}$$

where

$$\mathbf{\Gamma} = \begin{bmatrix} \frac{\partial^2 \tilde{V}_e(\mathbf{e}_q^*, \mathbf{q}_r)}{\partial e_{q_1}^2} & \frac{\partial^2 \tilde{V}_e(\mathbf{e}_q^*, \mathbf{q}_r)}{\partial e_{q_2} \partial e_{q_1}} & \frac{\partial^2 \tilde{V}_e(\mathbf{e}_q^*, \mathbf{q}_r)}{\partial e_{q_3} \partial e_{q_1}} \\ \frac{\partial^2 \tilde{V}_e(\mathbf{e}_q^*, \mathbf{q}_r)}{\partial e_{q_1} \partial e_{q_2}} & \frac{\partial^2 \tilde{V}_e(\mathbf{e}_q^*, \mathbf{q}_r)}{\partial e_{q_2}^2} & \frac{\partial^2 \tilde{V}_e(\mathbf{e}_q^*, \mathbf{q}_r)}{\partial e_{q_3} \partial e_{q_2}} \\ \frac{\partial^2 \tilde{V}_e(\mathbf{e}_q^*, \mathbf{q}_r)}{\partial e_{q_1} \partial e_{q_3}} & \frac{\partial^2 \tilde{V}_e(\mathbf{e}_q^*, \mathbf{q}_r)}{\partial e_{q_2} \partial e_{q_3}} & \frac{\partial^2 \tilde{V}_e(\mathbf{e}_q^*, \mathbf{q}_r)}{\partial e_{q_3}^2} \end{bmatrix} = k_p \mathbf{I}_3$$

Note that Eqs. (3.27b) and (3.27c) are used to obtain $\mathbf{\Gamma} = k_p \mathbf{I}_3$. If the leading principal minors of $\nabla^2 \tilde{\mathcal{H}}_e(\mathbf{e}_q^*, \mathbf{e}_p^*, \mathbf{q}_r, \mathbf{p}_r)$ are positive definite, $\nabla^2 \tilde{\mathcal{H}}_e(\mathbf{e}_q^*, \mathbf{e}_p^*, \mathbf{q}_r, \mathbf{p}_r)$ is guaranteed to be positive definite. That is, $\nabla^2 \tilde{\mathcal{H}}_e(\mathbf{e}_q^*, \mathbf{e}_p^*, \mathbf{q}_r, \mathbf{p}_r)$ is positive definite if and only if $\mathbf{\Gamma} > 0$ and $\det(\nabla^2 \tilde{\mathcal{H}}_e(\mathbf{e}_q^*, \mathbf{e}_p^*, \mathbf{q}_r, \mathbf{p}_r)) > 0$. Since $\mathbf{I}_3$ is invertible, the following relation is satisfied by the Schur complement.

$$\begin{aligned} \det(\nabla^2 \tilde{\mathcal{H}}_e(\mathbf{e}_q^*, \mathbf{e}_p^*, \mathbf{q}_r, \mathbf{p}_r)) &= \det(\mathbf{I}_3) \det(\mathbf{\Gamma} + \Omega_f^2 \mathbf{J} \mathbf{I}_3^{-1} \mathbf{J}) \\ &= k_p (k_p - \Omega_f^2)^2 \end{aligned} \tag{3.30}$$

If k_p is chosen as any positive value other than Ω_f^2, the Hessian of the reshaped tracking error potential function is positive definite. Therefore, the Hessian of the reshaped Hamiltonian tracking error is positive definite. In the CR3BP, the angular velocity of the frame is normalized to $\Omega_f = 1$, and therefore **Lemma 1** holds for any positive k_p except 1. □

Consequently, if the proposed potential shaping feedback control, Eq. (3.27), is applied to an unstable LPO, stability is guaranteed in the sense of Lyapunov when $k_p \neq 1$ in accordance with the Lagrange-Dirichlet theorem. In addition,

with the proposed potential shaping control, the vicinity of the equilibrium point becomes an autonomous Hamiltonian system, i.e., a conservative system, with a positive definite Hamiltonian function. That is, the Lyapunov stability is guaranteed because of the nature of energy conservation, but at the same time convergence to the equilibrium point is not possible. Therefore, for convergence to the equilibrium point, in other words, for exact LPO tracking, the conservative system structure formed around the equilibrium point should be broken. To this end, an additional control input should be designed to enable energy dissipation.

Remark 1. : Because the Lagrange-Dirichlet theorem is a sufficient condition to determine the stability, it cannot be concluded that the system is unstable even if the sufficient condition is not satisfied, that is, when k_p is 1.

Remark 2. : In this study, the potential shaping control is proposed as Eq. (3.27), but in practice it may be difficult to design the potential shaping control input using $\nabla^2_{\mathrm{qq}} V(\mathbf{q}_r)$ which constantly changes. That is, it is more feasible to design a potential shaping control input using a constant value of $\nabla^2_{\mathrm{qq}} V(\mathbf{q}^*_r)$ for a certain time interval of the reference orbit. Here, $\mathbf{q}^*_r$ denotes a representative point for each orbit piece during a certain time interval. However, in this case, $\nabla^2 \tilde{\mathcal{H}}_e(\mathbf{e}^*_q, \mathbf{e}^*_p, \mathbf{q}_r, \mathbf{p}_r)$ is not constant, and therefore the Lyapunov stability is not guaranteed by the Lagrange-Dirichlet theorem. Nonetheless, because the $\nabla^2_{\mathrm{qq}} V(\mathbf{q}_r)$ does not change rapidly in the target reference LPO, $\nabla^2 \tilde{\mathcal{H}}_e(\mathbf{e}^*_q, \mathbf{e}^*_p, \mathbf{q}_r, \mathbf{p}_r)$ can be considered to be nearly constant by designing sufficiently large k_p. In this case, it was shown by Scheeres et al. [24] that the orbital stability, i.e., Lagrange stability, was guaranteed.

Remark 3. : The mathematical definition of orbital stability is defined in [101].

However, it is not easy to determine whether or not the conditions for ensuring orbital stability are satisfied in general system. To address this problem, Scheeres et al. [24] applied the Floquet theory on the linearized system for the periodic reference orbit and determined the long-term stability, i.e., orbital stability, through the distribution of the eigenvalues of the monodromy matrix.

3.3.2 Energy Dissipation Control

By applying the proposed potential shaping control, the motion of the spacecraft is "trapped" around the equilibrium point. To make the "trapped" trajectory converge to the equilibrium point, it is required to break the Hamiltonian structure using dissipative forces.

Let us consider the following linear energy dissipation feedback controller.

$$\begin{aligned} \mathbf{u}_v(\dot{\mathbf{e}}_q) &= -k_d \mathbf{I}_3(\mathbf{e}_p + \Omega_f \mathbf{J}\mathbf{e}_q) \\ &= -k_d \mathbf{I}_3 \dot{\mathbf{e}}_q \\ &\triangleq -\mathbf{K}_d \dot{\mathbf{e}}_q \end{aligned} \tag{3.31}$$

where $k_d > 0$ is a damping parameter to be designed.

Theorem 2. If an initial value of the spacecraft is given in the vicinity of the equilibrium point $(\mathbf{e}_q^*, \mathbf{e}_p^*)$, the spacecraft converges to the equilibrium point by the proposed potential shaping control, Eq. (3.27), and energy dissipation control, Eq. (3.31).

Proof. After applying the potential shaping, the reshaped tracking error Hamiltonian function near the equilibrium point can be regarded as a locally Lyapunov function. To obtain a linearized tracking error Hamiltonian function, $\mathcal{H}_{e,2}$, near the equilibrium, the CR3BP equation, Eq. (2.5), should be linearized.

A linearized CR3BP equation with respect to the reference LPO before applying the potential shaping control can be written as

$$\frac{d}{dt}\begin{bmatrix}\mathbf{e}_q\\ \dot{\mathbf{e}}_q\end{bmatrix} = \begin{bmatrix}\mathbf{0}_3 & \mathbf{I}_3\\ \nabla^2_{\mathrm{qq}}U(\mathbf{q}_r) & 2\Omega_f\mathbf{J}\end{bmatrix}\begin{bmatrix}\mathbf{e}_q\\ \dot{\mathbf{e}}_q\end{bmatrix} \tag{3.32}$$

By applying the Legendre transformation using Eq. (2.10), we have

$$\frac{d}{dt}\begin{bmatrix}\mathbf{e}_q\\ \mathbf{e}_p\end{bmatrix} = \begin{bmatrix}\mathbf{I}_3 & \mathbf{0}_3\\ -\Omega_f\mathbf{J} & \mathbf{I}_3\end{bmatrix}\begin{bmatrix}\mathbf{0}_3 & \mathbf{I}_3\\ \nabla^2_{\mathrm{qq}}U(\mathbf{q}_r) & 2\Omega_f\mathbf{J}\end{bmatrix}\begin{bmatrix}\mathbf{I}_3 & \mathbf{0}_3\\ -\Omega_f\mathbf{J} & \mathbf{I}_3\end{bmatrix}^{-1}\begin{bmatrix}\mathbf{e}_q\\ \mathbf{e}_p\end{bmatrix} \tag{3.33}$$

By the Hamilton's equation, Eq. (2.8), the following equation can be obtained.

$$\begin{bmatrix}\frac{\partial\mathcal{H}_{e,2}(\mathbf{e}_q,\mathbf{e}_p,\mathbf{q}_r,\mathbf{p}_r)}{\partial\mathbf{e}_q}^T\\ \frac{\partial\mathcal{H}_{e,2}(\mathbf{e}_q,\mathbf{e}_p,\mathbf{q}_r,\mathbf{p}_r)}{\partial\mathbf{e}_p}^T\end{bmatrix} = \begin{bmatrix}\mathbf{0}_3 & -\mathbf{I}_3\\ \mathbf{I}_3 & \mathbf{0}_3\end{bmatrix}\begin{bmatrix}\mathbf{I}_3 & \mathbf{0}_3\\ -\Omega_f\mathbf{J} & \mathbf{I}_3\end{bmatrix}\begin{bmatrix}\mathbf{0}_3 & \mathbf{I}_3\\ \nabla^2_{\mathrm{qq}}U(\mathbf{q}_r) & 2\Omega_f\mathbf{J}\end{bmatrix}\begin{bmatrix}\mathbf{I}_3 & \mathbf{0}_3\\ -\Omega_f\mathbf{J} & \mathbf{I}_3\end{bmatrix}^{-1}\begin{bmatrix}\mathbf{e}_q\\ \mathbf{e}_p\end{bmatrix} \tag{3.34}$$

Therefore, the linearized error Hamiltonian function can be obtained as follows,

$$\begin{aligned}\mathcal{H}_{e,2}(\mathbf{e}_q,\mathbf{e}_p) &= \frac{1}{2}\begin{bmatrix}\mathbf{e}_q^T & \mathbf{e}_p^T\end{bmatrix}\begin{bmatrix}\mathbf{0}_3 & -\mathbf{I}_3\\ \mathbf{I}_3 & \mathbf{0}_3\end{bmatrix}\begin{bmatrix}\mathbf{I}_3 & \mathbf{0}_3\\ -\Omega_f\mathbf{J} & \mathbf{I}_3\end{bmatrix}\begin{bmatrix}\mathbf{0}_3 & \mathbf{I}_3\\ \nabla^2_{\mathrm{qq}}U(\mathbf{q}_r) & 2\Omega_f\mathbf{J}\end{bmatrix}\begin{bmatrix}\mathbf{I}_3 & \mathbf{0}_3\\ -\Omega_f\mathbf{J} & \mathbf{I}_3\end{bmatrix}^{-1}\begin{bmatrix}\mathbf{e}_q\\ \mathbf{e}_p\end{bmatrix}\\ &= \frac{1}{2}\begin{bmatrix}\mathbf{e}_q^T & \mathbf{e}_p^T\end{bmatrix}\begin{bmatrix}-\nabla^2_{\mathrm{qq}}U(\mathbf{q}_r)-\Omega_f^2\mathbf{J}\mathbf{J} & -\Omega_f\mathbf{J}\\ \Omega_f\mathbf{J} & \mathbf{I}_3\end{bmatrix}\begin{bmatrix}\mathbf{e}_q\\ \mathbf{e}_p\end{bmatrix}\end{aligned} \tag{3.35}$$

Note from Eq. (3.35) that $\mathcal{H}_{e,2}(\mathbf{e}_q,\mathbf{e}_p,\mathbf{q}_r,\mathbf{p}_r)$ before applying the potential shaping control cannot be a Lyapunov candidate function because it is not positive definite. However, after applying the proposed potential shaping control, it is guaranteed that $\tilde{\mathcal{H}}_{e,2}(\mathbf{e}_q,\mathbf{e}_p)$ is positive definite except for $k_p = 1$ by **Lemma 1**, and therefore the following $\tilde{\mathcal{H}}_{e,2}(\mathbf{e}_q,\mathbf{e}_p)$ can be a local Lyapunov candidate

function.

$$\tilde{\mathcal{H}}_{e,2}(\mathbf{e}_q, \mathbf{e}_p) = \frac{1}{2} \begin{bmatrix} \mathbf{e}_q^T & \mathbf{e}_p^T \end{bmatrix} \begin{bmatrix} \mathbf{\Gamma} & -\Omega_f \mathbf{J} \\ \Omega_f \mathbf{J} & \mathbf{I}_3 \end{bmatrix} \begin{bmatrix} \mathbf{e}_q \\ \mathbf{e}_p \end{bmatrix} \tag{3.36}$$

Now, after the potential shaping control, the linearized tracking error dynamics near the equilibrium point can be expressed using Eqs. (2.17) and (3.31) as

$$\dot{\mathbf{e}}_q^T = \frac{\partial \tilde{\mathcal{H}}_{e,2}(\mathbf{e}_q, \mathbf{e}_p)}{\partial \mathbf{e}_p} \tag{3.37a}$$

$$\begin{aligned} \dot{\mathbf{e}}_p^T &= -\frac{\partial \tilde{\mathcal{H}}_{e,2}(\mathbf{e}_q, \mathbf{e}_p)}{\partial \mathbf{e}_q} + \mathbf{u}_v^T \\ &= -\frac{\partial \tilde{\mathcal{H}}_{e,2}(\mathbf{e}_q, \mathbf{e}_p)}{\partial \mathbf{e}_q} - \dot{\mathbf{e}}_q^T \mathbf{K}_d \end{aligned} \tag{3.37b}$$

Using Eq. (3.37) and the Legendre transformation, the time derivative of $\tilde{\mathcal{H}}_{e,2}(\mathbf{e}_q, \mathbf{e}_p)$ along Eq. (3.37) can be written as follows,

$$\begin{aligned} \dot{\tilde{\mathcal{H}}}_{e,2} &= \frac{\partial \tilde{\mathcal{H}}_{e,2}(\mathbf{e}_q, \mathbf{e}_p)}{\partial \mathbf{e}_q} \frac{\partial \mathbf{e}_q}{\partial t} + \frac{\partial \tilde{\mathcal{H}}_{e,2}(\mathbf{e}_q, \mathbf{e}_p)}{\partial \mathbf{e}_p} \frac{\partial \mathbf{e}_p}{\partial t} \\ &= \frac{\partial \tilde{\mathcal{H}}_{e,2}(\mathbf{e}_q, \mathbf{e}_p)}{\partial \mathbf{e}_q} \frac{\partial \tilde{\mathcal{H}}_{e,2}(\mathbf{e}_q, \mathbf{e}_p)}{\partial \mathbf{e}_p} - \frac{\partial \tilde{\mathcal{H}}_{e,2}(\mathbf{e}_q, \mathbf{e}_p)}{\partial \mathbf{e}_p} \frac{\partial \tilde{\mathcal{H}}_{e,2}(\mathbf{e}_q, \mathbf{e}_p)}{\partial \mathbf{e}_q} - \frac{\partial \tilde{\mathcal{H}}_{e,2}(\mathbf{e}_q, \mathbf{e}_p)}{\partial \mathbf{e}_p} \mathbf{K}_d \dot{\mathbf{e}}_q \\ &= -k_d \|\dot{\mathbf{e}}_q\|^2 \\ &\leq 0 \end{aligned} \tag{3.38}$$

Therefore, a set $\boldsymbol{E} = \{\dot{\mathbf{e}}_q | \dot{\tilde{\mathcal{H}}}_{e,2}(\dot{\mathbf{e}}_q) = 0\} = \{\dot{\mathbf{e}}_q = \mathbf{0}\}$. Meanwhile, $\partial \tilde{\mathcal{H}}_{e,2} / \partial \mathbf{e}_p$ and $\partial \tilde{\mathcal{H}}_{e,2} / \partial \mathbf{e}_q$ satisfy the following relations.

$$\frac{\partial \tilde{\mathcal{H}}_{e,2}(\mathbf{e}_q, \mathbf{e}_p)}{\partial \mathbf{e}_p} = \mathbf{e}_p^T - \Omega_f \mathbf{e}_q^T \mathbf{J} \tag{3.39a}$$

$$\frac{\partial \tilde{\mathcal{H}}_{e,2}(\mathbf{e}_q, \mathbf{e}_p)}{\partial \mathbf{e}_q} = \mathbf{e}_q^T \Gamma + \Omega_f \mathbf{e}_p^T \mathbf{J} \tag{3.39b}$$

Then, the largest invariant set in $\boldsymbol{E}$ is $\boldsymbol{M} = \{(\dot{\mathbf{e}}_q, \dot{\mathbf{e}}_p) = (\mathbf{0}, \mathbf{0})\}$, and therefore the equilibrium point $(\mathbf{e}_q^*, \mathbf{e}_p^*) = (\mathbf{0}, \mathbf{0})$ is locally asymptotically stable by

LaSalle's invariance principle. □

In summary, for a non-autonomous Hamiltonian system, applying the proposed potential shaping control and energy dissipation control can achieve exact target LPO tracking. Note that this result is in line with that of van der Schaft [57] in an autonomous Hamiltonian system and shares the same philosophy as interconnection and damping assignment passivity-based control (IDA-PBC) [92,102]. Furthermore, because the proposed Hamiltonian structure-based control has a proportional-derivative control form, it can be easily implemented in real systems. However, the orbital tracking performance is only valid when the system has the exact form of the Hamiltonian system. In other words, if the Hamiltonian system structure is not maintained due to disturbances, the tracking performance may be degraded. This lack of robustness is a weakness of the station-keeping strategy using the geometric structure of phase space [20], and therefore a combination with a robust control scheme is required for performance enhancement.

Chapter 4

Filtered Extended High-Gain Observer and Closed-Loop Stability

The environment of deep-space is highly uncertain, and therefore a dynamic system cannot be represented as an exact Hamiltonian system. A real system is a "perturbed" Hamiltonian system due to the unmodeled dynamics, external disturbances, and parameter uncertainties. In spite of the well-known stability robustness of the energy-based control for the parameter uncertainty, the robustness with respect to the external disturbances such as measurement and/or process noise, is not ensured. Also, even though the stability of the system is guaranteed, the reference orbit tracking performance may not be satisfactory due to excessive external disturbances. To address this problem, a number of energy-based control techniques that are robust to the disturbances and uncertainties have been studied [103–105]. However, all of the previous studies were only applicable when certain types of disturbances were assumed, which is difficult to satisfy in real deep-space environments. Moreover, full-state information, including the position and velocity, are required.

In this chapter, to address these issues, the Extended High-Gain Observer (EHGO) technique is employed [58]. To attenuate the effects of the measurement noise amplification of the standard EHGO, an enhanced version of the EHGO

using integral state feedback, is proposed, which is Filtered Extended High-Gain Observer (FEHGO). And, the convergence of the proposed filter is proven. The closed-loop stability analysis for the entire system applying the FEHGO-based Hamiltonian structure-based controller is also performed.

4.1 Filtered Extended High-Gain Observer and Its Convergence

The spacecraft dynamics can be written as follows,

$$\dot{\boldsymbol{X}} = \boldsymbol{f}(\boldsymbol{X}) + \mathbf{B}\mathbf{u} + \mathbf{E}\mathbf{d} \tag{4.1}$$

where the system state is $\boldsymbol{X} = [\mathbf{r}, \mathbf{v}]^T \in \mathbb{R}^{6\times1}$, control input is $\mathbf{u} = [u_x, u_y, u_z]^T \in \mathbb{R}^{3\times1}$, and external disturbance is $\mathbf{d} = [d_x, d_y, d_z]^T \in \mathbb{R}^{3\times1}$, $\boldsymbol{f}(\boldsymbol{X}) \in \mathbb{R}^{6\times1}$ denotes the dynamics of the spacecraft, $\mathbf{B} = \mathbf{B}_n + \Delta\mathbf{B} \in \mathbb{R}^{6\times3}$, $\mathbf{B}_n = [\mathbf{0}_3 \quad \mathbf{I}_3]^T$, $\Delta\mathbf{B}$ is its associated uncertainties, and $\mathbf{E} = [\mathbf{0}_3 \quad \mathbf{I}_3]^T \in \mathbb{R}^{6\times3}$.

By defining lumped disturbance as $\mathbf{d}^* \triangleq \boldsymbol{f}(\boldsymbol{X}) - \boldsymbol{f}_n(\boldsymbol{X}) + \Delta\mathbf{B}\mathbf{u} + \mathbf{E}\mathbf{d}$ with the nominal dynamics $\boldsymbol{f}_n(\boldsymbol{X})$ of the spacecraft in CR3BP, Eq. (4.1) can be rewritten as

$$\dot{\boldsymbol{X}} = \boldsymbol{f}_n(\boldsymbol{X}) + \mathbf{B}_n\mathbf{u} + \mathbf{E}\mathbf{d}^* \tag{4.2}$$

The standard EHGO treats the lumped disturbance $\mathbf{d}^*$ as an augmented state of the system. In this study, the proposed FEHGO treats the integral term of the position vector with measurement noise as a following additional state $\mathbf{x}_0 \in \mathbb{R}^{3\times1}$.

$$\mathbf{x}_0(t) \triangleq \int_0^t (\mathbf{r} + \boldsymbol{\nu}) d\tau \tag{4.3}$$

where $\boldsymbol{\nu} = [\nu_x, \nu_y, \nu_z]^T \in \mathbb{R}^{3\times1}$ denotes position measurement noise, i.e., navigation error.

By defining extended states $[\mathbf{x}_0, \mathbf{r}, \mathbf{v}, \mathbf{d}^*]^T \in \mathbb{R}^{12\times1}$, the extended state sys-

tem equation can be written as follows,

$$\frac{d}{dt}\begin{bmatrix}\mathbf{x}_0\\ \mathbf{r}\\ \mathbf{v}\\ \mathbf{d}^*\end{bmatrix} = \begin{bmatrix}\mathbf{0}_3 & \mathbf{I}_3 & \mathbf{0}_3 & \mathbf{0}_3\\ \mathbf{0}_3 & \mathbf{0}_3 & \mathbf{I}_3 & \mathbf{0}_3\\ \mathbf{0}_3 & \mathbf{0}_3 & \mathbf{0}_3 & \mathbf{I}_3\\ \mathbf{0}_3 & \mathbf{0}_3 & \mathbf{0}_3 & \mathbf{0}_3\end{bmatrix}\begin{bmatrix}\mathbf{x}_0\\ \mathbf{r}\\ \mathbf{v}\\ \mathbf{d}^*\end{bmatrix} + \begin{bmatrix}\mathbf{0}_{3\times1}\\ \mathbf{0}_{3\times1}\\ \boldsymbol{f}_{\text{cr3bp}}(\boldsymbol{X})\\ \mathbf{0}_{3\times1}\end{bmatrix} + \begin{bmatrix}\mathbf{0}_{3\times1}\\ \mathbf{0}_{3\times1}\\ \mathbf{0}_{3\times1}\\ \mathbf{h}\end{bmatrix} + \begin{bmatrix}\mathbf{0}_{3\times1}\\ \mathbf{0}_{3\times1}\\ \mathbf{u}(\hat{\boldsymbol{X}},\hat{\mathbf{d}}^*)\\ \mathbf{0}_{3\times1}\end{bmatrix} + \begin{bmatrix}\nu\\ \mathbf{0}_{3\times1}\\ \mathbf{0}_{3\times1}\\ \mathbf{0}_{3\times1}\end{bmatrix} \tag{4.4}$$

where $\boldsymbol{f}_{\text{cr3bp}} \in \mathbb{R}^{3\times1}$ denotes the nonlinear CR3BP equations of motion, Eq. (2.5), and $\mathbf{h} \in \mathbb{R}^{3\times1}$ denotes the rate of the lumped disturbance, i.e., $\mathbf{h} = \dot{\mathbf{d}}^*$, which is assumed to be an unknown function but bounded.

Then, the FEHGO can be designed as follows,

$$\frac{d}{dt}\begin{bmatrix}\hat{\mathbf{x}}_0\\ \hat{\mathbf{r}}\\ \hat{\mathbf{v}}\\ \hat{\mathbf{d}}^*\end{bmatrix} = \begin{bmatrix}\mathbf{0}_3 & \mathbf{I}_3 & \mathbf{0}_3 & \mathbf{0}_3\\ \mathbf{0}_3 & \mathbf{0}_3 & \mathbf{I}_3 & \mathbf{0}_3\\ \mathbf{0}_3 & \mathbf{0}_3 & \mathbf{0}_3 & \mathbf{I}_3\\ \mathbf{0}_3 & \mathbf{0}_3 & \mathbf{0}_3 & \mathbf{0}_3\end{bmatrix}\begin{bmatrix}\hat{\mathbf{x}}_0\\ \hat{\mathbf{r}}\\ \hat{\mathbf{v}}\\ \hat{\mathbf{d}}^*\end{bmatrix} + \begin{bmatrix}\mathbf{0}_{3\times1}\\ \mathbf{0}_{3\times1}\\ \boldsymbol{f}_{\text{cr3bp}}(\hat{\boldsymbol{X}})\\ \mathbf{0}_{3\times1}\end{bmatrix} + \begin{bmatrix}\mathbf{0}_{3\times1}\\ \mathbf{0}_{3\times1}\\ \mathbf{u}(\hat{\boldsymbol{X}},\hat{\mathbf{d}}^*)\\ \mathbf{0}_{3\times1}\end{bmatrix} + \begin{bmatrix}\mathbf{L}_0\\ \mathbf{L}_1\\ \mathbf{L}_2\\ \mathbf{L}_3\end{bmatrix}(\mathbf{x}_0 - \hat{\mathbf{x}}_0) \tag{4.5}$$

where $\mathbf{L}_i \in \mathbb{R}^{3\times3}, i = 0, \cdots, 3$, are observer gain matrices, which are designed according to the following high-gain observer gain assign rule [59].

$$\mathbf{L}_0 = \frac{1}{\varepsilon}\text{diag}(l_{01}, l_{02}, l_{03}) \tag{4.6a}$$

$$\mathbf{L}_1 = \frac{1}{\varepsilon^2}\text{diag}(l_{11}, l_{12}, l_{13}) \tag{4.6b}$$

$$\mathbf{L}_2 = \frac{1}{\varepsilon^3}\text{diag}(l_{21}, l_{22}, l_{23}) \tag{4.6c}$$

$$\mathbf{L}_3 = \frac{1}{\varepsilon^4}\text{diag}(l_{31}, l_{32}, l_{33}) \tag{4.6d}$$

The elements of the observer gain matrices, $l_{ij} > 0, i = 0, \cdots, 3, j = 1, \cdots, 3$, are parameters to make the system matrix of the estimation error dynamics be Hurwitz, and $\varepsilon \ll 1$ is a positive constant.

For a convergence analysis of the proposed FEHGO, let us define the fol-

lowing coordinates transformation.

$$\boldsymbol{\eta}_0 = \frac{\mathbf{x}_0 - \hat{\mathbf{x}}_0}{\varepsilon^3}, \quad \boldsymbol{\eta}_1 = \frac{\mathbf{r} - \hat{\mathbf{r}}}{\varepsilon^2}, \quad \boldsymbol{\eta}_2 = \frac{\mathbf{v} - \hat{\mathbf{v}}}{\varepsilon}, \quad \boldsymbol{\eta}_3 = \mathbf{d}^* - \hat{\mathbf{d}}^* \tag{4.7}$$

Then, the estimation error dynamics of the FEHGO in new coordinates can be written as

$$\dot{\boldsymbol{\eta}} = \frac{1}{\varepsilon}\boldsymbol{A}\boldsymbol{\eta} + \frac{1}{\varepsilon}\boldsymbol{f}_{nm} + \boldsymbol{f}_h + \frac{1}{\varepsilon^3}\boldsymbol{f}_{ns} \tag{4.8}$$

where $\boldsymbol{\eta}^T = [\boldsymbol{\eta}_0, \boldsymbol{\eta}_1, \boldsymbol{\eta}_2, \boldsymbol{\eta}_3]$, and

$$\boldsymbol{A} = \begin{bmatrix} -\varepsilon\mathbf{L}_0 & \mathbf{I}_3 & \mathbf{0}_3 & \mathbf{0}_3 \\ -\varepsilon^2\mathbf{L}_1 & \mathbf{0}_3 & \mathbf{I}_3 & \mathbf{0}_3 \\ -\varepsilon^3\mathbf{L}_2 & \mathbf{0}_3 & \mathbf{0}_3 & \mathbf{I}_3 \\ -\varepsilon^4\mathbf{L}_3 & \mathbf{0}_3 & \mathbf{0}_3 & \mathbf{0}_3 \end{bmatrix}, \boldsymbol{f}_{nm} = \begin{bmatrix} \mathbf{0}_{3\times1} \\ \mathbf{0}_{3\times1} \\ \boldsymbol{f}_{\text{cr3bp}}(\boldsymbol{X}) - \boldsymbol{f}_{\text{cr3bp}}(\hat{\boldsymbol{X}}) \\ \mathbf{0}_{3\times1} \end{bmatrix}, \boldsymbol{f}_h = \begin{bmatrix} \mathbf{0}_{3\times1} \\ \mathbf{0}_{3\times1} \\ \mathbf{0}_{3\times1} \\ \mathbf{h} \end{bmatrix}, \boldsymbol{f}_{ns} = \begin{bmatrix} \nu \\ \mathbf{0}_{3\times1} \\ \mathbf{0}_{3\times1} \\ \mathbf{0}_{3\times1} \end{bmatrix} \tag{4.9}$$

For comparison, let us consider the estimation error dynamics of the standard EHGO with position measurement noise.

$$\begin{aligned} \frac{d}{dt}\begin{bmatrix} \boldsymbol{\eta}_1 \\ \boldsymbol{\eta}_2 \\ \boldsymbol{\eta}_3 \end{bmatrix} =& \frac{1}{\varepsilon}\begin{bmatrix} -\varepsilon\mathbf{L}_1' & \mathbf{I}_3 & \mathbf{0}_3 \\ -\varepsilon^2\mathbf{L}_2' & \mathbf{0}_3 & \mathbf{I}_3 \\ -\varepsilon^3\mathbf{L}_3' & \mathbf{0}_3 & \mathbf{0}_3 \end{bmatrix}\begin{bmatrix} \boldsymbol{\eta}_1 \\ \boldsymbol{\eta}_2 \\ \boldsymbol{\eta}_3 \end{bmatrix} + \frac{1}{\varepsilon}\begin{bmatrix} \mathbf{0}_{3\times1} \\ \boldsymbol{f}_{\text{cr3bp}}(\boldsymbol{X}) - \boldsymbol{f}_{\text{cr3bp}}(\hat{\boldsymbol{X}}) \\ \mathbf{0}_{3\times1} \end{bmatrix} + \begin{bmatrix} \mathbf{0}_{3\times1} \\ \mathbf{0}_{3\times1} \\ \mathbf{h} \end{bmatrix} \\ & - \frac{1}{\varepsilon^3}\begin{bmatrix} \varepsilon\mathbf{L}_1' \\ \varepsilon^2\mathbf{L}_2' \\ \varepsilon^3\mathbf{L}_3' \end{bmatrix}\nu \end{aligned} \tag{4.10}$$

Note that $\mathbf{L}_i'$ $(i = 1, 2, 3)$ is the EHGO gain that makes the poles of the EHGO estimation error dynamics and poles of the FEHGO estimation error dynamics identical. Equations (4.8) and (4.10) show that the estimation error dynamics

of the FEHGO are less affected by noise amplification due to the high gain of the observer. Therefore, it can be expected that the estimation performance of FEHGO is better than that of standard EHGO. Because $\boldsymbol{A}/\varepsilon$ is Hurwitz for all ε, given any positive constant $\alpha > 0$, there exists a positive definite matrix $\boldsymbol{P} = \boldsymbol{P}^T \in \mathbb{R}^{12\times 12}$ satisfying the following Lyapunov equation.

$$\boldsymbol{A}^T\boldsymbol{P} + \boldsymbol{P}\boldsymbol{A} = -\alpha \mathbf{I}_{12} \tag{4.11}$$

Now, let us consider a following Lyapunov candidate function for Eq. (4.8).

$$V_1 = \boldsymbol{\eta}^T\boldsymbol{P}\boldsymbol{\eta} \tag{4.12}$$

The nominal CR3BP nonlinear dynamics $\boldsymbol{f}_{\text{cr3bp}}$ can be regarded as a Lipschitz function because there is a lower bound of $r_i, i = 1, 2$, with the Earth's radius R_E and the Moon's radius R_M, respectively, and $\boldsymbol{f}_{\text{cr3bp}}$ converges to 0 as r_i increases. Therefore, the following relation is satisfied with the Lipschitz constant κ.

$$\begin{aligned} \|\boldsymbol{f}_{nm}\| &= \|\boldsymbol{f}_{\text{cr3bp}}(\boldsymbol{X}) - \boldsymbol{f}_{\text{cr3bp}}(\hat{\boldsymbol{X}})\| \\ &\leq \kappa\|\boldsymbol{X} - \hat{\boldsymbol{X}}\| \\ &= \kappa\varepsilon\sqrt{\varepsilon^2\eta_1^2 + \eta_2^2} \end{aligned} \tag{4.13}$$

Additionally, the following relations hold.

$$\frac{V_1}{\lambda_{\max}(\boldsymbol{P})} \leq \|\boldsymbol{\eta}\|^2 \leq \frac{V_1}{\lambda_{\min}(\boldsymbol{P})} \tag{4.14a}$$

$$\|\boldsymbol{\eta}^T\boldsymbol{P}\| \leq \lambda_{\max}(\boldsymbol{P})\|\boldsymbol{\eta}\| \tag{4.14b}$$

Using Eqs. (4.13) and (4.14), the time derivative of V_1 along Eq. (4.8) can be

written as follows,

$$\begin{aligned}
\dot{V}_1 &= \dot{\boldsymbol{\eta}}^T \boldsymbol{P}\boldsymbol{\eta} + \boldsymbol{\eta}^T \boldsymbol{P}\dot{\boldsymbol{\eta}} \\
&= -\frac{\alpha}{\varepsilon}\boldsymbol{\eta}^T\boldsymbol{\eta} + 2\boldsymbol{\eta}^T\boldsymbol{P}\Big(\boldsymbol{f}_h + \frac{1}{\varepsilon}\boldsymbol{f}_{nm} + \frac{1}{\varepsilon^3}\boldsymbol{f}_{ns}\Big) \\
&\le -\frac{\alpha}{\varepsilon}\|\boldsymbol{\eta}\|^2 + 2\lambda_{\max}(\boldsymbol{P})\|\boldsymbol{\eta}\|\Big\{\|\boldsymbol{f}_h\| + \frac{1}{\varepsilon}\|\boldsymbol{f}_{nm}\| + \frac{1}{\varepsilon^3}\|\boldsymbol{f}_{ns}\|\Big\} \\
&\le -\frac{\alpha}{\varepsilon}\|\boldsymbol{\eta}\|^2 + 2\lambda_{\max}(\boldsymbol{P})\|\boldsymbol{\eta}\|\Big\{\gamma_h + \kappa\sqrt{\varepsilon^2\eta_1^2 + \eta_2^2} + \frac{1}{\varepsilon^3}\gamma_{ns}\Big\} \\
&\le -\frac{\alpha}{\varepsilon}\|\boldsymbol{\eta}\|^2 + 2\lambda_{\max}(\boldsymbol{P})\|\boldsymbol{\eta}\|\Big\{\gamma_h + \kappa\|\boldsymbol{\eta}\| + \frac{1}{\varepsilon^3}\gamma_{ns}\Big\} \\
&\le -\frac{\alpha}{\varepsilon}\frac{V_1}{\lambda_{\max}(\boldsymbol{P})} + 2\lambda_{\max}(\boldsymbol{P})\sqrt{\frac{V_1}{\lambda_{\min}(\boldsymbol{P})}}\left\{\gamma_h + \kappa\sqrt{\frac{V_1}{\lambda_{\min}(\boldsymbol{P})}} + \frac{1}{\varepsilon^3}\gamma_{ns}\right\}
\end{aligned} \tag{4.15}$$

Note that the rate of lumped disturbance and the magnitude of noise are assumed to be bounded, i.e., $\|\boldsymbol{f}_h\| \le \gamma_h$ and $\|\boldsymbol{f}_{ns}\| \le \gamma_{ns}$. In addition, using $\dot{V}_1 = 2\sqrt{V_1}\big(d\sqrt{V_1}/dt\big)$, the following relation can be obtained.

$$\frac{d\sqrt{V_1}}{dt} \le c_0\sqrt{V_1} + \left(\gamma_h + \frac{\gamma_{ns}}{\varepsilon^3}\right)\frac{\lambda_{\max}(\boldsymbol{P})}{\sqrt{\lambda_{\min}(\boldsymbol{P})}} \tag{4.16}$$

where $c_0 = -\alpha/2\varepsilon\lambda_{\max}(\boldsymbol{P}) + \kappa\lambda_{\max}(\boldsymbol{P})/\lambda_{\min}(\boldsymbol{P})$.

Equation (4.16) is a differential inequality, and therefore the bound of the solution $\sqrt{V_1(t)}$ can be obtained by applying the comparison lemma [106] as

$$\sqrt{V_1(t)} \le \left[\sqrt{V_1(0)} + \frac{(\gamma_h + \frac{\gamma_{ns}}{\varepsilon^3})\lambda_{\max}(\boldsymbol{P})}{c_0\sqrt{\lambda_{\min}(\boldsymbol{P})}}\right]e^{c_0 t} - \frac{(\gamma_h + \frac{\gamma_{ns}}{\varepsilon^3})\lambda_{\max}(\boldsymbol{P})}{c_0\sqrt{\lambda_{\min}(\boldsymbol{P})}} \tag{4.17}$$

By substituting Eq. (4.17) into Eq. (4.14a), the estimation error bound of the FEHGO can be obtained as

$$\begin{aligned}
\|\boldsymbol{\eta}(t)\| &\le \frac{\sqrt{V_1(t)}}{\sqrt{\lambda_{\min}(\boldsymbol{P})}} \\
&\le \left[\frac{\sqrt{V_1(0)}}{\sqrt{\lambda_{\min}(\boldsymbol{P})}} + \frac{(\gamma_h + \frac{\gamma_{ns}}{\varepsilon^3})\lambda_{\max}(\boldsymbol{P})}{c_0\lambda_{\min}(\boldsymbol{P})}\right]e^{c_0 t} - \frac{(\gamma_h + \frac{\gamma_{ns}}{\varepsilon^3})\lambda_{\max}(\boldsymbol{P})}{c_0\lambda_{\min}(\boldsymbol{P})}
\end{aligned} \tag{4.18}$$

The parameter c_0 can be made negative by adjusting ε for a given α, and therefore the following relation holds for negative α.

$$\limsup_{t\to\infty}\|\boldsymbol{\eta}(t)\| \le \beta = \frac{2\varepsilon\lambda_{\max}^2(\boldsymbol{P})(\gamma_h + \frac{\gamma_{ns}}{\varepsilon^3})}{\alpha\lambda_{\min}(\boldsymbol{P}) - 2\varepsilon\kappa\lambda_{\max}^2(\boldsymbol{P})} \tag{4.19}$$

Therefore, from Eqs. (4.7) and (4.8), it can be stated that all of the states of the FEHGO converge as

$$\begin{aligned}
&\limsup_{t\to\infty}\|\mathbf{x}_0(t) - \hat{\mathbf{x}}_0(t)\| \le \varepsilon^3\beta \\
&\limsup_{t\to\infty}\|\mathbf{r}(t) - \hat{\mathbf{r}}(t)\| \le \varepsilon^2\beta \\
&\limsup_{t\to\infty}\|\mathbf{v}(t) - \hat{\mathbf{v}}(t)\| \le \varepsilon\beta \\
&\limsup_{t\to\infty}\|\mathbf{d}^*(t) - \hat{\mathbf{d}}^*(t)\| \le \beta
\end{aligned} \tag{4.20}$$

From Eqs. (4.19) and (4.20), as the value of ε decreases, the estimation error bound of $\mathbf{x}_0$ converges to 0 and the error bound of $\mathbf{r}$ converges to a specific value, $2\gamma_{ns}\lambda_{\max}^2((P))/\alpha\lambda_{\min}(\boldsymbol{P})$. However, since the error bounds of $\mathbf{v}$ and $\mathbf{d}^*$ diverge, the value of ε cannot be reduced indefinitely. Note that the convergence proof of the FEHGO does not apply any linearization assumption, and therefore convergence is guaranteed in the whole region regardless of the initial value of the observer. Therefore, the above convergence proof is more general than that of the extended state observer (ESO) proposed by Narula and Biggs [30], where the convergence is guaranteed only around LPO under the assumption that navigation error does not exist.

4.2 Closed-Loop Stability Analysis

In this section, closed-loop stability analysis for the entire system applying the FEHGO-based Hamiltonian structure-based controller is performed. The

FEHGO-based Hamiltonian structure-based controller consists of three parts: i) potential shaping $\mathbf{u}_r$, ii) energy dissipation $\mathbf{u}_v$, and iii) disturbance rejection $\mathbf{u}_d$. Each part of the control input is designed using the state values estimated by FEHGO. The control input for LPO tracking can be written from Eqs. (3.27) and (3.31) as follows,

$$\begin{aligned}\mathbf{u} &= \mathbf{u}_r + \mathbf{u}_v + \mathbf{u}_d \\ &= -\mathbf{W}(\mathbf{r}_r)\hat{\mathbf{e}}_r - \mathbf{K}_d\hat{\mathbf{e}}_v - \hat{\mathbf{d}}^*\end{aligned} \tag{4.21}$$

where $\hat{\mathbf{e}}_r = \hat{\mathbf{r}} - \mathbf{r}_r \in \mathbb{R}^{3\times1}$, $\hat{\mathbf{e}}_v = \hat{\mathbf{v}} - \mathbf{v}_r \in \mathbb{R}^{3\times1}$, and $(\mathbf{r}_r, \mathbf{v}_r)$ denote the position and velocity vector of the target LPO, respectively.

In this study, the time-varying potential shaping gain matrix $\mathbf{W}(\mathbf{r}_r)$, Eq. (3.27a), is chosen as follows,

$$\mathbf{W}(\mathbf{r}_r) = k_p\mathbf{I}_3 - \nabla^2_{\mathrm{rr}}V(\mathbf{r}_r) \tag{4.22}$$

Now, from Eqs. (4.4), (4.7), and (4.21), the closed-loop tracking error dynamics can be obtained as

$$\dot{\mathbf{e}}_r = \mathbf{e}_v \tag{4.23a}$$

$$\begin{aligned}\dot{\mathbf{e}}_v &= (\mathbf{d}^* + \boldsymbol{f}_{\mathrm{cr3bp}}(\boldsymbol{X}) - \mathbf{W}(\mathbf{r}_r)\hat{\mathbf{e}}_r - \mathbf{K}_d\hat{\mathbf{e}}_v - \hat{\mathbf{d}}^*) - \boldsymbol{f}_{\mathrm{cr3bp}}(\boldsymbol{X}_r) \\ &= \boldsymbol{f}_{\mathrm{cr3bp}}(\boldsymbol{X}) - \boldsymbol{f}_{\mathrm{cr3bp}}(\boldsymbol{X}_r) - \mathbf{W}(\mathbf{r}_r)\mathbf{e}_r - k_d\mathbf{e}_v + \mathbf{W}(\mathbf{r}_r)\varepsilon^2\boldsymbol{\eta}_1 + k_d\varepsilon\boldsymbol{\eta}_2 + \boldsymbol{\eta}_3\end{aligned} \tag{4.23b}$$

For the entire closed-loop system stability analysis, let us consider the following time-varying Lyapunov candidate function, which is similar to that of the time-invariant case [107].

$$V_2(\mathbf{r}_r) = \frac{1}{2}\left[\mathbf{e}_r^T\{\mathbf{W}(\mathbf{r}_r) + \zeta\mathbf{K}_d\}\mathbf{e}_r + 2\zeta\mathbf{e}_r^T\mathbf{e}_v + \mathbf{e}_v^T\mathbf{e}_v\right] \tag{4.24}$$

where ζ is a positive constant.

Lemma 2. : The Lyapunov candidate function, Eq. (4.24), is positive definite if ζ satisfies the following condition.

$$\begin{cases} \max\left\{ -\frac{\min(\Lambda_{\mathbf{W}}^{-})}{k_d}, \frac{k_d - \sqrt{k_d^2 + 4\min(\Lambda_{\mathbf{W}}^{-})}}{2} \right\} < \zeta < \frac{k_d + \sqrt{k_d^2 + 4\min(\Lambda_{\mathbf{W}}^{-})}}{2}, & \text{if} \quad -\frac{k_d^2}{4} < \min(\Lambda_{\mathbf{W}}^{-}) < 0 \\ 0 < \zeta < \frac{k_d + \sqrt{k_d^2 + 4\min(\Lambda_{\mathbf{W}}^{-})}}{2} & \text{if} \quad 0 \leq \min(\Lambda_{\mathbf{W}}^{-}) \end{cases} \tag{4.25}$$

where $\Lambda_{\mathbf{W}}^{-}$ and $\Lambda_{\mathbf{W}}^{+}$ denote a set of the minimum/maximum eigenvalue of the time-varying potential shaping gain matrix during one period of the reference LPO, respectively.

Proof. Since the potential shaping gain matrix $\mathbf{W}(\mathbf{r}_r)$ is a symmetric matrix, it can always be diagonalized, and therefore the Lyapunov candidate function $V_2(\mathbf{r}_r)$ satisfies the following relation.

$$\frac{1}{2}\mathbf{x}^T\mathbf{B}_1\mathbf{x} \leq \frac{1}{2}\mathbf{x}^T\mathbf{C}_1\mathbf{x} \leq V_2(\mathbf{r}_r) \leq \frac{1}{2}\mathbf{x}^T\mathbf{C}_2\mathbf{x} \leq \frac{1}{2}\mathbf{x}^T\mathbf{B}_2\mathbf{x} \tag{4.26}$$

where $\mathbf{x} = [\|\mathbf{e}_r\|, \|\mathbf{e}_v\|]^T$, and

$$\mathbf{C}_1 = \begin{bmatrix} \zeta k_d + \lambda_{\min}(\mathbf{W}(\mathbf{r}_r)) & -\zeta \\ -\zeta & 1 \end{bmatrix} \tag{4.27a}$$

$$\mathbf{C}_2 = \begin{bmatrix} \zeta k_d + \lambda_{\max}(\mathbf{W}(\mathbf{r}_r)) & \zeta \\ \zeta & 1 \end{bmatrix} \tag{4.27b}$$

$$\mathbf{B}_1 = \begin{bmatrix} \zeta k_d + \min(\Lambda_{\mathbf{W}}^{-}) & -\zeta \\ -\zeta & 1 \end{bmatrix} \tag{4.27c}$$

$$\mathbf{B}_2 = \begin{bmatrix} \zeta k_d + \max(\Lambda_{\mathbf{W}}^{+}) & \zeta \\ \zeta & 1 \end{bmatrix} \tag{4.27d}$$

Note that $\min(\Lambda_{\mathbf{W}}^{-})$ and $\max(\Lambda_{\mathbf{W}}^{+})$ denote the minimum and maximum elements of the set $\Lambda_{\mathbf{W}}^{-}$ and $\Lambda_{\mathbf{W}}^{+}$, respectively. For $\mathbf{B}_1$ and $\mathbf{B}_2$ to be positive

definite, all leading principal minors of $\mathbf{B}_1$ and $\mathbf{B}_2$ must be positive. The range of ζ satisfying these conditions can be obtained as follows,

$$-\frac{\min(\Lambda_{\mathbf{W}}^{-})}{k_d} < \zeta \tag{4.28a}$$

$$\frac{k_d - \sqrt{k_d^2 + 4\min(\Lambda_{\mathbf{W}}^{-})}}{2} < \zeta < \frac{k_d + \sqrt{k_d^2 + 4\min(\Lambda_{\mathbf{W}}^{-})}}{2} \tag{4.28b}$$

In addition, since ζ is a real number, the following relation must also be satisfied.

$$-\frac{k_d^2}{4} < \min(\Lambda_{\mathbf{W}}^{-}) \tag{4.29}$$

In short, the condition for $\mathbf{B}_1$ and $\mathbf{B}_2$ to be positive definite can be summarized as Eq. (4.25). If ζ satisfies Eq. (4.25), then positive definiteness of $V_2(\mathbf{r}_r)$ is guaranteed. □

Next, the time derivative of $V_2(\mathbf{r}_r)$ along Eq. (4.23) can be expressed as

$$\dot{V}_2(\mathbf{r}_r) = \mathbf{e}_r^T(\mathbf{W}(\mathbf{r}_r) + \zeta\mathbf{K}_d)\mathbf{e}_v + \frac{1}{2}\mathbf{e}_r^T\dot{\mathbf{W}}(\mathbf{r}_r)\mathbf{e}_r + \zeta\mathbf{e}_v^T\mathbf{e}_v + \zeta\mathbf{e}_r^T\dot{\mathbf{e}}_v + \mathbf{e}_v^T\dot{\mathbf{e}}_v \tag{4.30}$$

where

$$\begin{aligned}\mathbf{e}_v^T\dot{\mathbf{e}}_v =& -\boldsymbol{e}_v^T\mathbf{W}(\boldsymbol{r}_r)\boldsymbol{e}_r - k_d\|\boldsymbol{e}_v\|^2 + \mathbf{e}_v^T\big\{\boldsymbol{f}_{\text{cr3bp}}(\boldsymbol{X}) - \boldsymbol{f}_{\text{cr3bp}}(\boldsymbol{X}_r) + \mathbf{W}(\mathbf{r}_r)\varepsilon^2\boldsymbol{\eta}_1 + k_d\varepsilon\boldsymbol{\eta}_2 + \boldsymbol{\eta}_3\big\}\\ \leq& -\boldsymbol{e}_v^T\mathbf{W}(\boldsymbol{r}_r)\boldsymbol{e}_r - k_d\|\boldsymbol{e}_v\|^2 + \mathbf{e}_v^T\big\{\boldsymbol{f}_{\text{cr3bp}}(\boldsymbol{X}) - \boldsymbol{f}_{\text{cr3bp}}(\boldsymbol{X}_r) + \mathbf{W}(\mathbf{r}_r)\varepsilon^2\boldsymbol{\eta}_1\big\}\\ &+ \|\mathbf{e}_v\|\big\{k_d\varepsilon\|\boldsymbol{\eta}_2\| + \|\boldsymbol{\eta}_3\|\big\}\end{aligned} \tag{4.31a}$$

$$\begin{aligned}\zeta\mathbf{e}_r^T\dot{\mathbf{e}}_v =& \zeta\mathbf{e}_r^T\Big[\boldsymbol{f}_{\text{cr3bp}}(\boldsymbol{X}) - \boldsymbol{f}_{\text{cr3bp}}(\boldsymbol{X}_r) - \mathbf{W}(\mathbf{r}_r)\mathbf{e}_r - k_d\mathbf{e}_v + \mathbf{W}(\mathbf{r}_r)\varepsilon^2\boldsymbol{\eta}_1 + k_d\varepsilon\boldsymbol{\eta}_2 + \boldsymbol{\eta}_3\Big]\\ \leq& \zeta\mathbf{e}_r^T\big\{\boldsymbol{f}_{\text{cr3bp}}(\boldsymbol{X}) - \boldsymbol{f}_{\text{cr3bp}}(\boldsymbol{X}_r)\big\} - \zeta\mathbf{e}_r^T\mathbf{W}(\mathbf{r}_r)\mathbf{e}_r - \zeta k_d\mathbf{e}_r^T\mathbf{e}_v + \zeta\mathbf{e}_r^T\mathbf{W}(\mathbf{r}_r)\varepsilon^2\boldsymbol{\eta}_1\\ &+ \zeta\|\mathbf{e}_r\|\big\{k_d\varepsilon\|\boldsymbol{\eta}_2\| + \|\boldsymbol{\eta}_3\|\big\}\end{aligned} \tag{4.31b}$$

$$\begin{aligned}\boldsymbol{f}_{\text{cr3bp}}(\boldsymbol{X}) - \boldsymbol{f}_{\text{cr3bp}}(\boldsymbol{X}_r) &= 2\Omega_f \mathbf{J}\mathbf{e}_v + \left[\frac{\partial U(\mathbf{r})}{\partial \mathbf{r}}\right]^T - \left[\frac{\partial U(\mathbf{r}_r)}{\partial \mathbf{r}_r}\right]^T \\ &= 2\Omega_f \mathbf{J}\mathbf{e}_v - \Omega_f^2 \mathbf{J}\mathbf{J}\mathbf{e}_r - \left[\frac{\partial V(\mathbf{r})}{\partial \mathbf{r}}\right]^T + \left[\frac{\partial V(\mathbf{r}_r)}{\partial \mathbf{r}_r}\right]^T\end{aligned} \tag{4.31c}$$

Because the Lagrange-Dirichlet theorem only guarantees the local stability of the equilibrium, the stability of the controller proposed in this study is valid only near the equilibrium point. Therefore, using Eq. (4.31) and the linearized equation of $\boldsymbol{f}_{\text{cr3bp}}(\boldsymbol{X})$, the following relation can be obtained.

$$\begin{aligned}\dot{V}_2(\mathbf{r}_r) \leq (\zeta - k_d)\|\mathbf{e}_v\|^2 + (\|\mathbf{e}_v\| + \zeta\|\mathbf{e}_r\|)(k_d\varepsilon\|\boldsymbol{\eta}_2\| + \|\boldsymbol{\eta}_3\|) - \zeta\mathbf{e}_r^T\mathbf{W}(\mathbf{r}_r)\mathbf{e}_r + \frac{1}{2}\max(\Lambda_{\dot{\mathbf{W}}})\|\mathbf{e}_r\|^2 \\ + (\mathbf{e}_v^T + \zeta\mathbf{e}_r^T)\big[-\Omega_f^2\mathbf{J}\mathbf{J}\mathbf{e}_r - \nabla_{\text{rr}}^2 V(\mathbf{r}_r)\mathbf{e}_r + 2\Omega_f\mathbf{J}\mathbf{e}_v\big] + (\mathbf{e}_v^T + \zeta\mathbf{e}_r^T)\mathbf{W}(\mathbf{r}_r)\varepsilon^2\boldsymbol{\eta}_1\end{aligned} \tag{4.32}$$

where $\Lambda_{\dot{\mathbf{W}}}$ denotes a set of the maximum eigenvalue of the rate of time-varying potential shaping gain matrix during one period of the reference LPO. Additionally, using $\|\mathbf{e}_r\| \leq \|\mathbf{x}\|$, $\|\mathbf{e}_v\| \leq \|\mathbf{x}\|$, $\|\boldsymbol{\eta}_i\| \leq \|\boldsymbol{\eta}\|$, $i = 1, 2, 3$, and Cauchy-Schwarz inequality, the following inequality can be obtained.

$$\begin{aligned}\dot{V}_2(\mathbf{r}_r) \leq (\zeta - k_d)\|\mathbf{e}_v\|^2 + \|\mathbf{x}\|\|\boldsymbol{\eta}\|(1+\zeta)(k_d\varepsilon + 1) + \left[\frac{1}{2}\max(\Lambda_{\dot{\mathbf{W}}}) + (\Omega_f^2 - k_p)\zeta\right]\|\mathbf{e}_r\|^2 \\ + (\Omega_f^2 + 2\zeta)\|\mathbf{e}_v\|\|\mathbf{e}_r\| - \mathbf{e}_v^T\nabla_{\text{rr}}^2 V(\mathbf{r}_r)\mathbf{e}_r + (\mathbf{e}_v^T + \zeta\mathbf{e}_r^T)\mathbf{W}(\mathbf{r}_r)\varepsilon^2\boldsymbol{\eta}_1\end{aligned} \tag{4.33}$$

The last two terms of the Eq. (4.33) satisfy the following inequality.

$$-\mathbf{e}_v^T\nabla_{\text{rr}}^2 V(\mathbf{r}_r)\mathbf{e}_r \leq \|\mathbf{e}_v\|\|\mathbf{e}_r\|\max(|\Lambda_V|) \tag{4.34a}$$

$$(\mathbf{e}_v^T + \zeta\mathbf{e}_r^T)\mathbf{W}(\mathbf{r}_r)\varepsilon^2\boldsymbol{\eta}_1 \leq (1+\zeta)\varepsilon^2\max(|\Lambda_{\mathbf{W}}|)\|\mathbf{x}\|\|\boldsymbol{\eta}\| \tag{4.34b}$$

where $|\Lambda_V|$ and $|\Lambda_{\mathbf{W}}|$ denote a set of the maximum absolute value of eigenvalues of the $\nabla^2 V_{\text{rr}}(\mathbf{r}_r)$ and $\mathbf{W}(\mathbf{r}_r)$ during one period of the reference LPO, respectively. Then, using Eqs. (4.33) and (4.34), the following inequality can be

derived.

$$\dot{V}_2(\mathbf{r}_r) \leq -\mathbf{x}^T\mathbf{B}_0\mathbf{x} + \|\mathbf{x}\|\|\boldsymbol{\eta}\|(1+\zeta)\big[\varepsilon^2\max(|\Lambda_{\mathbf{W}}|) + k_d\varepsilon + 1\big] \tag{4.35}$$

where

$$\mathbf{B}_0 = \begin{bmatrix} B_{0,11} & B_{0,12} \\ B_{0,12} & B_{0,22} \end{bmatrix} \tag{4.36a}$$

$$B_{0,11} = -\frac{1}{2}\max(\Lambda_{\dot{\mathbf{W}}}) - (\Omega_f^2 - k_p)\zeta \tag{4.36b}$$

$$B_{0,12} = -\frac{1}{2}\big[\Omega_f^2 + 2\zeta + \max(|\Lambda_V|)\big] \tag{4.36c}$$

$$B_{0,22} = k_d - \zeta \tag{4.36d}$$

Following **Remark 4** provides a condition for ζ that matrix $\mathbf{B}_0$ in Eq. (4.35) is positive definite.

Remark 4. : The matrix $\mathbf{B}_0$ is positive definite if ζ satisfies the following condition.

$$\max\left\{\frac{\max(\Lambda_{\dot{\mathbf{W}}})}{2(k_p - \Omega_f^2)},\ \underline{\zeta}\right\} < \zeta < \bar{\zeta} \tag{4.37}$$

Let us investigate **Remark 4**. In order for $\mathbf{B}_0$ to be positive definite, $B_{0,11} > 0$ and $\det(\mathbf{B}_0) > 0$ must be satisfied. Note from Eq. (4.22) that $\dot{\mathbf{W}}(\mathbf{r}_r) = -d\big(\nabla^2_{\mathrm{rr}}V(\mathbf{r}_r)\big)/dt$, and therefore $\max(\Lambda_{\dot{\mathbf{W}}})$ is independent of control gain k_p and k_d. Also, the $\max(\Lambda_{\dot{\mathbf{W}}})$ value of the target LPO is always guaranteed to be positive as shown in Fig. 4.1.

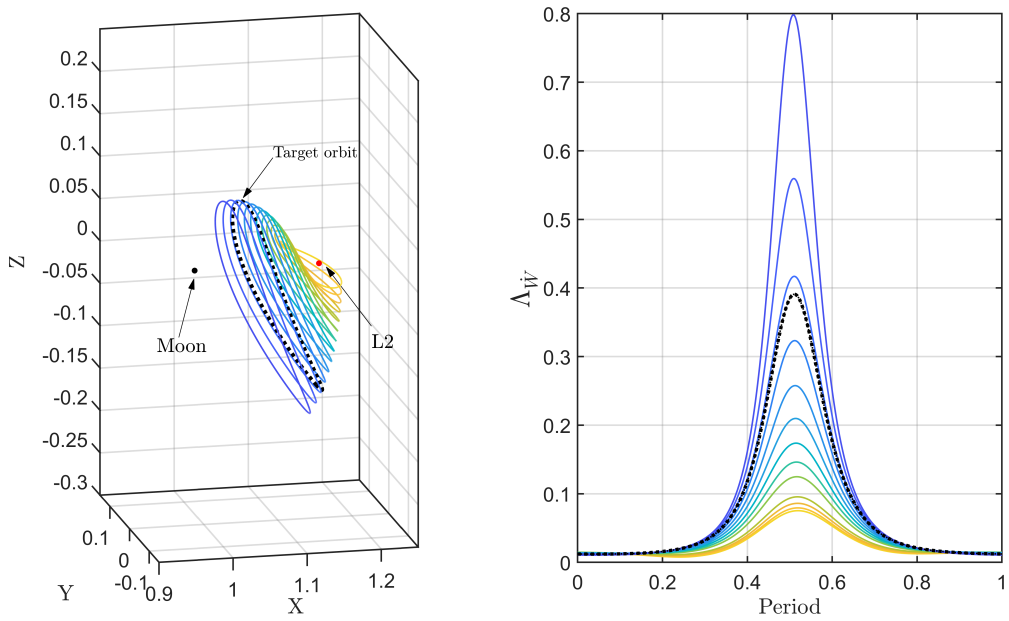

Figure 4.1 Set of maximum eigenvalue of $\Lambda_{\dot{\mathbf{W}}}$ during one-period of LPO (black dot line is a reference orbit)

For the condition $B_{0,11} > 0$, the range that ζ should be satisfied as follows,

$$\begin{cases} \zeta < -\frac{\max(\Lambda_{\dot{\mathbf{W}}})}{2\left(\Omega_f^2 - k_p\right)}, & \text{if} \quad 0 < k_p < \Omega_f^2 \\ \zeta > \frac{\max(\Lambda_{\dot{\mathbf{W}}})}{2\left(k_p - \Omega_f^2\right)} \quad , & \text{if} \quad k_p > \Omega_f^2 \end{cases} \tag{4.38}$$

Note from Eq. (4.38) that the positive condition of ζ is guaranteed only when $k_p > \Omega_f^2$. Next, the range of ζ to satisfy the condition $\det(\mathbf{B}_0) > 0$ can be obtained as follows,

$$\underline{\zeta} < \zeta < \bar{\zeta} \tag{4.39}$$

where

$$\underline{\zeta} = \frac{\zeta_1 - \sqrt{\zeta_2}}{2(k_p - \Omega_f^2 + 1)}, \qquad \bar{\zeta} = \frac{\zeta_1 + \sqrt{\zeta_2}}{2(k_p - \Omega_f^2 + 1)} \tag{4.40a}$$

$$\zeta_1 = k_d(k_p - 1) - \left[1 + \max(|\Lambda_V|)\right] + \frac{1}{2}\max(\Lambda_{\dot{\mathbf{W}}}) \tag{4.40b}$$

$$\zeta_2 = \zeta_1^2 - 4(k_p - \Omega_f^2 + 1)\left[\frac{k_d}{2}\max(\Lambda_{\dot{\mathbf{W}}}) + \frac{1}{4}\left\{1 + \max(|\Lambda_V|)\right\}^2\right] \tag{4.40c}$$

Since ζ is a real number, ζ_2 should be positive. Equation (4.40) shows that $\zeta_2 > 0$ is satisfied for sufficiently large ζ_1, i.e., sufficiently large k_p and k_d. Also, note from Eq. (4.40c) that $\zeta_1^2 - \zeta_2 > 0$ always holds for $k_p > \Omega_f^2 - 1$ and $k_d > 0$, and therefore $\underline{\zeta} > 0$ is guaranteed. In addition, from Eqs. (4.38) and (4.40), the following inequality also satisfies for sufficiently large k_p and k_d.

$$\frac{\max(\Lambda_{\dot{\mathbf{W}}})}{2(k_p - \Omega_f^2)} < \bar{\zeta} \tag{4.41}$$

Therefore, for sufficiently large k_p and k_d, there exists a positive ζ satisfying Eq. (4.37), and then the positive definiteness of $\mathbf{B}_0$ is guaranteed. Finally, following **Theorem 3** provides the stability analysis of the proposed controller for the spacecraft in the vicinity of LPO.

Theorem 3. In the vicinity of LPO, applying the proposed FEHGO based Hamiltonian structure-based control, Eq. (4.21), the LPO tracking error is uniformly ultimately bounded.

Proof. From Eq. (4.22), $\min(\Lambda_{\mathbf{W}}^{-}) > 0$ is guaranteed for sufficiently large k_p. From Eq. (4.25), following inequality is also satisfied for sufficiently large k_p and k_d.

$$\frac{\max(\Lambda_{\dot{\mathbf{W}}})}{2(k_p - \Omega_f^2)} < \frac{k_d + \sqrt{k_d^2 + 4\min(\Lambda_{\mathbf{W}}^{-})}}{2} \tag{4.42}$$

In addition, from Eqs. (4.40a) and (4.40b), it is observed that $\underline{\zeta}$ satisfies the following inequality.

$$\begin{aligned}\underline{\zeta} &< \frac{\zeta_1}{2(k_p - \Omega_f^2 + 1)} \\ &< \frac{k_d k_p}{2(k_p - \Omega_f^2 + 1)} + \frac{\max(\Lambda_{\dot{\mathbf{W}}})}{4(k_p - \Omega_f^2 + 1)}\end{aligned} \tag{4.43}$$

From Eqs. (4.25) and (4.43), the following relation holds for sufficiently large k_p and k_d.

$$\begin{aligned}\underline{\zeta} &< \frac{k_d k_p}{2(k_p - \Omega_f^2 + 1)} + \frac{\max(\Lambda_{\dot{\mathbf{W}}})}{4(k_p - \Omega_f^2 + 1)} \\ &< \frac{k_d + \sqrt{k_d^2 + 4\min(\Lambda_{\mathbf{W}}^-)}}{2}\end{aligned} \tag{4.44}$$

Therefore, by Eqs. (4.25), (4.37), (4.42) and (4.44), positive ζ always exists within the following inequality such that $\mathbf{B}_1, \mathbf{B}_2,$ and $\mathbf{B}_0$ are positive definite for sufficiently large $k_p \gg \Omega_f^2$ and k_d.

$$\max\left\{\frac{\max(\Lambda_{\dot{\mathbf{W}}})}{2(k_p - \Omega_f^2)},\ \underline{\zeta}\right\} < \zeta < \min\left\{\frac{k_d + \sqrt{k_d^2 + 4\min(\Lambda_{\mathbf{W}}^-)}}{2},\ \bar{\zeta}\right\} \tag{4.45}$$

Now, from Eq. (4.26), the following relation can be obtained.

$$\frac{2V_2}{\lambda_{\max}(\mathbf{B}_2)} \leq \|\mathbf{x}\|^2 \leq \frac{2V_2}{\lambda_{\min}(\mathbf{B}_1)} \tag{4.46}$$

Substituting Eq. (4.46), $\dot{V}_2 = 2\sqrt{V_2}\big(d\sqrt{V_2}/dt\big)$, and Eq. (4.18) into Eq. (4.35), we have

$$\begin{aligned}\frac{d\sqrt{V_2(\mathbf{r}_r)}}{dt} &\leq -c_3\sqrt{V_2(\mathbf{r}_r)} + \frac{\|\boldsymbol{\eta}\|(1+\zeta)\big[\varepsilon^2\max(|\Lambda_{\mathbf{W}}|) + k_d\varepsilon + 1\big]}{\sqrt{2\lambda_{\min}(\mathbf{B}_1)}} \\ &\leq -c_3\sqrt{V_2(\mathbf{r}_r)} + \frac{(1+\zeta)\big[\varepsilon^2\max(|\Lambda_{\mathbf{W}}|) + k_d\varepsilon + 1\big]}{\sqrt{2\lambda_{\min}(\mathbf{B}_1)}}(c_1 e^{c_0 t} - c_2)\end{aligned} \tag{4.47}$$

where

$$c_1 = \frac{\sqrt{V_1(0)}}{\sqrt{\lambda_{\min}(\boldsymbol{P})}} + c_2 \tag{4.48a}$$

$$c_2 = \frac{(\gamma_h + \frac{\gamma_{ns}}{\varepsilon^3})\lambda_{\max}(\boldsymbol{P})}{c_0\lambda_{\min}(\boldsymbol{P})} \tag{4.48b}$$

$$c_3 = \frac{\lambda_{\min}(\mathbf{B}_0)}{\lambda_{\max}(\mathbf{B}_2)} \tag{4.48c}$$

Integrating both sides of Eq. (4.47) from 0 to t yields

$$\begin{aligned}\sqrt{V_2(\mathbf{r}_r(t))} \leq & \sqrt{V_2(\mathbf{r}_r(0))} + \frac{(1+\zeta)\left[\varepsilon^2\max(|\Lambda_{\mathbf{W}}|) + k_d\varepsilon + 1\right]}{\sqrt{2\lambda_{\min}(\mathbf{B}_1)}}\left[\frac{c_1}{c_0}(e^{c_0 t} - 1) - c_2 t\right] \\ & - \int_0^t c_3\sqrt{V_2(\mathbf{r}_r(\tau))}d\tau\end{aligned} \tag{4.49}$$

Lastly, applying the Gronwall-Bellman inequality [106] to Eq. (4.49), $\sqrt{V_2(\mathbf{r}_r(t))}$ has the following bounded solution.

$$\begin{aligned}&\sqrt{V_2(\mathbf{r}_r(t))} \leq \\ &\begin{cases} \frac{(1+\zeta)\left[\varepsilon^2\max(|\Lambda_{\mathbf{W}}|)+k_d\varepsilon+1\right]}{\sqrt{2\lambda_{\min}(\mathbf{B}_1)}}\left[\left\{\frac{c_1 c_3}{c_0(c_0+c_3)} + \frac{c_2}{c_3} - \frac{c_1}{c_0}\right\}e^{-c_3 t} + \frac{c_1}{(c_0+c_3)}e^{c_0 t} - \frac{c_2}{c_3}\right] & \text{if} \quad c_0 \neq -c_3 \\ +\sqrt{V_2(\mathbf{r}_r(0))}e^{-c_3 t} \\ \frac{(1+\zeta)\left[\varepsilon^2\max(|\Lambda_{\mathbf{W}}|)+k_d\varepsilon+1\right]}{\sqrt{2\lambda_{\min}(\mathbf{B}_1)}}\left[\left\{\frac{c_2}{c_3} + c_1 t\right\}e^{-c_3 t} - \frac{c_2}{c_3}\right] + \sqrt{V_2(\mathbf{r}_r(0))}e^{-c_3 t}, & \text{if} \quad c_0 = -c_3 \end{cases}\end{aligned} \tag{4.50}$$

Note that c_0 can be made negative as mentioned previously. Therefore, using $c_0 < 0$, $c_2 < 0$, $c_3 > 0$, $c_3 = \lambda_{\min}(\mathbf{B}_0)/\lambda_{\max}(\mathbf{B}_2)$, Eq. (4.50), and Eq. (4.46), it can be shown that LPO tracking error state $\mathbf{x} = [\|\mathbf{e}_r\|, \|\mathbf{e}_v\|]^T$ converges, that is,

$$\limsup_{t\to\infty}\|\mathbf{x}(t)\| \leq -c_2(1+\zeta)\left[\varepsilon^2\max(|\Lambda_{\mathbf{W}}|) + k_d\varepsilon + 1\right]\frac{\lambda_{\max}(\mathbf{B}_2)}{\lambda_{\min}(\mathbf{B}_1)\lambda_{\min}(\mathbf{B}_0)} \tag{4.51}$$

□

The above stability analysis for LPO tracking is an extended version of the analysis of Gui [107], which analysed the stability of hovering spacecraft for an equilibrium point around an asteroid. Gui's analysis showed a global stability using a controller that exactly cancels the nonlinear equation of motion around the asteroid. On the other hand, the controller proposed in this study only locally reshapes the gravitational potential around the LPO considering the Hamiltonian structure. In addition, the analysis showed the entire closed-loop stability using the FEHGO with an improved filtering effect even though the navigation error is relatively large. Finally, the convergence analysis of the FEHGO based Hamiltonian structure-based controller is advantageous in that it can be applied to any trajectory tracking problem having a Hamiltonian structure.

Chapter 5

Numerical Simulations

In this chapter, numerical simulations are performed to demonstrate the performance of the proposed controller and observer. Acceptable external disturbance and navigation error are taken into account.

5.1 Disturbance Model

According to [27] and [29], the most significant perturbative force in the simplified CR3BP is the effect of the eccentricity of the Earth orbits and lunar orbits. For this reason, in this study, numerical simulation is performed under the elliptic restricted 3-body problem (ER3BP) model, which is a variant of the CR3BP considering the orbital eccentricity. The ER3BP used in the simulation can be written as follows [108],

$$x'' - 2y' = \frac{\partial \omega}{\partial x} \tag{5.1a}$$

$$y'' + 2x' = \frac{\partial \omega}{\partial y} \tag{5.1b}$$

$$z'' + z = \frac{\partial \omega}{\partial z} \tag{5.1c}$$

where

$$\omega(x, y, z, f) = \frac{1}{1 + e\cos f}\Psi(x, y, z) \tag{5.2a}$$

$$\Psi(x,y,z) = \frac{1}{2}(x^2+y^2+z^2) + \frac{1-\mu}{r_1} + \frac{\mu}{r_2} + \frac{1}{2}\mu(1-\mu) \tag{5.2b}$$

Note that f and $(\cdot)'$ denote a true anomaly and a derivative of $(\cdot)$ with respect to true anomaly, respectively. Additionally, e is the eccentricity and is approximately 0.0554 in the Earth-Moon system. By the chain rule, $(\cdot)'$ has the following relation with a time derivative of $(\cdot)$.

$$(\cdot)' = \frac{d(\cdot)}{df} = \frac{d(\cdot)}{dt}\cdot\frac{dt}{df} = \frac{d(\cdot)}{dt}\cdot\frac{(1-e^2)^{3/2}}{(1+e\cos f)^2} \tag{5.3}$$

Using Eqs. (5.1) and (5.3), the ER3BP in the time domain can be expressed as follows,

$$\ddot{x} + 2\dot{f}\left[\frac{\sin f}{(1+e\cos f)}\dot{x} - \dot{y}\right] = \frac{\dot{f}^2}{1+e\cos f}\left[x - \frac{(1-\mu)(x+\mu)}{r_1^3} - \frac{\mu(x-1+\mu)}{r_2^3}\right] \tag{5.4a}$$

$$\ddot{y} + 2\dot{f}\left[\frac{\sin f}{(1+e\cos f)}\dot{y} + \dot{x}\right] = \frac{\dot{f}^2}{1+e\cos f}\left[y - \frac{(1-\mu)y}{r_1^3} - \frac{\mu y}{r_2^3}\right] \tag{5.4b}$$

$$\ddot{z} + 2\frac{\sin f}{(1+e\cos f)}\dot{f}\dot{z} + \dot{f}^2 z = -\frac{\dot{f}^2}{1+e\cos f}\left[\frac{(1-\mu)z}{r_1^3} + \frac{\mu z}{r_2^3}\right] \tag{5.4c}$$

In this study, controller and observer are designed based on the CR3BP model, and numerical simulation is performed under Eq. (5.4).

5.2 Navigation Error Model

Navigation accuracy is crucial in deep-space station-keeping missions because more accurate orbit control is possible if more precise spacecraft navigation is used. Moreover, if the navigation is perfect, that is, if perfect navigation information is provided without measurement noise, then the EHGO may almost completely reject the disturbance. Unfortunately, navigation errors always exist in the real environment, especially in deep-space missions. According

to [27], [109], and [110], standard deviations of the position error ($1\sigma_{x,y,z}$) of the spacecraft are approximately 1 km for the Earth-Moon system, and 10 km for the Sun-Earth system. In addition, initial orbit injection error is approximately 0.1∼1 km for each direction [26]. Therefore, in this study, numerical simulation is performed considering 2 km of initial orbit injection error for each direction and the position measurement with 1 km of random error.

5.3 Simulation Results

Nominal orbit considered in the simulation is one of the various candidate LPOs for the lunar south pole coverage [111], which is shown in Fig. 5.1. The properties of the nominal orbit, i.e., halo orbit are summarized in Table 5.1, and the parameters of the Earth-Moon CR3BP system used in the simulation are summarized in Table 5.2. As mentioned in Chapter 3, when designing the potential shaping of the Hamiltonian structure-based control, Eq. (3.27), it may not be possible to use the exact $\nabla^2_{\mathrm{qq}}V(\mathbf{q}_r)$ value, i.e., $\nabla^2_{\mathrm{rr}}V(\mathbf{r}_r)$, which changes constantly. Therefore, in this study, a more feasible control input using the constant $\nabla^2_{\mathrm{rr}}V(\mathbf{r}^*_r)$ for a certain time interval of the reference orbit was designed, where $\mathbf{r}^*_r$ denotes a representative point for each orbit piece during a certain time interval. One period of nominal LPO is divided into 50 equal parts, and the trajectory corresponding to each time interval could be regarded as an individual orbit piece. In other words, the potential shaping control is designed with a new $\nabla^2_{\mathrm{rr}}V(\mathbf{r}^*_r)$ every 14/50 days (= 6.72 hr.).

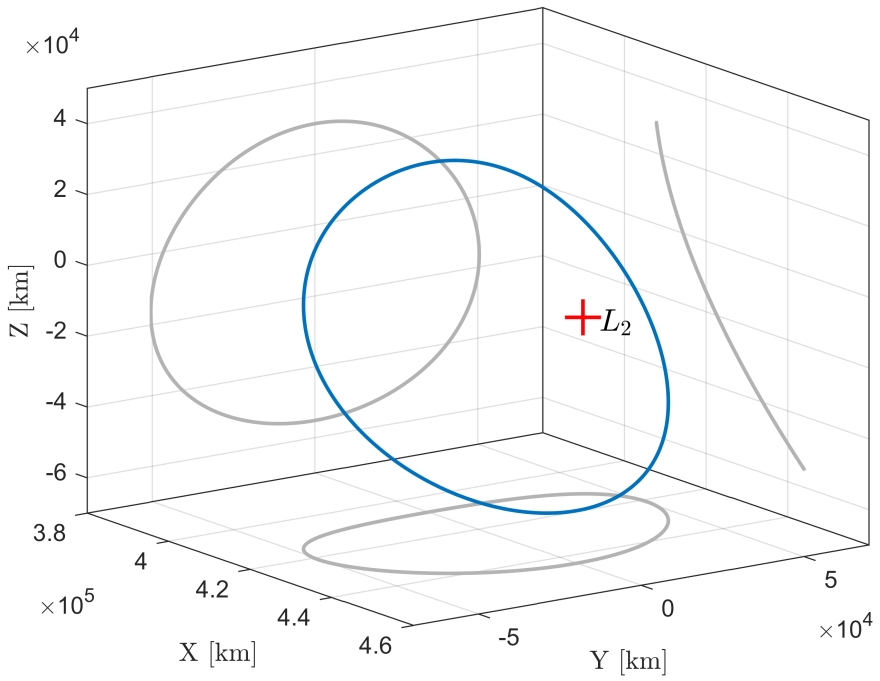

Figure 5.1 Nominal halo orbit

Table 5.1 Nominal halo orbit parameter values

Quantity	**Value**	**Units**
Z-amp.	-55,154.03	km
Period	14	days
Jacobi constant	3.07607	N/A

Table 5.2 System parameter values

Quantity	**Value**	**Units**
Gravitational constant	6.674×10^{-20}	$\mathrm{km^3kg^{-1}s^{-2}}$
Earth mass (m_1)	5.972×10^{24}	kg
Moon mass (m_2)	7.347×10^{22}	kg
Mass parameter (μ)	0.01215	N/A
Characteristic length (l^*)	385,692.5	km
Characteristic Time (t^*)	4.364	days

5.3.1 Simulation 1

First of all, a numerical simulation is carried out to illustrate the performance of the proposed switching Hamiltonian structure-preserving control. Model uncertainty, external disturbance, navigation error, and orbit injection error are not considered in this simulation scenario to evaluate the developed algorithm. The relative circular orbit size of the spacecraft is chosen similar to the TPF mission requirements [34]. Specific values of the radii of the transfer orbits and the initial values of the spacecraft are summarized in Tables 5.3 and 5.4, respectively. Figures 5.2 $\sim$ 5.5 present the relative position of each spacecraft, and Figs. 5.6 $\sim$ 5.8 present the control inputs for each spacecraft. Simulation results show that the size of the relative circular motion of the spacecraft can be changed by applying the switching Hamiltonian structure-preserving control. However, as the radius of the relative circular orbit decreases, the rotating frequency and magnitude of the maximum control input increases. That means, as shown in Fig. 5.4, converging to the reference trajectory using the switching Hamiltonian structure-preserving control is not efficient in the propellant consumption viewpoint. For instance, as the relative orbital radius of

the spacecraft decreases by two times, from $R_1 = 50m$ to $R_2 = 25m$, the mode frequency of each mode increases by approximately four times from $\omega = 40$ to $\omega = 160$, and the required maximum control input magnitude increases from $|a_{\max}(t)| = 4.81 \times 10^{-7} m/s^2$ to $3.7 \times 10^{-6} m/s^2$. To compare the consumption of the propellant, $\int_0^T |a(t)|dt$ is calculated for one period of the reference orbit. For the spacecraft with rotation frequency $\omega = 40$, maneuver cost is approximately $(0.3691, 0.3692, 0.3539)m/s$ for each direction (x, y, z). Likewise, for the spacecraft with rotation frequency $\omega = 160$, orbit maintenance cost is $(2.8626, 2.8570, 2.8316)m/s$. Lastly, consider a somewhat extreme condition, an initial position offset from the nominal orbit of $2,000km$ is considered. Figure. 5.9 shows that the switching Hamiltonian structure-preserving controller works well even though the spacecraft is far from the reference orbit.

Table 5.3 Radius of transfer orbit

	Spacecraft No.1	**Spacecraft No.2**	**Spacecraft No.3**
R_1 [m]	50	50	50
R_2 [m]	100	25	50

Table 5.4 Initial values of spacecrafts

Quantity	**Value**
Frequency (ω)	40
Plane orientation ($\bar{n}$)	(1,1,1)
Spacecraft No.1 position direction	(1,1,-2)
Spacecraft No.2 position direction	(1,-2,1)
Spacecraft No.3 position direction	(-2,1,1)

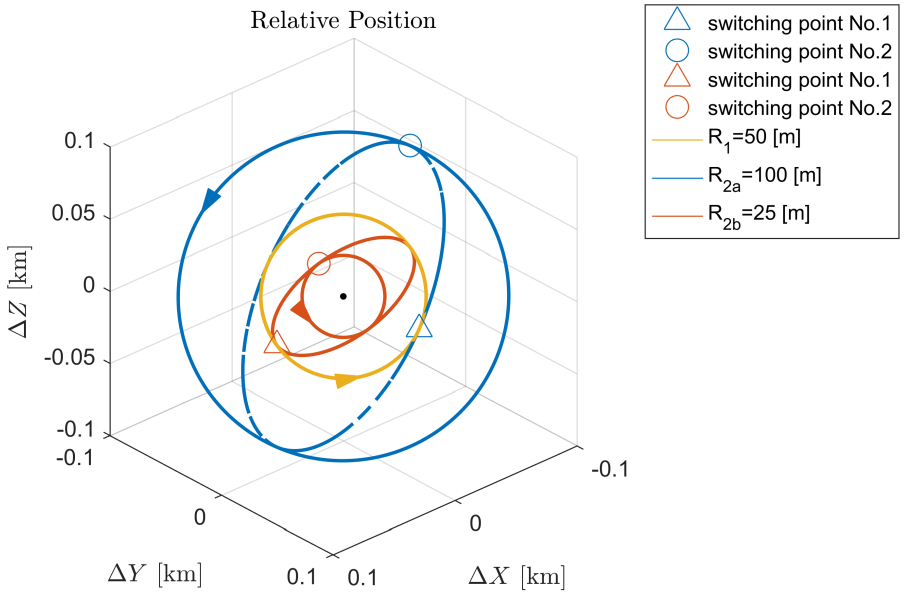

Figure 5.2 Orbit transfer using switching HSP control (relative motion)

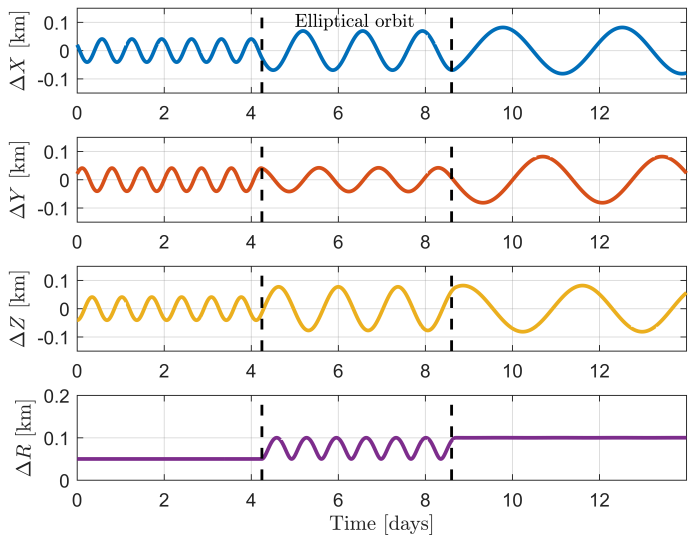

Figure 5.3 Relative position of spacecraft No.1 (from $R_1 = 50m$ to $R_2 = 100m$)

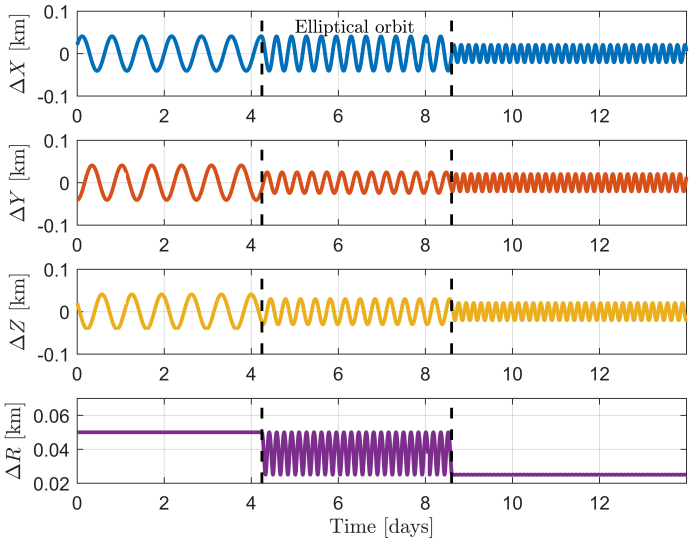

Figure 5.4 Relative position of spacecraft No.2 (from $R_1 = 50m$ to $R_2 = 25m$)

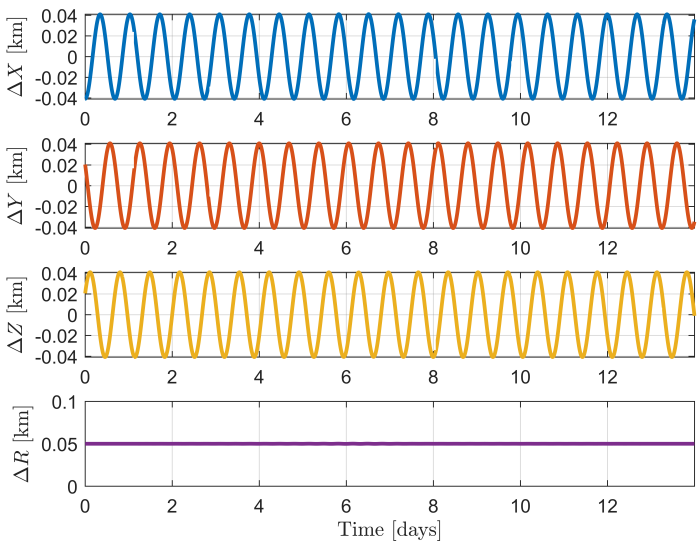

Figure 5.5 Relative position of spacecraft No.3 ($R = 50m$)

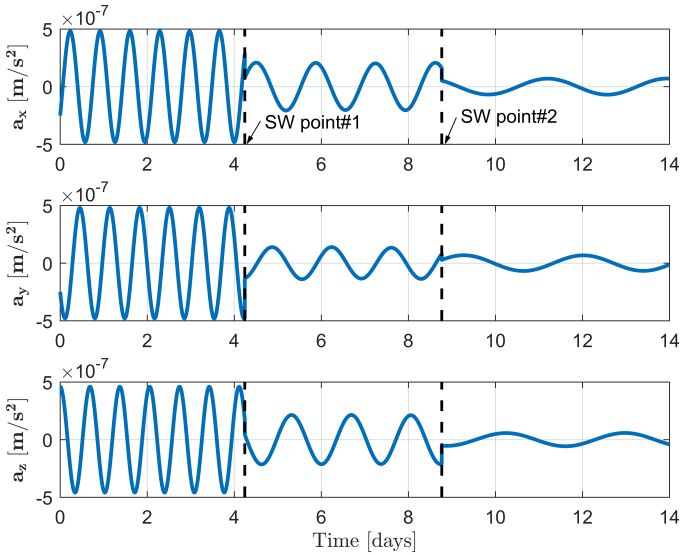

Figure 5.6 Control input of spacecraft No.1 (from $R_1 = 50m$ to $R_2 = 100m$)

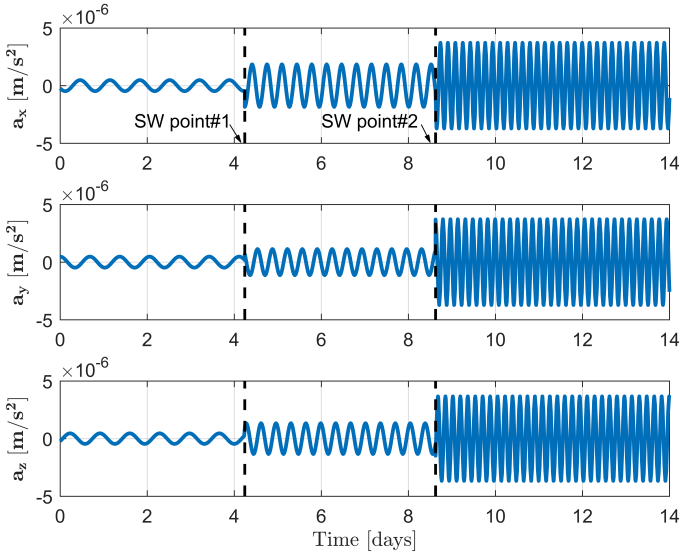

Figure 5.7 Control input of spacecraft No.2 (from $R_1 = 50m$ to $R_2 = 25m$)

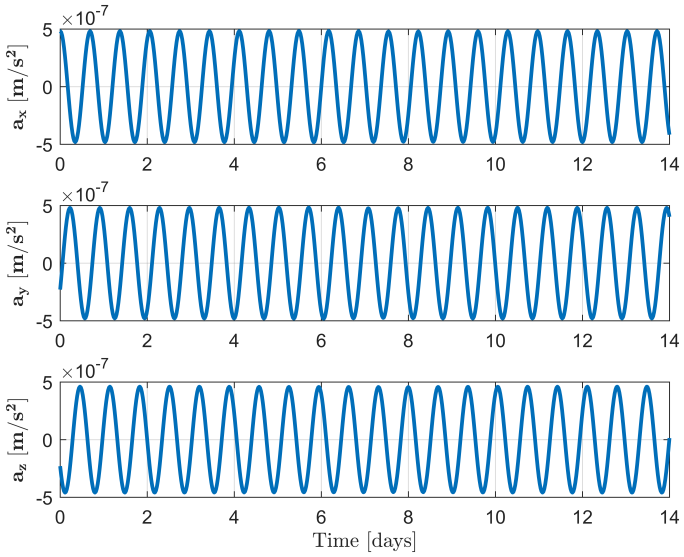

Figure 5.8 Control input of spacecraft No.3 ($R = 50m$)

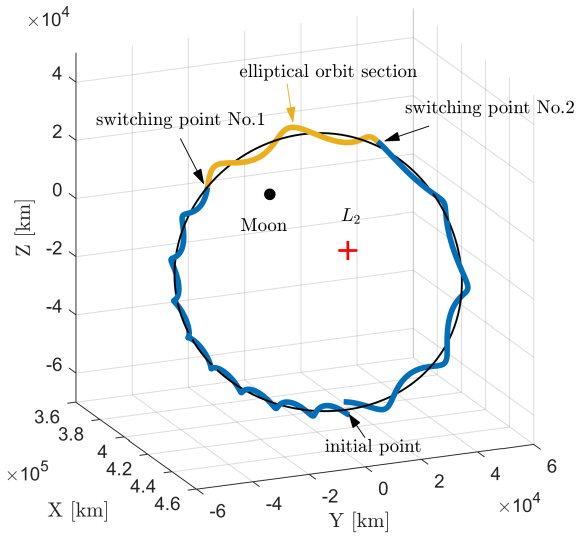

Figure 5.9 Exaggerated orbit size formation flying scenario along halo orbit (from $R_1 = 2,000km$ to $R_2 = 3,000km$)

5.3.2 Simulation 2

In this scenario, numerical simulation is performed to examine how station-keeping performance of a spacecraft using conventional Hamiltonian structure-preserving control deteriorates when model uncertainty and disturbance exist. For this, the Hamiltonian structure-preserving controller proposed by Xu and Xu [54] is chosen, and the initial orbit injection error is set to $2km$ in each direction as in other simulation environments. It is also assumed that relative navigation error does not exist for the Hamiltonian structure-preserving control. Figure 5.10 shows the relative trajectories of spacecraft to the nominal orbit in each case with and without disturbance during three periods of orbit. Figure 5.11 shows the relative distance and magnitude of the relative velocity

of the spacecraft. In the absence of disturbance and model uncertainty, that is, under the CR3BP environment, the mean values of the relative distance and relative velocity of the spacecraft to the nominal orbit are about $1.831km$ and $0.244m/s$, respectively. Compared with this, however, in the presence of disturbance and model uncertainty, that is, under the ER3BP environment, the magnitudes of the relative distance and relative velocity are approximately $84.448km$ and $4.429m/s$, respectively. From the simulation result, it can be observed that the performance of the existing Hamiltonian structure-preserving controller is significantly degraded when model uncertainty and external disturbance exist, which demonstrates the need to improve the performance of the existing Hamiltonian structure-preserving controllers. The station-keeping performance of the Hamiltonian structure-based controller proposed in this study will be shown in the following simulation.

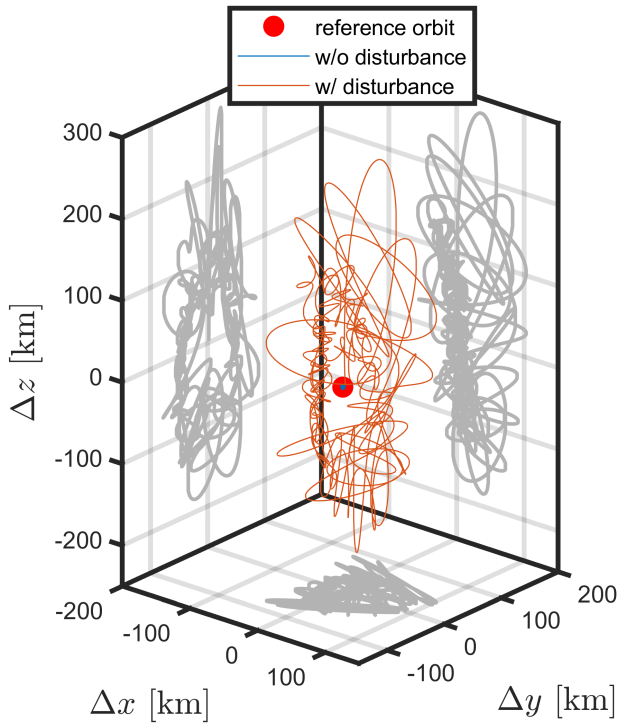

Figure 5.10 Relative trajectory of spacecraft with respect to the reference LPO under Xu's HSP controller (with and without disturbance, $G_1 = G_2 = 300$, $G_3 = 200$, $\Delta = 0$)

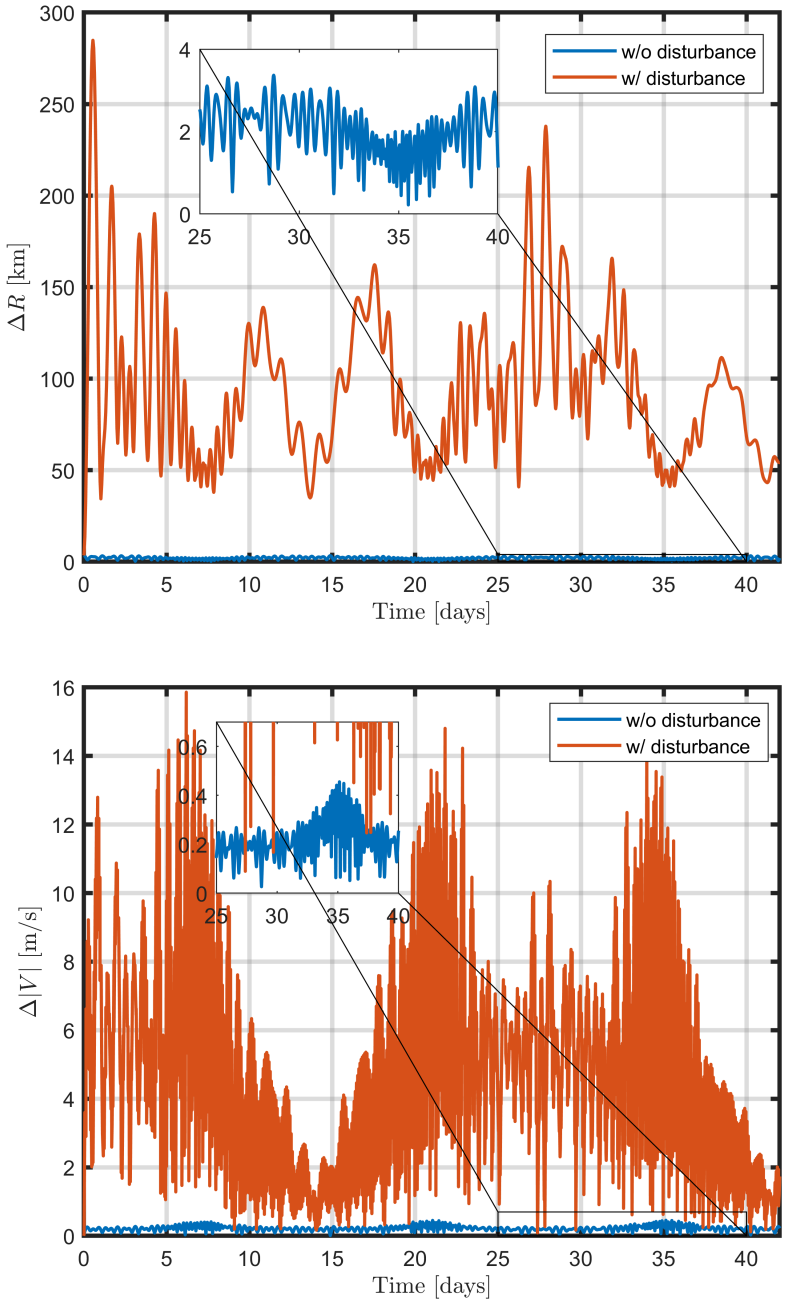

Figure 5.11 Relative distance and velocity with respect to the reference LPO under Xu's HSP controller (with and without disturbance, $G_1 = G_2 = 300$, $G_3 = 200$, $\Delta = 0$)

5.3.3 Simulation 3

The station-keeping simulation of the spacecraft is performed under various conditions by applying the proposed strategy in this study. Figures 5.12 and 5.13 show the estimation errors of the state and disturbance of EHGO and FEHGO for the case of no navigation error. The poles of the EHGO and FEHGO are placed at $\{-220, -210, -200\}$ and $\{-220, -210, -200, -p\}$ in each direction, respectively, and p is an arbitrary positive real number. The FEHGO has one more degree-of-freedom in each direction than the EHGO in the pole assignment, because the integral state is added in comparison with the EHGO. Figures 5.12 and 5.13 show that when the poles of the EHGO and FEHGO are placed at similar locations and there are no navigation errors, the EHGO estimates the state and disturbance more precisely. This result can be seen as a result of the phase delay effect, which occurs as FEHGO feedbacks the integral state. In addition, as the p value increases, the estimation accuracy of the FEHGO converges to that of the EHGO. This can be thought of as a result of the relaxation of the phase delay effect because the observer dynamics corresponding to the integral state become faster.

On the other hand, in the presence of navigation error, Figs. 5.14 and 5.15 show that the state and disturbance estimation accuracy of the FEHGO are higher than those of EHGO due to the noise filtering effect of FEHGO itself. To ensure a fair performance comparison, the sampling time for both observers was set to 12 seconds. There exists still a trade-off between noise attenuation and the phase delay effect depending on the p value. This property is similar to that of the low-pass-filter (LPF), and therefore the FEHGO can be thought of as an observer in the form of LPF and EHGO combined. As shown in Figure 5.16,

the control input using the state estimated by the FEHGO becomes smoother, which is more appropriate to be implemented in a real propulsion system, such as a continuous low-thrust thruster.

Note that the state and disturbance estimated by the FEHGO are smoother than those by the EHGO. Therefore, a higher observer gain than the EHGO at the allowable noise level could be tuned in designing the control input. Figures 5.17 and 5.18 show the estimation error of the state and disturbance during 10 periods of orbit, when the poles of the EHGO and FEHGO are on $\{-120, -110, -100\}$ and $\{-220, -210, -200, -190\}$, respectively. Although the dynamics of the FEHGO are faster, that is, the observer gain is higher, the noise level of estimation error is comparable. The mean values of the state and disturbance estimation error are summarized in Table 5.5. Figure 5.19 shows the LPO tracking error using the identical Hamiltonian structure-based controller with $k_p = 3,600$ and $k_d = 10$, and Fig. 5.20 shows the control inputs. As shown in Figs. 5.19 and 5.20, spacecraft tracks the target LPO well within a specific bound. Additionally, the LPO position tracking error bound of the FEHGO is smaller than that of the EHGO. The mean and standard deviation of the tracking error are summarized in Table 5.6. Obviously, for the FEHGO to work properly, it is inevitable that a significant amount of computational power is required to conduct large amount of computations quickly. It can generally be expected that there will be no significant difference compared with the amount of computation required in the orbit determination process using filter. Also, the peaking phenomenon due to the high-gain observer may adversely affect the initial tracking performance. However, this problem can be solved by setting the adequate control input saturation.

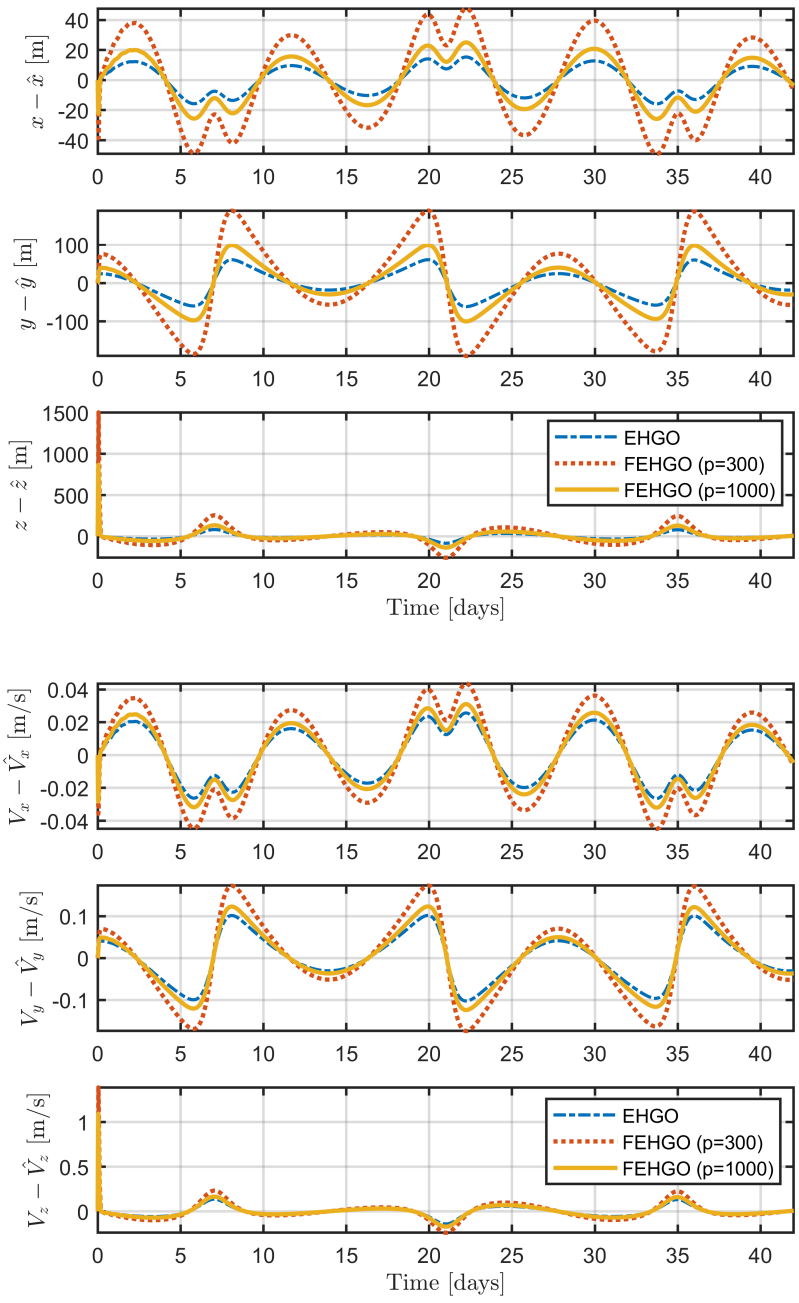

Figure 5.12 Position and velocity estimation error without navigation error

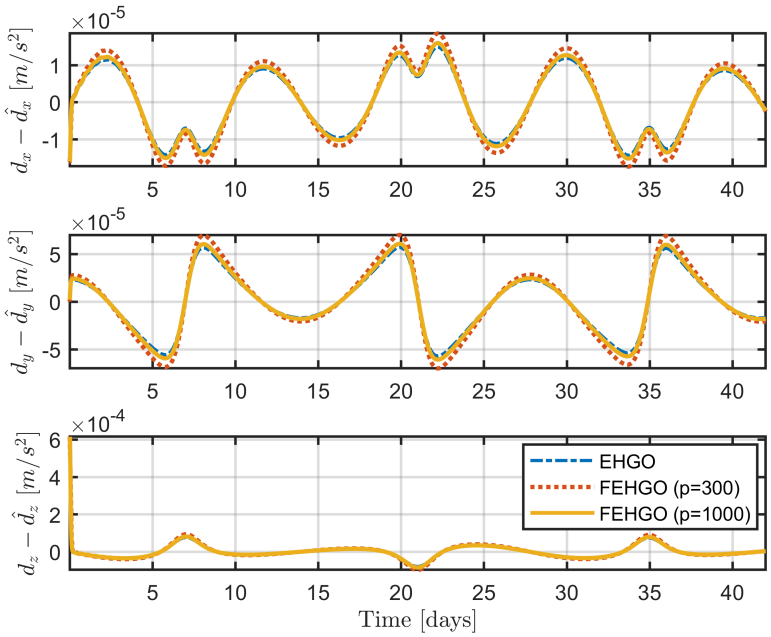

Figure 5.13 Disturbance estimation error without navigation error

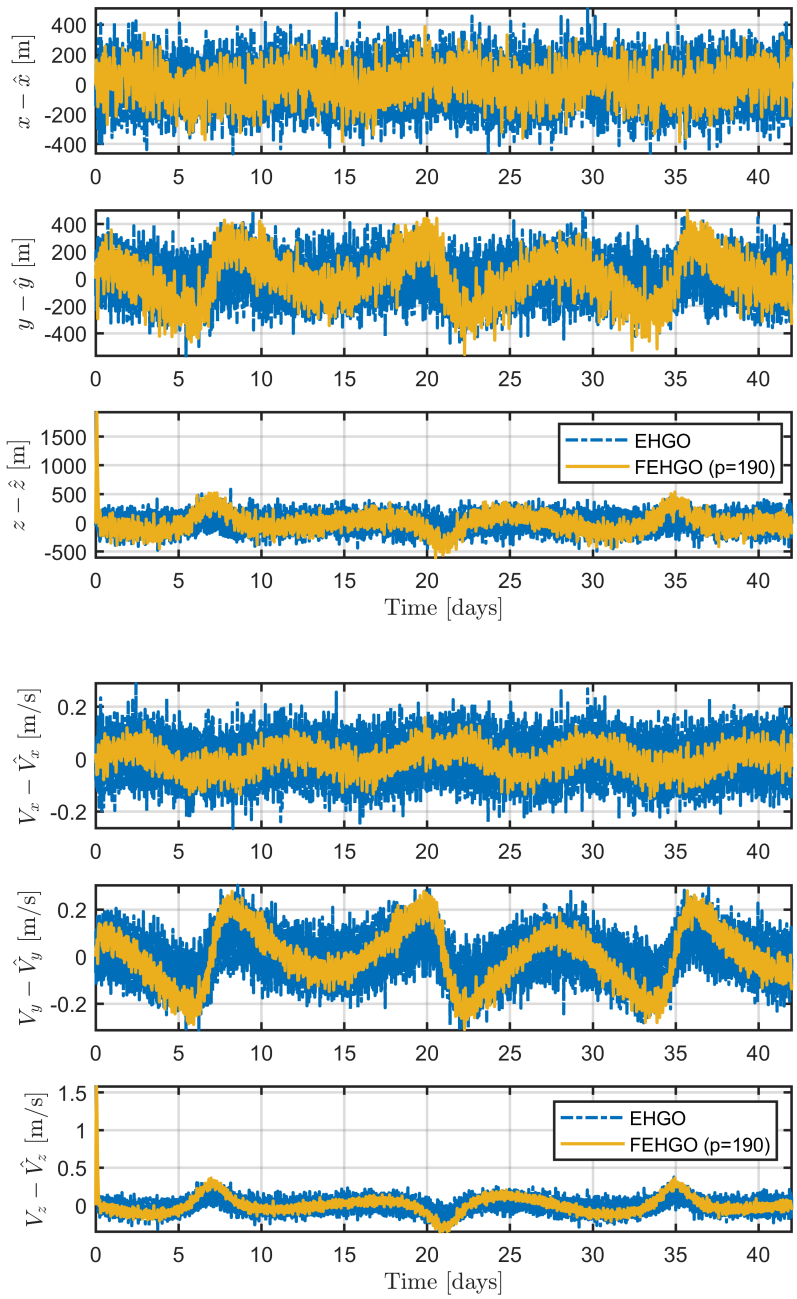

Figure 5.14 Position and velocity estimation error with navigation error ($1\sigma_{x,y,z}$ = 1 km)

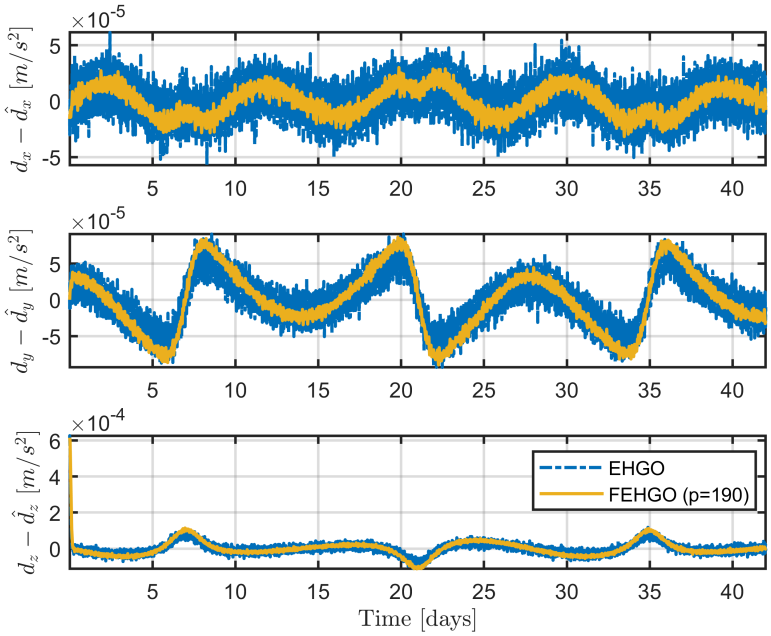

Figure 5.15 Disturbance estimation error with navigation error ($1\sigma_{x,y,z} = 1$ km)

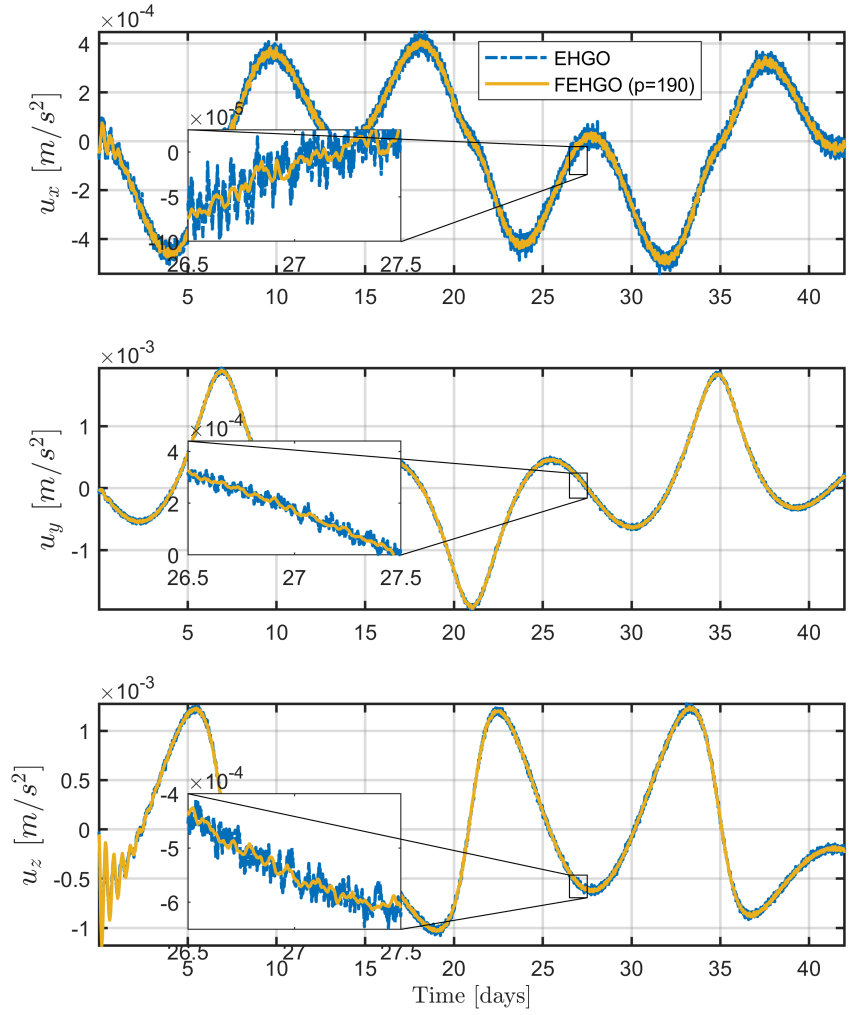

Figure 5.16 Control input history with navigation error ($1\sigma_{x,y,z} = 1$ km)

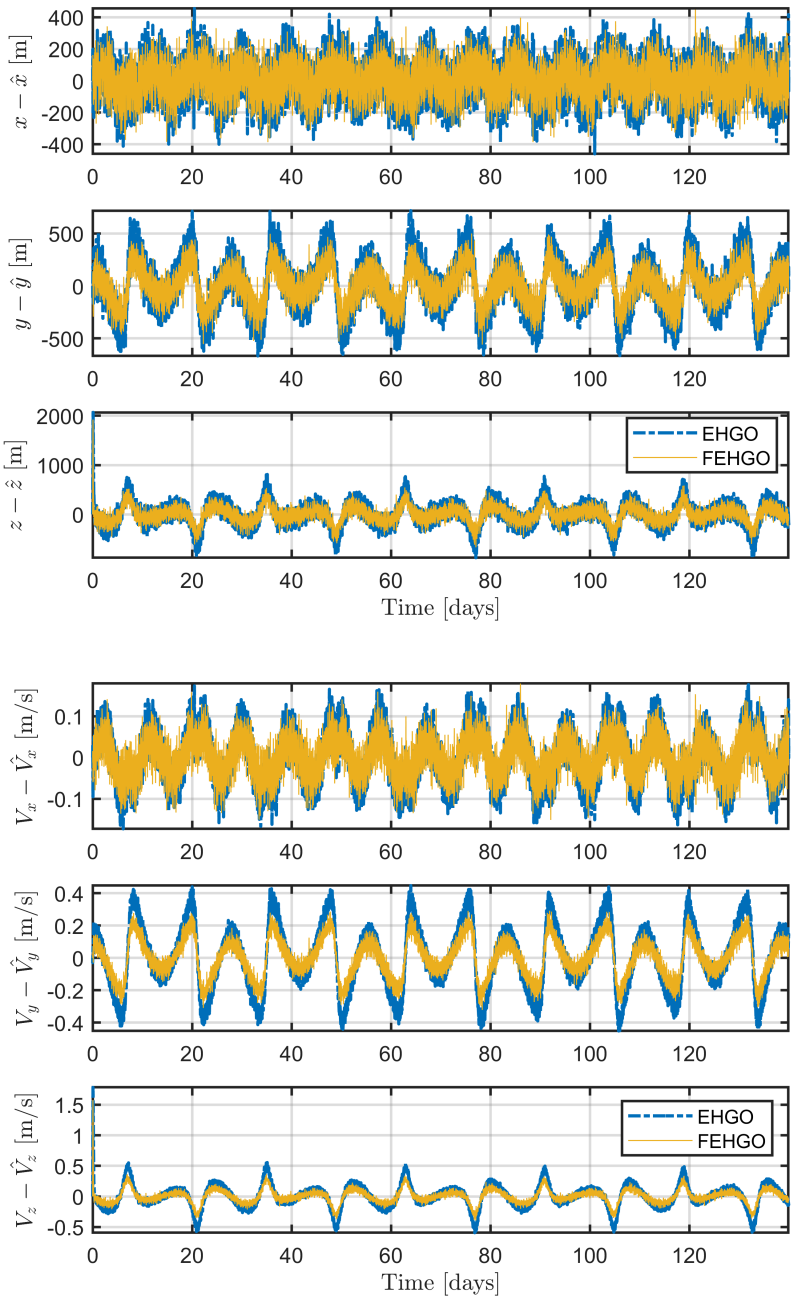

Figure 5.17 Position and velocity estimation error with different observer pole

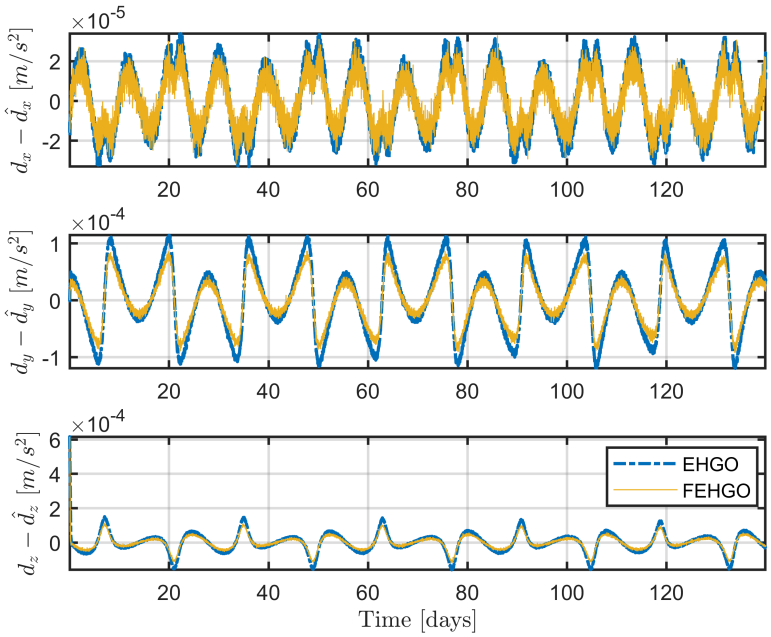

Figure 5.18 Disturbance estimation error with different observer pole

Table 5.5 Average estimation error

	EHGO			**FEHGO**		
	x	**y**	**z**	**x**	**y**	**z**
Position $[m]$	85.567	200.047	174.215	83.692	136.812	125.702
Velocity $[m/s]$	0.052	0.166	0.142	0.037	0.098	0.085
Disturbance $[m/s^2]$	1.448×10^{-5}	4.800×10^{-5}	4.101×10^{-5}	1.069×10^{-5}	3.442×10^{-5}	2.944×10^{-5}

Table 5.6 Mean and standard deviation of tracking error

	EHGO		**FEHGO**	
	mean	**std**	**mean**	**std**
ΔR $[km]$	3.473	1.979	2.435	1.477
$\lvert V \rvert$ $[m/s]$	0.064	0.182	0.057	0.158

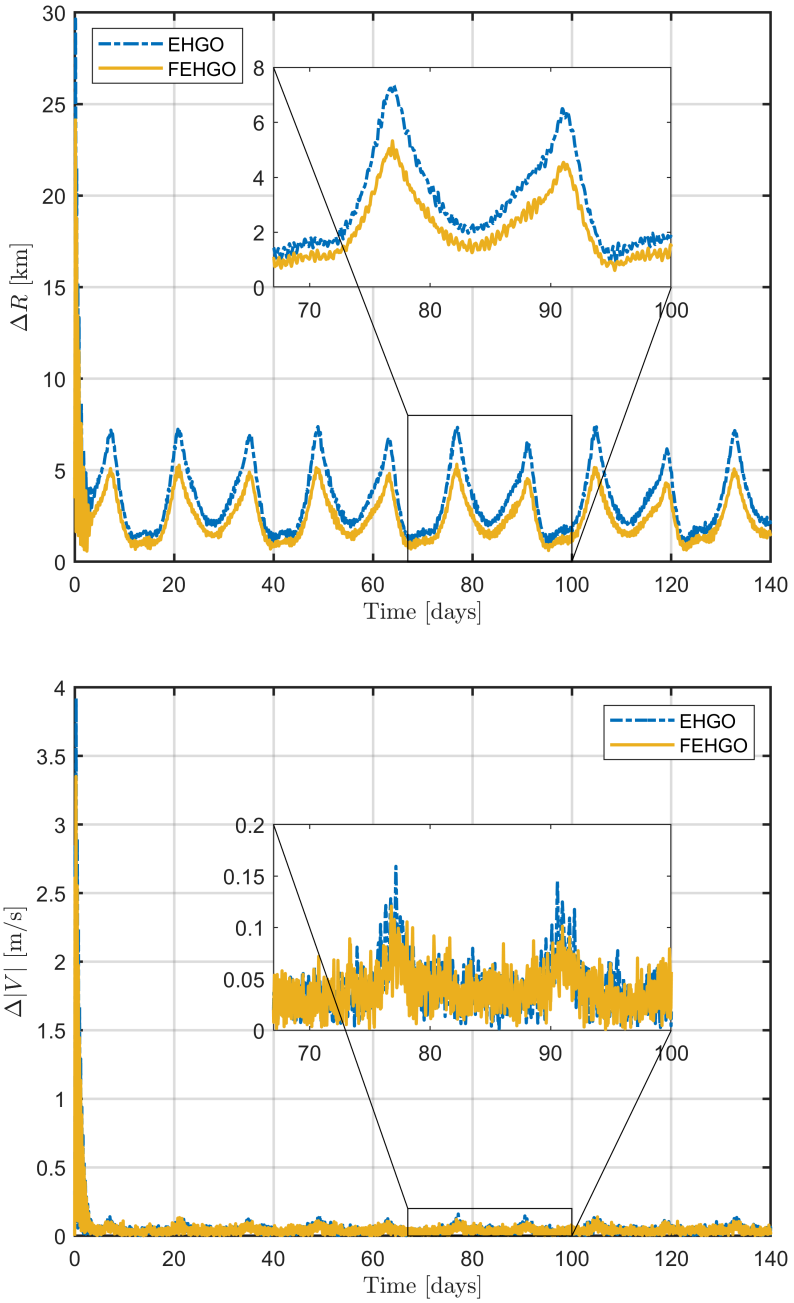

Figure 5.19 LPO position and velocity tracking error (during 10 periods)

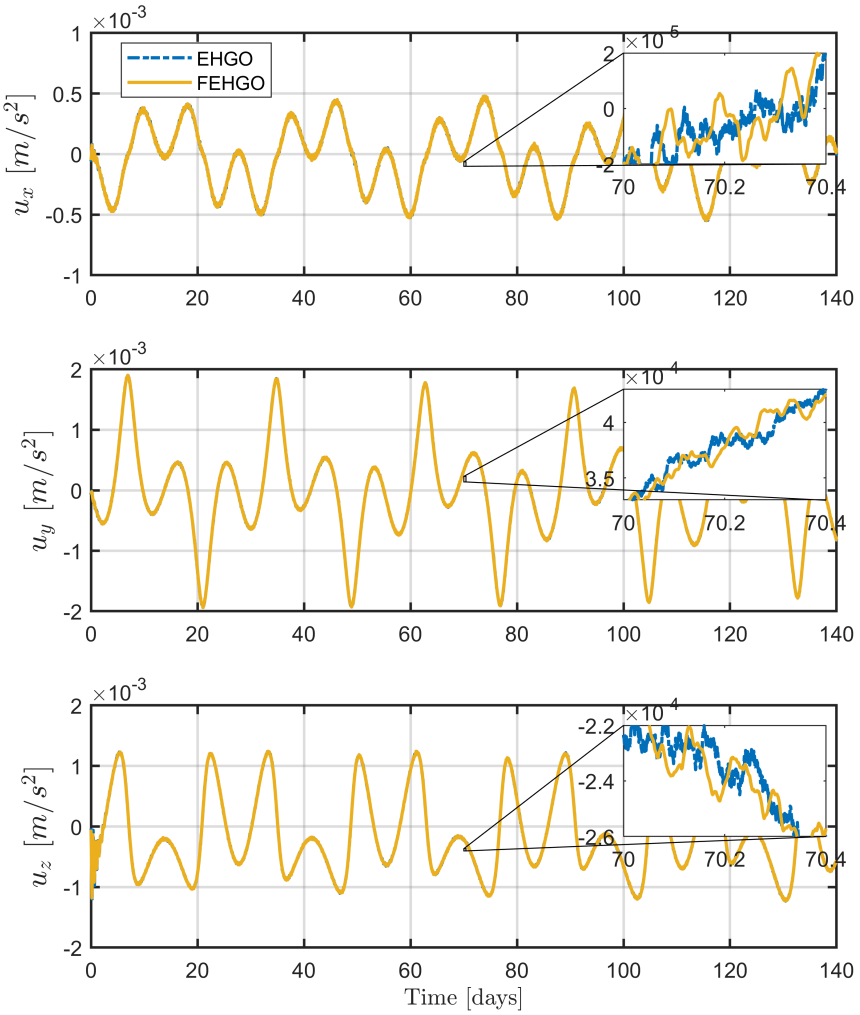

Figure 5.20 Control input history (during 10 periods)

5.3.4 Simulation 4

To reduce the orbit tracking error bound, it is important to choose the appropriate potential shaping control gain k_p and design the disturbance observer. As mentioned in Chapter 3, as a higher k_p is used, the gravitational potential around the target orbit is more deformed, and therefore the region of attraction becomes wider and more robust to the external disturbances. In this study, the terminology "region of attraction" can be used when an energy dissipation control is applied. The term "attraction" is not relevant if energy dissipation control is not applied. Figure 5.21 shows the LPO tracking error bound for the various potential shaping control gains. The mean and standard deviation of tracking error are summarized in Table 5.7. As the potential shaping control gain increases, the position tracking error bound tends to decrease. On the contrary, in the case of velocity tracking, the tracking performance becomes worse due to the noise amplification effect. This result shows that tracking performance could be degraded if the control gain is high, especially the noise level in the estimated state is not sufficiently small. In this regard, it can be stated that the FEHGO enables more effective orbit tracking than the EHGO.

In this study, the same potential shaping gains k_p are used for each direction to facilitate the control design. However, it is also possible to tune different potential shaping gains for each direction. In other words, different potential shaping gains can be assigned for each direction in the form of $\texttt{diag}(k_{p_x}, k_{p_y}, k_{p_z})$ in Eq. (3.27b), not $k_p\mathbf{I}_3$. Depending on the intensity of the disturbance, the potential shaping gain in each direction can be flexibly determined, and as a result, the tracking error bound can be adjusted. This way of the gain tuning is also applicable for energy dissipation control gain $\texttt{diag}(k_{d_x}, k_{d_y}, k_{d_z})$, which affects the

convergence speed of the transient response. Especially, if $k_{d_x} = k_{d_y} = k_{d_z} = 0$ in Eq. (4.21), spacecraft performs bounded motion with respect to the reference orbit by the results of the potential shaping control, i.e., Hamiltonian structure-preserving control. Strictly speaking, the overall closed-loop system is no longer a Hamiltonian system if the control input is designed using the estimated states. Still, if fairly accurate estimated states are used, motion of the Hamiltonian structure-preserving control can be expected, i.e., bounded motion. Figures 5.22 to 5.24 show the results during 3-period of reference orbit when there is no navigation error and no energy dissipation control is applied. First, Figs. 5.22 to 5.23 show the relative trajectory and distance of the spacecraft moving along the reference orbit, which demonstrates that the spacecraft does not converge to the reference orbit unless energy dissipation control is activated. In addition, since the disturbance rejection is well performed, it can be observed that the motion is maintained as if disturbance does not exist. In this case, however, the Lyapunov stability of spacecraft with respect to the reference orbit is not guaranteed. Instead, it can be assured the orbital stability using Floquet theory. Figure 5.24 shows the eigenvalues of the monodromy matrix obtained by numerical integration. Because the eigenvalues are located on the unit circle, the orbital stability is guaranteed.

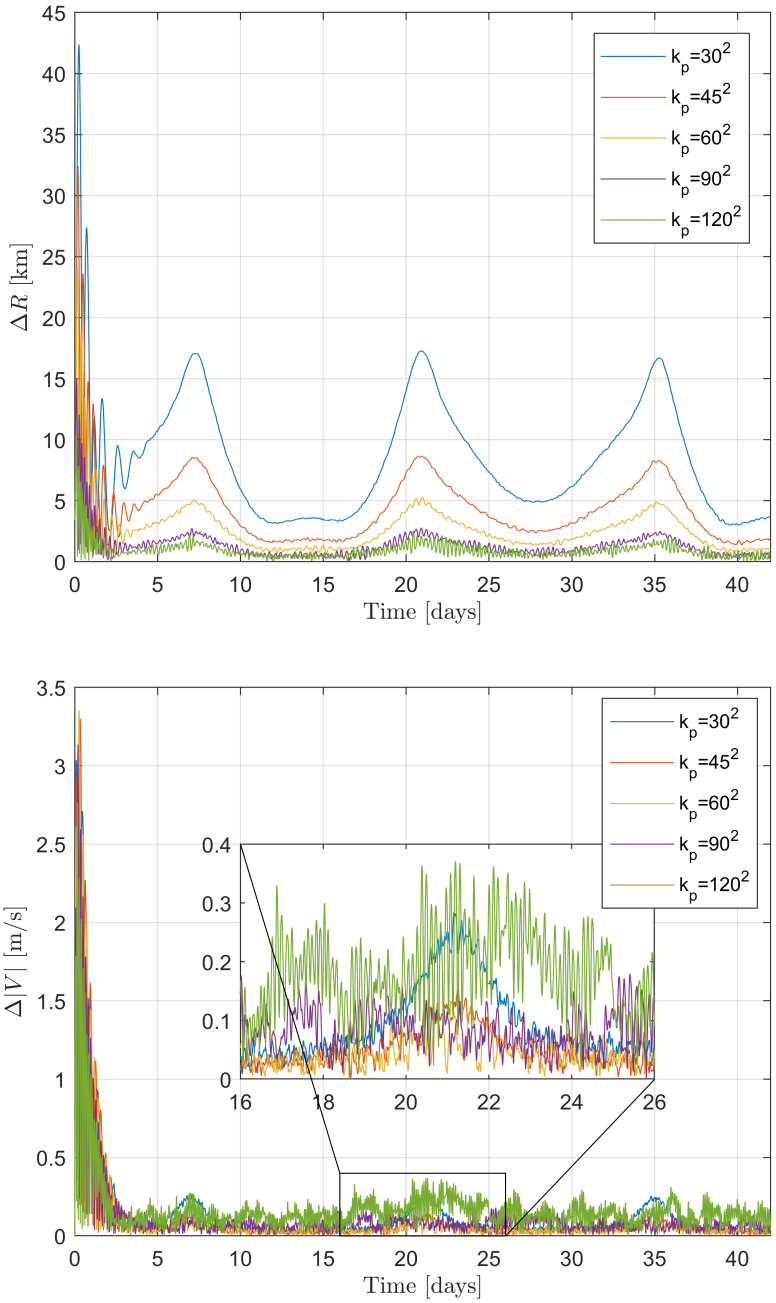

Figure 5.21 LPO position and velocity tracking error depending on potential shaping control change

Table 5.7 Mean and standard deviation of tracking error depending on potential shaping control gain

		k_p				
		30^2	45^2	60^2	90^2	120^2
ΔR $[km]$	**mean**	8.502	4.438	2.642	1.344	0.938
	std	5.026	3.014	2.020	1.140	0.730
$\|V\|$ $[m/s]$	**mean**	0.129	0.100	0.093	0.116	0.172
	std	0.281	0.298	0.283	0.241	0.195

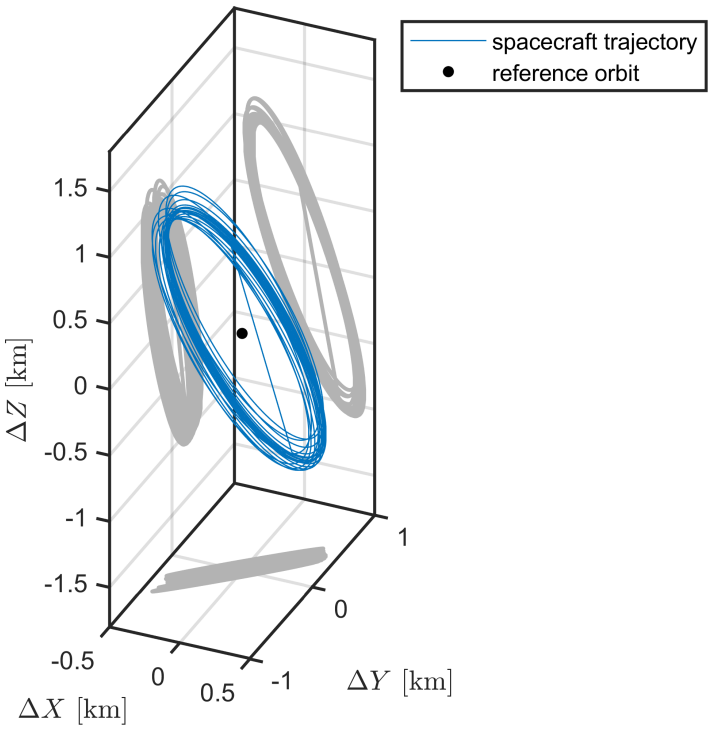

Figure 5.22 Relative trajectory of spacecraft with respect to the reference LPO without navigation error and energy dissipation control

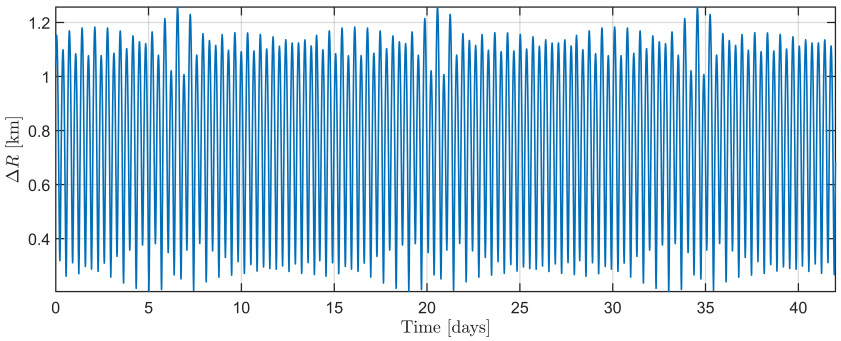

Figure 5.23 Distance of spacecraft with respect to the reference LPO without navigation error and energy dissipation control

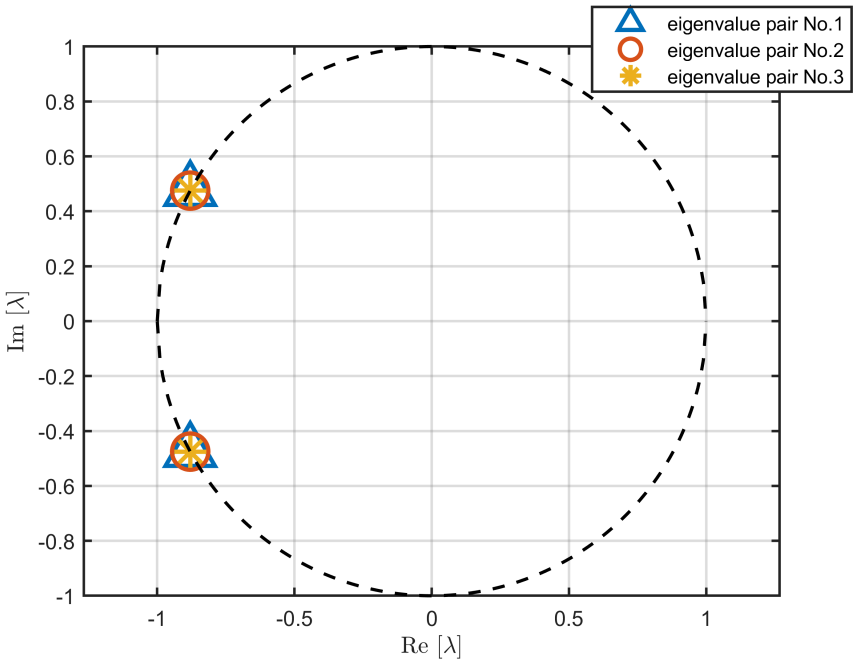

Figure 5.24 Monodromy matrix eigenvalues of controlled orbit

5.3.5 Simulation 5

In this simulation scenario, for comparison with the widely known control method, such as feedback linearization, the controller proposed by Marchand and Howell is designed [43]. Controller is designed so that the spacecraft performs relative motion with the radius and rotation rate designated by the designer. In this simulation, the radius, $\mathbf{e}_r^o$, and the rotation rate, $\mathbf{e}_\theta^o$, are designated as $50m$ and 40, respectively. The nominal radial error dynamics are designed to follow the critically damped response with natural frequency ω_n that meets some prescribed mission requirement.

$$\ddot{\mathbf{e}}_r = \ddot{\mathbf{e}}_r^o - 2\omega_n\big(\dot{\mathbf{e}}_r - \dot{\mathbf{e}}_r^o\big) - \omega_n^2\big(\mathbf{e}_r - \mathbf{e}_r^o\big)$$

And, the error dynamics for the rotation rate are specified a decaying exponential.

$$\ddot{\mathbf{e}}_\theta = \ddot{\mathbf{e}}_\theta^o - k\omega_n\big(\dot{\mathbf{e}}_\theta - \dot{\mathbf{e}}_\theta^o\big)$$

where k is an arbitrary scale factor. A more detailed description of the controller can be found in [43]. Note that, like Hamiltonian structure-preserving control, the plane of the resultant motion of the deputy spacecraft is completely determined by the initial state of the vehicle controller is activated as the Hamiltonian structure-preserving controller. Without the model uncertainty, implementation of the control law is shown in Figs. 5.25 $\sim$ 5.26. Compared to the **Simulation 1**, the results of Hamiltonian structure-preserving control and the controller proposed by Marchand and Howell are comparable. Although cancelling the nonlinear terms may generally lead to prohibitive control inputs, the application of the feedback linearization technique seems acceptable in the vicinity of the LPO region. However, when the feedback linearization is applied

under model uncertainty, namely, under the ER3BP model, all the states of the system diverged. This is a weakness of the feedback linearization technique compared to the result of **Simulation 2** and Fig. 5.27, where the Hamiltonian structure-preserving controller maintained the bounded motion of spacecraft to some extent in the same uncertain environment. In other words, it can be stated that Hamiltonian structure-preserving control is inherently robust against parameter and model uncertainties.

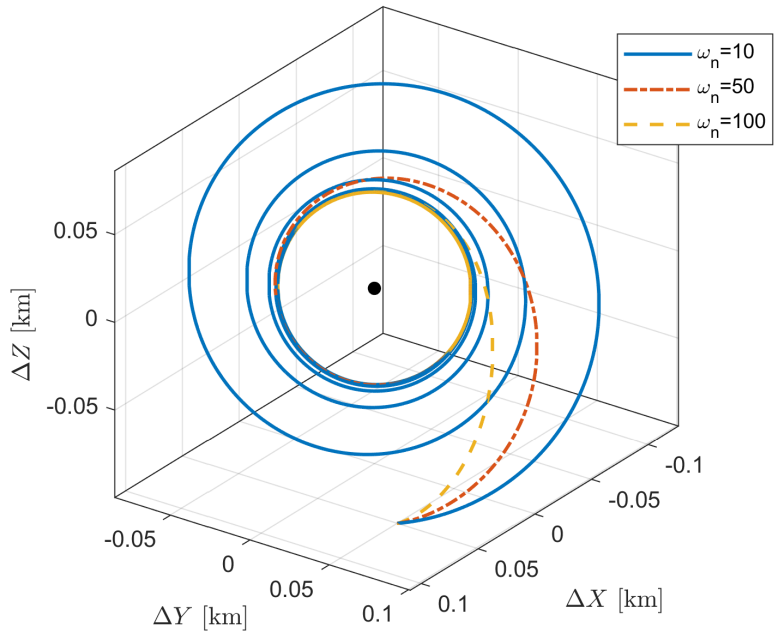

Figure 5.25 Relative trajectory of spacecraft with respect to the reference LPO

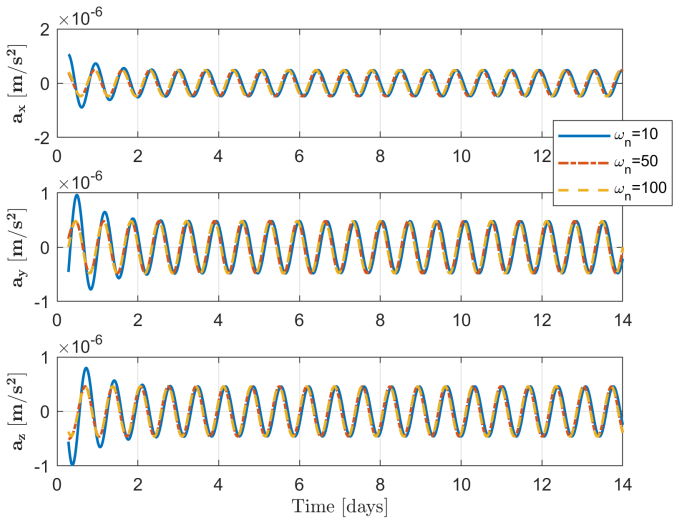

Figure 5.26 Control input

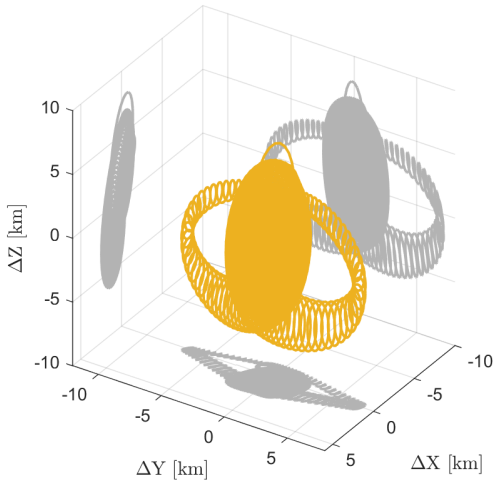

Figure 5.27 Relative trajectory of spacecraft with respect to the reference LPO under potential shaping gain $k_p = 200^2$

Chapter 6

Conclusion

6.1 Concluding Remarks

In this study, feedback control strategies were presented for spacecraft station-keeping and formation flight in the vicinity of unstable libration point orbit by leveraging the mathematical structure of the Hamiltonian system. The original concept of the Hamiltonian structure-preserving control was extended to design the desired elliptic/circular orbit pattern by means of switching control strategy. To achieve the desired relative distances, relative orbital motion was analyzed and then a strategy similar to classical Hohmann transfer was applied. By applying the developed switching Hamiltonian structure-preserving control, it is possible to adjust the radius of the relative motion systematically that could not be achieved using the existing Hamiltonian structure-preserving controller.

For the system stability analysis and the development of a controller, canonical coordinates were adopted. Through the canonical coordinate transformations, the equations of motion of spacecraft were represented in the form of Hamilton's equation with generalized coordinates and momenta, and then Hamiltonian structure-based controller was designed. The Hamiltonian structure-

based controller was divided into two parts: i) a potential shaping control, and ii) energy dissipation control. The potential shaping control makes the equilibrium point as an isolated minimum of the tracking error Hamiltonian function without destroying the Hamiltonian structure of the system. It was shown that the potential shaping control was same as the Hamiltonian structure-preserving control. Energy dissipation control makes the motion of spacecraft converge to the equilibrium point, that is, the isolated minimum of the reshaped tracking error Hamiltonian.

A filtered extended high-gain observer was designed to recover the station-keeping and formation flight performance even under highly uncertain deep-space environment. Using only the location information of spacecraft, the filtered extended high-gain observer can estimate the velocity state of spacecraft and disturbance/uncertainty acting on the spacecraft. In addition, the degradation of estimation performance is mitigated by using integral state feedback even under the strong measurement noise. The global convergence of the filtered extended high-gain observer was proved, and the tracking error was bounded to the unstable libration point orbit by applying the Hamiltonian structure-based controller.

6.2 Further Work

As more ambitious interplanetary missions appear on the roadmap for advancing the human presence in space, the understanding of spaceflight mechanics and advanced GN&C techniques are also required to progress. Within the context of orbit maintenance strategy, potential areas for future research developments are as follows,

Impulsive Station-Keeping Strategy

According to NASA's ongoing Lunar Gateway mission, the impulsive control strategy is being considered for orbit maintenance. Nominal trajectory of the Lunar Gateway mission is a Near Rectilinear Halo Orbit (NRHO), a subclass of halo orbit family, and the NRHO has a perilune and apolune. In this mission, orbital maneuver is going to be placed at or near apolune to minimize risk due to maneuver. In this regard, it would be interesting to analyze and design a new impulsive station-keeping strategy considering a various constraints.

Hamiltonian Structure-Preserving Control Under Measurement Noise

In this study, navigation error was not considered in designing the Hamiltonian structure-preserving controller. Unfortunately, navigation error always exists in real world mission, and therefore applying the Hamiltonian structure-preserving control, including navigation error, will not be able to maintain long-term bounded behavior due to navigation error effect. Because this is a very fundamental problem, it may be difficult to solve completely. Nevertheless, it would be valuable to study a new way to attenuate the effect of the navigation error.

Bibliography

[1] Lam, T., Buffington, B. B., Campagnola, S., Scott, C., and Ozimek, M., "A Robust Mission Tour for NASA's Planned Europa Clipper Mission," *AIAA/AAS Space Flight Mechanics Meeting*, Kissimmee, FL, January 2018.
DOI:10.2514/6.2018-0202

[2] Campagnola, S., Yam, C. H., Tsuda, Y., Ogawa, N., and Kawakatsu, Y., "Mission Analysis for the Martian Moons Explorer (MMX) Mission," *Acta Astronautica*, Vol. 146, 2018, pp. 409–417.
DOI:10.1016/j.actaastro.2018.03.024

[3] Snodgrass, C., and Jones, G. H., "The European Space Agency's Comet Interceptor Lies in Wait," *Nature Communications*, Vol. 10, No. 5418, 2019, pp. 1–4.
DOI:10.1038/s41467-019-13470-1

[4] Russell, R. P., "Survey of Spacecraft Trajectory Design in Strongly Perturbed Environments," *Journal of Guidance, Control, and Dynamics*, Vol. 35, No. 3, 2012, pp. 705–720.
DOI:10.2514/1.56813

[5] Quadrelli, M. B., Wood, L. J., Riedel, J. E., McHenry, M. C., Aung, M., C. L. A., Volpe, R. A., Beauchamp, P. M., and Cutts, J. A., "Guidance, Nav-

igation, and Control Technology Assessment for Future Planetary Science Missions," *Journal of Guidance, Control, and Dynamics*, Vol. 38, No. 7, 2015, pp. 1165–1186.
DOI:10.2514/1.G000525

[6] Spilker, T. R., Adler, M., Arora, N., Beauchamp, P. M., Cutts, J. A., Munk, M. M., Powell, R. W., Braun, R. D., and Wercinski, P. F., "Qualitative Assessment of Aerocapture and Applications to Future Missions," *Journal of Spacecraft and Rockets*, Vol. 56, No. 2, 2019, pp. 536–545.
DOI:10.2514/1.A34056

[7] Condon, G. L., Esty, C. C., Berry, C. F., Downs, S. P., Ocampo, C., Mahajan, B., and Burke, L. M., "Mission and Trajectory Design Considerations for a Human Lunar Mission Originating from a Near Rectiliinear Halo Orbit," *AIAA/AAS Space Flight Mechanics Meeting*, Orlando, FL, January 2020.
DOI:10.2514/6.2020-1921

[8] Folta, D. C., Pavlak, T. A., Haapala, A. F., Howell, K. C., and Woodard, M. A., "Earth-Moon Libration Point Orbit Stationkeeping: Theory, Modeling, and Operations," *Acta Astronautica*, Vol. 94, 2014, pp. 421–433.
DOI:10.1016/j.actaastro.2013.01.022

[9] Chappaz, L., and Howell, K. C., "Exploration of Bounded Motion Near Binary Systems Comprised of Small Irregular Bodies," *Celestial Mechanics and Dynamical Astronomy*, Vol. 123, 2015, pp. 123–149.
DOI:10.1007/s10569-015-9632-5

[10] Farquhar, R. W., *The Control and Use of Libration-Point Satellites*, Ph.D. Dissertation, Department of Aeronautics and Astronautics, Stanford University, Stanford, CA, July 1968.

[11] Hernandez, S., Restrepo, R. L., and Anderson, R. L., "Connecting Resonant Trajectories to a Europa Capture Through Lissajous Staging Orbits," *AAS/AIAA Space Flight Mechanics Meeting*, Maui, HI, January 2019.

[12] Bosanac, N., Webster, C. M., Howell, K. C., and Folta, D. C., "Trajectory Design for the Wide Field Infrared Survey Telescope Mission," *Journal of Guidance, Control, and Dynamics*, Vol. 42, No. 9, 2019, pp. 1899–1911. DOI:10.2514/1.G004179

[13] Canalias, E., Gomez, G., Marcote, M., and Masdemont, J. J., Assessment of Mission Design Including Utilization of Libration Points and Weak Stability Boundaries, ESA Advanced Concept Team, TR 18142/04/NL/MV, Noordwijk, The Netherlands, 2004.

[14] Koon, W. S., Lo, M. W., Marsden, J. E., and Ross, S. D., *Dynamical Systems, the Three-Body Problem and Space Mission Design*, Springer, New York, NY, 2007.

[15] Xu, M., Liang, Y., and Ren, K., "Survey on Advances in Orbital Dynamics and Control for Libration Point Orbits," *Progress in Aerospace Sciences*, Vol. 82, 2016, pp. 24–35. DOI:10.1016/j.paerosci.2015.12.005

[16] Chung, S.-J., Bandyopadhyay, S., Foust, R., Subramanian, G. P., and Hadaegh, F. Y., "Review of Formation Flying and Constellation Missions Using Nanosatellites," *Journal of Spacecraft and Rockets*, Vol. 53, No. 3, 2016, pp. 567–578.
DOI:10.2514/1.A33291

[17] Hesar, S. G., Parker, J. S., Leonard, J. M., McGranaghan, R. M., and Born, G. H., "Lunar Far Side Surface Navigation Using Linked Autonomous Interplanetary Satellite Orbit Navigation (LiAISON)," *Acta Astronautica*, Vol. 117, 2015, pp. 116–129.
DOI:10.1016/j.actaastro.2015.07.027

[18] Chen, H., Liu, J., Long, L., Xu, Z., Meng, Y., and Zhang, H., "Lunar Far Side Positioning Enabled by a CubeSat System Deployed in an Earth-Moon Halo Orbit," *Advances in Space Research*, Vol. 64, No. 1, 2019, pp. 28–41.
DOI:10.1016/j.asr.2019.03.031

[19] Peng, H., and Bai, X., "Natural Deep Space Satellite Constellation in the Earth-Moon Elliptic System," *Acta Astronautica*, Vol. 153, 2018, pp. 240–258.
DOI:10.1016/j.actaastro.2018.01.008

[20] Shirobokov, M., Trofimov, S., and Ovchinnikov, M., "Survey of Station-Keeping Techniques for Libration Point Orbits," *Journal of Guidance, Control, and Dynamics*, Vol. 40, No. 5, 2017, pp. 1085–1105.
DOI:10.2514/1.G001850

[21] Simo, C., Gomez, G., Llibre, J., Martinez, R., and Rodriguez, J., "On the Optimal Station Keeping Control of Halo Orbits," *Acta Astronautica*, Vol. 15, 1987, pp. 391–397.
DOI:10.1016/0094-5765(87)90175-5

[22] Farres, A., and Jorba, A., "A Dynamical System Approach for the Station Keeping of a Solar Sail," *Journal of the Astronautical Sciences*, Vol. 56, No. 2, 2008, pp. 199–230.
DOI:10.1007/BF03256549

[23] Farres, A., and Jorba, A., "Station Keeping of a Solar Sail Around a Halo Orbit," *Acta Astronautica*, Vol. 94, No. 1, 2014, pp. 527–539.
DOI:10.1016/j.actaastro.2012.07.002

[24] Scheeres, D. J., Hsiao, F. Y., and Vinh, N. X., "Stabilizing Motion Relative to an Unstable Orbit: Applications to Spacecraft Formation Flight," *Journal of Guidance, Control, and Dynamics*, Vol. 26, No. 1, 2003, pp. 62–73.
DOI:10.2514/2.5015

[25] Feng, J., Hou, X., and Armellin, R., "Survey on Studies About Model Uncertainties in Small Body Explorations," *Progress in Aerospace Sciences*, Vol. 110, 2019, pp. 1–12.
DOI:10.1016/j.paerosci.2019.05.009

[26] Lian, Y., Gomez, G., Masdemont, J. J., and Tang, G., "Station-Keeping of Real Earth-Moon Libration Point Orbits using Discrete-Time Sliding Mode Control," *Communications in Nonlinear Science and Numerical*

Simulation, Vol. 19, No. 10, 2014, pp. 3792–3807.
DOI:10.1016/j.cnsns.2014.03.026

[27] Kulkarni, J. E., Campbell, M. E., and Dullerud, G. E., "Stabilization of Spacecraft Flight in Halo Orbits : An H_∞ Approach," *IEEE Transactions on Control Systems Technology*, Vol. 14, No. 3, 2006, pp. 572–578.
DOI:10.1109/TCST.2006.872517

[28] Zhu, M., Karimi, H. R., Zhang, H., Gao, Q., and Wang, Y., "Active Disturbance Rejection Station-Keeping Control of Unstable Orbits Around Collinear Libration Points," *Mathematical Problems in Engineering*, Vol. 2014, 2014, pp. 1–14.
DOI:10.1155/2014/410989

[29] Lou, Z., Zhang, K., and Wang, Y., "Active Disturbance Rejection Station-Keeping Control for Solar-Sail Libration-Point Orbits," *Journal of Guidance, Control, and Dynamics*, Vol. 39, No. 8, 2016, pp. 1917–1921.
DOI:10.2514/1.G001722

[30] Narula, A., and Biggs, J. D., "Fault-Tolerant Station-Keeping on Libration Point Orbits," *Journal of Guidance, Control, and Dynamics*, Vol. 41, No. 4, 2018, pp. 879–887.
DOI:10.2514/1.G003115

[31] Akiyama, Y., Bando, M., and Hokamoto, S., "Explicit Form of Station-Keeping and Formation Flying Controller for Libration Point Orbits," *Journal of Guidance, Control, and Dynamics*, Vol. 41, No. 6, 2018,

pp. 1405–1413.
DOI:10.2514/1.G002845

[32] Akiyama, Y., Bando, M., and Hokamoto, S., "Station-Keeping and Formation Flying Based on Nonlinear Output Regulation Theory," *Acta Astronautica*, Vol. 153, 2018, pp. 289–296.
DOI:10.1016/j.actaastro.2018.02.004

[33] Folta, D., Hartman, K., Howell, K. C., and Marchand, B., "Formation Control of the MAXIM Ł$_2$ Libration Orbit Mission," *AIAA/AAS Astrodynamics Specialist Conference*, Providence, RI, August 2004.
DOI:10.2514/6.2004-5211

[34] Beichman, C., Gomez, G., Lo, M., Masdemont, J., and Romans, L., "Searching for Life with the Terrestrial Planet Finder: Lagrange Point Options for a Formation Flying Interferometer," *Advances in Space Research*, Vol. 34, No. 3, 2004, pp. 637–644.
DOI:10.1016/j.asr.2003.05.032

[35] Fridlund, C. V. M., "The Darwin Mission," *Advances in Space Research*, Vol. 34, No. 3, 2004, pp. 613–617.
DOI:10.1016/j.asr.2003.05.031

[36] Farres, A., and Webster, C. M., "Wide-Field Infrared Survey Telescope and Starshade Formation Flying Dynamics at Sun-Earth Ł$_2$," *69th International Astronautical Congress*, Bremen, Germany, October 2018.

[37] Mauro, G. D., Lawn, M., and Bevilacqua, R., "Survey on Guidance Navigation and Control Requirements for Spacecraft Formation-Flying Mis-

sions," *Journal of Guidance, Control, and Dynamics*, Vol. 41, No. 3, 2018, pp. 581–602.
DOI:10.2514/1.G002868

[38] Gomez, G., Marcote, M., Masdemont, J. J., and Mondelo, J. M., "Zero Relative Radial Acceleration Cones and Controlled Motions Suitable for Formation Flying," *Journal of the Astronautical Sciences*, Vol. 53, No. 4, 2005, pp. 413–431.

[39] Heritier, A., and Howell, K. C., "Natural Regions Near the Collinear Libration Points Ideal for Space Observations with Large Formations," *Journal of the Astronautical Sciences*, Vol. 60, 2013, pp. 87–108.
DOI:10.1007/s40295-014-0027-8

[40] Heritier, A., and Howell, K. C., "Dynamical Evolution of Natural Formations in Libration Point Orbits in a Multi-Body Regime," *Acta Astronautica*, Vol. 102, 2014, pp. 332–340.
DOI:10.1016/j.actaastro.2013.10.017

[41] Ferrari, F., and Lavagna, M., "Suitable Configurations for Triangular Formation Flying About Collinear Libration Points Under the Circular and Elliptic Restricted Three-Body Problems," *Acta Astronautica*, Vol. 147, 2018, pp. 374–382.
DOI:10.1016/j.actaastro.2016.08.011

[42] Gurfil, P., and Kasdin, N. J., "Stability and Control of Spacecraft Formation Flying in Trajectories of the Restricted Three-Body Problem," *Acta*

Astronautica, Vol. 54, No. 6, 2004, pp. 433–453.
DOI:10.1016/S0094-5765(03)00170-X

[43] Marchand, B. G., and Howell, K. C., "Control Strategies for Formation Flight in the Vicinity of the Libration Points," *Journal of Guidance, Control, and Dynamics*, Vol. 28, No. 6, 2005, pp. 1210–1219.
DOI:10.2514/1.11016

[44] Gurfil, P., Idan, M., and Kasdin, N. J., "Adaptive Neural Control of Deep-Space Formation Flying," *Journal of Guidance, Control, and Dynamics*, Vol. 26, No. 3, 2003, pp. 491–501.
DOI:10.2514/2.5072

[45] Peng, H., Zhao, J., Wu, Z., and Zhong, W., "Optimal Periodic Controller for the Formation Flying on Libration Point Orbits," *Acta Astronautica*, Vol. 69, No. 7–8, 2011, pp. 537–550.
DOI:10.1016/j.actaastro.2011.04.020

[46] Xin, M., Balakrishnan, S. N., and Pernicka, H. J., "Multiple Spacecraft Formation Control with $\theta - D$ Method," *IET Control Theory & Applications*, Vol. 1, No. 2, 2007, pp. 485–493.
DOI:10.1049/iet-cta:20050410

[47] Xin, M., Balakrishnan, S. N., and Pernicka, H. J., "Position and Attitude Control of Deep-Space Spacecraft Formation Flying Via Virtual Structure and $\theta - D$ Technique," *Journal of Dynamic Systems, Measurement, and Control*, Vol. 129, No. 5, 2007, pp. 689–698.
DOI:10.1115/1.2764509

[48] Bando, M., and Ichikawa, A., "Formation Flying Along Halo Orbit of Circular-Restricted Three-Body Problem," *Journal of Guidance, Control, and Dynamics*, Vol. 38, No. 1, 2015, pp. 123–129.
DOI:10.2514/1.G000463

[49] Ardaens, J. S., and D'Amico, S., Control of Formation Flying Spacecraft at a Lagrange Point, Deutsches Zentrum fur Luft- und Raumfahrt, TN 08-01, Wessling, Germany, Apr. 2008.

[50] Howell, K. C., and Marchand, B. G., "Natural and Non-Natural Spacecraft Formations Near the L_1 and L_2 Libration Point in the Sun-Earth/Moon Ephemeris System," *Dynamical Systems: An International Journal*, Vol. 20, No. 1, 2005, pp. 149–173.
DOI:10.1080/1468936042000298224

[51] Pernicka, H. J., Carlson, B. A., and Balakrishnan, S. N., "Spacecraft Formation Flight About Libration Points Using Impulsive Maneuvering," *Journal of Guidance, Control, and Dynamics*, Vol. 29, No. 5, 2006, pp. 1122–1130.
DOI:10.2514/1.18813

[52] Qi, R., Xu, S., and Xu, M., "Impulsive Control for Formation Flight About Libration Points," *Journal of Guidance, Control, and Dynamics*, Vol. 35, No. 2, 2012, pp. 484–496.
DOI:10.2514/1.54383

[53] Wang, W., Mengali, G., Quarta, A. A., and Yuan, J., "Distributed Adaptive Synchronization for Multiple Spacecraft Formation Flying around La-

grange Point Orbits," *Aerospace Science and Technology*, Vol. 74, 2018, pp. 93–103.
DOI:10.1016/j.ast.2018.01.007

[54] Xu, M., and Xu, S., "Structure-Preserving Stabilization for Hamiltonian System and Its Applications in Solar Sail," *Journal of Guidance, Control, and Dynamics*, Vol. 32, No. 3, 2009, pp. 997–1004.
DOI:10.2514/1.34757

[55] Soldini, S., Colombo, C., and Walker, S. J. I., "Comparison of Hamiltonian Structure-preserving and Floquet Mode Station-Keeping for Libration-Point Orbits," *AIAA/AAS Astrodynamics Specialist Conference*, San Diego, CA, August 2014.
DOI:10.2514/6.2014-4118

[56] Soldini, S., Colombo, C., and Walker, S. J. I., "Solar Radiation Pressure Hamiltonian Feedback Control for Unstable Libration-Point Orbits," *Journal of Guidance, Control, and Dynamics*, Vol. 40, No. 6, 2017, pp. 1374–1389.
DOI:10.2514/1.G002090

[57] van der Schaft, A. J., "Stabilization of Hamiltonian Systems," *Nonlinear Analysis: Theory, Methods & Applications*, Vol. 10, No. 10, 1986, pp. 1021–1035.
DOI:10.1016/0362-546X(86)90086-6

[58] Freidovich, L. B., and Khalil, H. K., "Performance Recovery of Feedback-Linearization Based Designs," *IEEE Transactions on Automatic Control*,

Vol. 53, No. 10, 2008, pp. 2324–2334.
DOI:10.1109/TAC.2008.2006821

[59] Khalil, H. K., "High-Gain Observers in Feedback Control: Application to Permanent Magnet Synchronous Motors," *IEEE Control Systems*, Vol. 37, No. 3, 2017, pp. 25–41.
DOI:10.1109/MCS.2017.2674438

[60] Ahrens, J. H., and Khalil, H. K., "High-Gain Observers in the Presence of Measurement Noise: A Switched-Gain Approach," *Automatica*, Vol. 45, No. 4, 2009, pp. 936–943.
DOI:10.1016/j.automatica.2008.11.012

[61] Sanfelice, R. G., and Praly, L., "On the Performance of High-Gain Observers with Gain Adaptation Under Measurement Noise," *Automatica*, Vol. 47, No. 10, 2011, pp. 2165–2176.
DOI:10.1016/j.automatica.2011.08.002

[62] Prasov, A. A., and Khalil, H. K., "A Nonlinear High-Gain Observer for Systems with Measurement Noise in a Feedback Control Framework," *IEEE Transactions on Automatic Control*, Vol. 58, No. 3, 2013, pp. 569–580.
DOI:10.1109/TAC.2012.2218063

[63] Khalil, H. K., and Priess, S., "Analysis of the Use of Low-Pass Filters with High-Gain Observers," *Proceedings of the IFAC Symposium on Nonlinear Control Systems*, Monterey, CA, August 2016.
DOI:10.1016/j.ifacol.2016.10.212

[64] Busawon, K. K., and Kabore, P., "Disturbance Attenuation Using Proportional Integral Observers," *International Journal of Control*, Vol. 74, No. 6, 2001, pp. 618–627.
DOI:10.1080/00207170010025249

[65] Szebehely, V., *Theory of Orbits: The Restricted Problem of Three Bodies*, Academic, New York, NY, 1967.

[66] Battin, R. H., *An Introduction to the Mathematics and Methods of Astrodynamics*, AIAA Education Series, American Institute of Aeronautics and Astronautics, Reston, VA, 1999.

[67] Schaub, H., and Junkins, J. L., *Analytical Mechanics of Space Systems*, 3rd ed., AIAA Education Series, American Institute of Aeronautics and Astronautics, Reston, VA, 2014.

[68] Gomez, G., and Mondelo, J. M., "The Dynamics Around the Collinear Equilibrium Points of the RTBP," *Physica D: Nonlinear Phenomena*, Vol. 157, No. 4, 2001, pp. 283–321.
DOI:10.1016/S0167-2789(01)00312-8

[69] Jorba, A., and Masdemont, J., "Dynamics in the Center Manifold of the Collinear Points of the Restricted Three Body Problem," *Physica D: Nonlinear Phenomena*, Vol. 132, No. 1-2, 1999, pp. 189–213.
DOI:10.1016/S0167-2789(99)00042-1

[70] Doedel, E. J., Paffenroth, R. C., Keller, H. B., Dichmann, D. J., Galan-Vioque, J., and Vanderbauwhede, A., "Computation of Periodic Solutions of Conservative Systems with Application to the 3-Body Problem,"

International Journal of Bifurcation and Chaos, Vol. 13, No. 6, 2003, pp. 1353–1381.
DOI:10.1142/S0218127403007291

[71] Farquhar, R. W., Muhonen, D. P., Newman, C. R., and Heuberger, H. S., "Trajectories and Orbital Maneuvers for the First Libration-Point Satellite," *Journal of Guidance, Control, and Dynamics*, Vol. 3, No. 6, 1980, pp. 549–554.
DOI:10.2514/3.56034

[72] McKay, R. J., Macdonald, M., Biggs, J., and McInnes, C., "Survey of Highly-Non-Keplerian Orbits with Low-Thrust Propulsion," *Journal of Guidance, Control, and Dynamics*, Vol. 34, No. 3, 2011, pp. 645–666.
DOI:10.2514/1.52133

[73] Howell, K. C., "Three-Dimensional, Periodic, 'Halo' Orbits," *Celestial Mechanics*, Vol. 32, No. 1, 1984, pp. 53–71.
DOI:10.1007/BF01358403

[74] Marchand, B. G., Howell, K. C., and Wilson, R. S., "Improved Corrections Process for Constrained Trajectory Design in the n-Body Problem," *Journal of Spacecraft and Rockets*, Vol. 44, No. 4, 2007, pp. 884–897.
DOI:10.2514/1.27205

[75] Strogatz, S. H., *Nonlinear Dynamics and Chaos: With Applications to Physics, Biology, Chemistry, and Engineering*, 2nd ed., Chap. 8, Westview Press, Boulder, CO, 2015.

[76] Haapala, A. F., Howell, K. C., and Folta, D. C., "Incorporating the Evolution of Multi-body Orbits into the Trajectory Trade Space and Design Process," *Acta Astronautica*, Vol. 112, 2015, pp. 1–18.
DOI:10.1016/j.actaastro.2015.02.024

[77] Meyer, K., Hall, G., and Offin, D. C., *Introduction to Hamiltonian Dynamical Systems and N-Body Problem*, 2nd ed., Springer, New York, NY, 2009.

[78] Scheeres, D. J., Hsiao, F. Y., Park, R. S., Villac, B. F., and Maruskin, J. M., "Fundamental Limits on Spacecraft Orbit Uncertainty and Distribution Propagation," *Journal of the Astronautical Sciences*, Vol. 54, No. 3–4, 2006, pp. 505–523.
DOI:10.1007/BF03256503

[79] Barden, B. T., and Howell, K. C., "Fundamental Motions Near Collinear Libration Points and Their Transitions," *Journal of the Astronautical Sciences*, Vol. 46, No. 4, 1998, pp. 361–378.

[80] Henry, D. B., and Scheeres, D. J., "Generalized Spacecraft Formation Design through Exploitation of Quasi-Periodic Tori Families," *AIAA/AAS Space Flight Mechanics Meeting*, Orlando, FL, January 2020.
DOI:10.2514/6.2020-0950

[81] Xu, M., Zhu, J., Tan, T., and Xu, S., "Application of Hamiltonian Structure-Preserving Control to Formation Flying on a J_2-Perturbed Mean Circular Orbit," *Celestial Mechanics and Dynamical Astronomy*,

Vol. 113, No. 4, 2012, pp. 403–433.
DOI:10.1007/s10569-012-9430-2

[82] Xu, M., Liang, Y., Tan, T., and Wei, L., "Cluster Flight Control for Fractionated Spacecraft on an Elliptic Orbit," *Celestial Mechanics and Dynamical Astronomy*, Vol. 125, No. 4, 2016, pp. 383–412.
DOI:10.1007/s10569-016-9685-0

[83] Liang, Y., Xu, M., and Xu, S., "Bounded Motions near Contact Binary Asteroids by Hamiltonian Structure-Preserving Control," *Journal of Guidance, Control, and Dynamics*, Vol. 41, No. 2, 2018, pp. 401–416.
DOI:10.2514/1.G002528

[84] Pan, X., Xu, M., and Dong, Y., "Low-Thrust Displaced Orbits by Weak Hamiltonian-Structure-Preserving Control," *Communications in Nonlinear Science and Numerical Simulation*, Vol. 62, 2018, pp. 282–306.
DOI:10.1016/j.cnsns.2018.02.036

[85] Jung, S., and Kim, Y., "Formation Flying along Unstable Libration Point Orbits Using Switching Hamiltonian Structure-preserving Control," *Acta Astronautica*, Vol. 158, 2019, pp. 1–11.
DOI:10.1016/j.actaastro.2018.07.020

[86] Jung, S., and Kim, Y., "Hamiltonian Structure-Based Robust Station-Keeping for Unstable Libration Point Orbits," *Journal of Guidance, Control, and Dynamics*, Vol. 42, No. 9, 2019, pp. 1912–1929.
DOI:10.2514/1.G003990

[87] Kirillov, O. N., "Destabilization Paradox Due to Breaking the Hamiltonian and Reversible Symmetry," *International Journal of Non-Linear Mechanics*, Vol. 42, No. 1, 2007, pp. 71–87.
DOI:10.1016/j.ijnonlinmec.2006.09.003

[88] Hsiao, F. Y., *Stabilizing and Specifying Motion Relative to Unstable Trajectories: Applications to Spacecraft Formation Flight*, Ph.D. Dissertation, Department of Aerospace Engineering, University of Michigan, Ann Arbor, MI, April 2004.

[89] Hsiao, F. Y., and Scheeres, D. J., "The Dynamics of Formation Flight About a Stable Trajectory," *Journal of the Astronautical Sciences*, Vol. 50, No. 3, 2002, pp. 269–287.

[90] Liberzon, D., and Morse, A. S., "Basic Problems in Stability and Design of Switched Systems," *IEEE Control Systems Magazine*, Vol. 19, No. 5, 1999, pp. 59–70.
DOI:10.1109/37.793443

[91] Liberzon, D., *Switching in Systems and Control*, Birkhauser, Boston, MA, USA, 2003.

[92] Ortega, R., van der Schaft, A., Mareels, I., and Maschke, B., "Putting Energy Back in Control," *IEEE Control Systems Magazine*, Vol. 21, No. 1, 2001, pp. 18–33.
DOI:10.1109/37.915398

[93] Sastry, S., *Nonlinear Systems: Analysis, Stability, and Control*, Chap. 2, Springer, New York, NY, 1999.

[94] Marsden, J. E., and Ratiu, T. S., *Introduction to Mechanics and Symmetry: A Basic Exposition of Classical Mechanical Systems*, 2nd ed., Springer, New York, NY, 2002.

[95] Krechetnikov, R., and Marsden, J. E., "Dissipation-Induced Instabilities in Finite Dimensions," *Reviews of Modern Physics*, Vol. 79, No. 2, 2007, pp. 519–553.
DOI:10.1103/RevModPhys.79.519

[96] Holm, D. D., Marsden, J. E., Ratiu, T., and Weinstein, A., "Nonlinear Stability of Fluid and Plasma Equilibria," *Physics Reports*, Vol. 123, No. 1-2, 1985, pp. 1–116.
DOI:10.1016/0370-1573(85)90028-6

[97] Takegaki, M., and Arimoto, S., "A New Feedback Method for Dynamic Control of Manipulators," *Journal of Dynamic Systems, Measurement, and Control*, Vol. 103, No. 2, 1981, pp. 119–125.
DOI:10.1115/1.3139651

[98] Jalnapurkar, S. M., and Marsden, J. E., "Stabilization of Relative Equilibria," *IEEE Transactions on Automatic Control*, Vol. 45, No. 8, 2000, pp. 1483–1491.
DOI:10.1109/9.871756

[99] Hsiao, F. Y., and Scheeres, D. J., "Design of Spacecraft Formation Orbits Relative to a Stabilized Trajectory," *Journal of Guidance, Control, and Dynamics*, Vol. 28, No. 4, 2005, pp. 782–794.
DOI:10.2514/1.8433

[100] Arnot, C. S., McInnes, C. R., McKay, R. J., Macdonald, M., and Biggs, J., "Orbit Period Modulation for Relative Motion using Continuous Low Thrust in the Two-Body and Restricted Three-Body Problems," *Celestial Mechanics and Dynamical Astronomy*, Vol. 130, No. 12, 2018.
DOI:10.1007/s10569-017-9807-3

[101] Wiggins, S., *Introduction to Applied Nonlinear Dynamical Systems and Chaos*, Chap. 1, 2nd ed., Chap. 1, Springer, New York, NY, 2003.

[102] Ortega, R., van der Schaft, A. J., Maschke, B., and Escobar, G., "Interconnection and Damping Assignment Passivity-Based Control of Port-Controlled Hamiltonian Systems," *Automatica*, Vol. 38, No. 4, 2002, pp. 585–596.
DOI:10.1016/S0005-1098(01)00278-3

[103] Astolfi, A., Isidori, A., and Marconi, L., "A Note on Disturbance Suppression for Hamiltonian Systems by State Feedback," *Proceedings of the IFAC Workshop on Lagrangian and Hamiltonian Methods in Nonlinear Systems*, Seville, Spain, April 2003.
DOI:10.1016/S1474-6670(17)38893-6

[104] Wang, Y., and Ge, S. S., "Augmented Hamiltonian Formulation and Energy-Based Control Design of Uncertain Mechanical Systems," *IEEE Transactions on Control Systems Technology*, Vol. 16, No. 2, 2008, pp. 202–213.
DOI:10.1109/TCST.2007.903367

[105] Romero, J. G., Donaire, A., and Ortega, R., "Robust Energy Shaping Control of Mechanical Systems," *Systems & Control Letters*, Vol. 62, No. 9, 2013, pp. 770–780.
DOI:10.1016/j.sysconle.2013.05.011

[106] Khalil, H. K., *Nonlinear Systems*, 3rd ed., Prentice-Hall, Upper Saddle River, NJ, 2002.

[107] Gui, H., and de Ruiter, A. H. J., "Control of Asteroid-Hovering Spacecraft with Disturbance Rejection Using Position-Only Measurements," *Journal of Guidance, Control, and Dynamics*, Vol. 40, No. 10, 2017, pp. 2401–2416.
DOI:10.2514/1.G002617

[108] Peng, H., Bai, X., Masdemont, J. J., Gomez, G., and Xu, S., "Libration Transfer Design Using Patched Elliptic Three-Body Models and Graphics Processing Units," *Journal of Guidance, Control, and Dynamics*, Vol. 40, No. 12, 2017, pp. 3155–3166.
DOI:10.2514/1.G002692

[109] Sweetser, T. H., Broschart, S. B., Angelopoulos, V., Whiffen, G. J., Folta, D. C., Chung, M., Hatch, S. J., and Woodard, M. A., "ARTEMIS Mission Design," *Space Science Reviews*, Vol. 165, No. 1–4, 2011, pp. 27–57.
DOI:10.1007/s11214-012-9869-1

[110] Shirobokov, M., Trofimov, S., and Ovchinnikov, M., "Recovery of Halo Orbit Missions in Case of Contingent Station-keeping Maneuver Delay,"

Advances in Space Research, Vol. 58, No. 9, 2016, pp. 1807–1818.
DOI:10.1016/j.asr.2016.07.003

[111] Grebow, D. J., Ozimek, M. T., Howell, K. C., and Folta, D. C., "Multibody Orbit Architectures for Lunar South Pole Coverage," *Journal of Spacecraft and Rockets*, Vol. 45, No. 2, 2008, pp. 344–358.
DOI:10.2514/1.28738

국문초록

본 논문에서는 불안정한 동적특성을 갖는 라그랑주 점 궤도 주변에서 위성의 궤도유지 및 편대비행을 위한 제어기와 관측기를 설계하였으며, 설계된 제어기와 관측기의 안정성 그리고 전체 시스템의 안정성을 분석하였다. 설계한 기준 제어 전략은 신호처리 관점의 제어이론을 기반으로 하지 않고, 라그랑주 점 궤도의 자연적인 수학적 구조를 활용하였다. 모델 불확실성과 외부 외란으로 인한 기준 제어 전략의 성능저하를 완화하기 위해 외란관측기의 일종인 확장 고이득 관측기를 설계하였다.

본 논문에서는 궤도역학에 내재되어 있는 해밀턴 시스템의 구조를 활용하는 제어기를 설계하기 위해 정준좌표를 도입하였으며, 좌표변환을 통해 위성의 운동방정식을 해밀턴 시스템의 정준형식으로 나타내었다. 해밀턴 시스템의 정준형식으로 표현된 운동방정식을 이용해 설계한 기준 제어기는 해밀턴-구조 보존제어와 에너지 소산제어로 분리 설계된다. Lagrange-Dirichlet 기준은 정준형식으로 나타낸 해밀턴 시스템의 비선형 안정성을 판별하는 충분조건으로, 해밀턴-구조 보존제어 설계의 기준이 된다. 기준 라그랑주 점 궤도 주위에서 해밀턴-구조 보존 제어를 적용한 결과, 위성은 기준궤도로 수렴하지 않고 기준궤도와 유한한 거리를 유지하는 경계운동을 하였다. 경계운동의 주파수 분석을 통하여 특정한 초기조건 하에서는 원형 경계운동이 가능하였으며, 더 나아가 해밀턴-구조 보존제어의 제어이득 값을 적절히 설정함으로 원형 경계운동의 크기를 체계적으로 조절할 수 있고 이를 위성 편대비행에 응용할 수 있음을 보였다. 추가적으로 에너지 소산제어 입력을 설계하여 위성이 기준 라그랑주 점 궤도로 점근 수렴하는 운동도 가능함을 수학적으로 증명하였다.

한편, 심우주상의 예측하기 어려운 섭동력 및 불확실성 하에서도 강건한 궤도 유지와 편대비행을 수행하기 위해 확장 고이득 관측기를 설계하였다. 확장 고이득 관측기는 위성의 위치 정보만을 이용하여 위성의 속도와 위성에 작용하는 외란을 동시에 추정하며, 추정된 상태변수를 이용하여 기준이 되는 피드백 제어입력을 생성한다. 추정된 외란은 피드포워드 형태의 제어입력으로 구성되어 제어기의 성능을 강건하게 만든다. 심우주 공간상의 위성의 궤도결정 결과로 얻어지는 위치정보는 상대적으로 큰 오차를 갖는데, 확장 고이득 관측기는 위치 오차를 증폭시킨다는 단점이 있다. 본 연구에서는 이러한 단점을 완화하고자 적분 관측기 형태로 개선된 필터링된 확장 고이득 관측기를 설계하고 수렴성을 분석하였다. 그리고 필터링된 확장 고이득 관측기와 시스템의 해밀턴 구조를 활용하는 제어기를 적용한 전체 시스템의 안정성을 분석하였다.

불안정한 라그랑주 점 궤도 주변에서 위성의 궤도유지와 편대비행을 위해 설계된 제어기법의 성능을 확인하고자 수치 시뮬레이션을 수행하였다. 수치 시뮬레이션을 위해 지구-달 시스템의 L_2 주변 헤일로 궤도를 기준궤도로 설정하였으며, 심우주 공간에서의 다양한 섭동력 및 모델 불확실성을 고려하였다. 궤도결정 오차로 인한 위성의 위치 및 속도 불확실성이 존재 하더라도 제안한 제어기법을 통해 위성이 궤도유지와 편대비행을 만족스럽게 수행함을 보였다.

주요어: 라그랑주 점 궤도, 불안정 궤도, 비케플러 궤도, 위성 궤도유지, 위성 편대비행, 해밀턴 시스템, 확장 고이득 관측기

학번: 2015-20790